A damage plastic approach for modelling strain hardening cementitious composites

by

Chao Zhou

James Watt School of Engineering

University of Glasgow

Submitted in fulfilment of requirements for the degree of

Doctor of Philosophy

September 2024

Declaration

I declare that this thesis is a record of the original work carried out by me under the supervision of Dr. Peter Grassl in the Infrastructure & Environment Division of the School of Engineering at the University of Glasgow, United Kingdom. This research was undertaken during the period of October 2020 to October 2024. I further declare that this thesis has not previously formed the basis for the award of any degree, diploma or other similar title of recognition.

Publications based on this thesis:

Paper 1: Zhou, C.; Marlot, A., and Grassl, P. Cdpm2f: A damage-plasticity approach for modelling the failure of strain hardening cementitious composites. Engineering Fracture Mechanics, 2024.

Paper 2: Zhou, C. and Grassl, P. On the failure process of steel reinforced strain hardening cementitious composites. In preparation

In Paper 1, I wrote the original draft, prepared the figures, developed the software and performed the FE-analyses.

In Paper 2, I wrote the original draft, prepared the figures and carried out the finite element analyses.

Chao Zhou

Abstract

Strain hardening cementitious composites or engineered cementitious composites exhibit significantly larger strains at maximum tensile stress than ordinary fibre reinforced concrete. The performance of strain hardening cementitious composites relies on the fibre/matrix properties at the micro-scale. A micro-mechanics based constitutive model for fibre reinforced strain hardening cementitious composites for finite element simulations of structural components is required.

Steel reinforced strain hardening cementitious composites potentially could be used as a composite material of structural component to improve ductility and load capacity. However, the failure process of steel reinforced strain hardening cementitious composite is not well understood because of the complex interaction of two scales of reinforcement involving crack patterns with spacings at multiple scales.

In this research, it is aimed to establish the link of micro-mechanics to structural component by incorporating a micro-mechanics based fibre bridging stress crack opening law into a macroscopic damage-plasticity approach, which is called CDPM2F. The model is implemented in the open-source finite element program OOFEM. The model produces mesh-insensitive results and its response agrees well with experimental results for failure in tension, shear and compression reported in the literature.

The response of specimens made of cementitious composites with a single reinforcement bar embedded in its centre is also investigated. The modelling reproduces well the experimental results which shows that the use of strain hardening matrix can lead to reduced overall ductility. By means of post-processing of the results, it is shown that this reduction of ductility is strongly dependent on the interplay

between the ultimate matrix stress and ultimate steel stress.

Acknowledgements

First of all, I would like to express my full appreciation to Dr. Peter Grassl. This thesis can not be achieved without his patiently guidance, support and encouragement. Not only his profound knowledge affects me, but also his unending passion for science. His dedications to ensuring integrity, honesty, and transparency in all aspects of scientific problems served as shining examples for me to follow. His patience in answering my countless questions, no matter how basic or complex, has been invaluable. He has always been willing to take the time to explain concepts in multiple ways, ensuring that I fully comprehend them. I am deeply grateful for the opportunity being academic supervised by such a distinguished scholar and mentor. I believe what I learned from Dr. Peter Grassl will continue to guide me throughout my entire professional journey.

I also would like to express my appreciation to Antoine Marlot for his contribution to the work, and also Dr Ismail Aldellaa, Xiaowei Liu, Gumma Abdaliziz Hasan Abdelrhim and Ifiok Edem Epok, for their patience in answering my questions and discussing problems relating this thesis with me.

At last, I want to give my appreciation to my parents and Weiwei for their endless supporting and encouragement. Their wishes are motivation for me to move forward.

Notation

Latin symbols

a	Parameter for enforcing zero jump of the bridging stress at $\tilde{\delta} = \tilde{\delta}^*$
d_f	The diameter of fibers
E	Young's modulus of strain hardening cementitious composite
E_m	Young's modulus of cementitious matrix
E_f	Young's modulus of fibers
f	The snubbing coefficient
f_t	The tensile strength of the matrix
f_c	The compressive strength of the matrix
g	The snubbing factor
H_p	The hardening modulus of the plasticity part of CDPM2
h_e	The length of element
L	The embedment length
L_f	The length of fibers
N	The number of fibers within one element

$\bar{s}$	The average crack spacing at the stage of strain hardening
s_{m}	The saturated crack spacing
V_{f}	The volume fraction of fibers
V_{m}	The volume fraction of matrix
$V_{\mathrm{f,min}}$	The minimum fibre volume fraction related to fibers distribution variation
z	The distance form the centre of the fibre to the crack surface

Greek symbols

α	The fiber dispersion index
α_{min}	The lower limit of α
β	The slip hardening parameter
γ_{r0}	A ratio links the crack opening to the displacement at peak
γ_{cu}	A ratio links $\bar{\delta}_{\mathrm{cu}}$ to δ_{cu}, related to fibers distribution variation.
δ	Crack opening/Crack opening of weakest crack of the composite
$\bar{\delta}_{\mathrm{cu}}$	Average crack opening of when weakest crack reaches δ_{cu}
δ_0	The crack opening at the onset of slip
δ_{f}	The crack open threshold which controls the softening slope
$\delta_{\mathrm{cu}}^{\mathrm{un}}$	Crack opening of unloading cracks

$\tilde{\delta}$	The normalized crack opening(normalized by $\frac{L_f}{2}$)
$\tilde{\delta}^*$	The normalised crack opening at the end of the debonding stage
$\tilde{\delta}_{\mathrm{cu}}$	The normalised crack opening at onset of softening
ε_{p}	Irreversible inelastic strain part
$\varepsilon_{\mathrm{cr}}$	Inelastic strain part; Refering strain due to multiple cracks
ε_{cu}	The cracking strain at the peak of the bridging stress
ξ	A parameter controls the slope of sigmoid relation
$\bar{\boldsymbol{\sigma}}_{\mathrm{t}}$	The positive parts of the effective stress $\bar{\boldsymbol{\sigma}}$
$\boldsymbol{\sigma}$	The nominal stress
$\bar{\boldsymbol{\sigma}}$	The effective stress
$\bar{\boldsymbol{\sigma}}_{\mathrm{t}}$	The positive parts of the effective stress $\bar{\boldsymbol{\sigma}}$
$\bar{\boldsymbol{\sigma}}_{\mathrm{c}}$	The negative parts of the effective stress $\bar{\boldsymbol{\sigma}}$
σ_{f}	Fibre stress in direct tension
σ_{m}	Matrix stress in direct tension
σ_0	The reference stress at the end of debonding
$\tilde{\sigma}_{\mathrm{f}}^{\mathrm{debonding}}$	Fibre stresses due to debonding
$\tilde{\sigma}_{\mathrm{f}}^{\mathrm{pullout}}$	Fibre stresses due to pullout
$\tilde{\sigma}_{\mathrm{f}}$	The normalized fibre stress(normalized by σ_0)
$\tilde{\sigma}_{\mathrm{cu}}$	The normalised fibre stress at onset of softening

τ_0	The bond strength at the onset of slip
ϕ	The fibre inclination angle
ω_{t}	Tensile damage variables
ω_{c}	Compressive damage variables

Contents

List of Figures

Chapter 1

Introduction

1.1 Background

Concrete has been used as a structural material since 1800s. The performance of concrete has been improved to satisfy increasing demands for infrastructure. For example, taller and taller buildings lead the compressive strength required to increase from 30-40 MPa in 1940s to over 100 MPa nowadays. This is achieved with finer cement and superplastiziser. However, high strength alone is not adequate for high quality of infrastructures. Greenness of concrete production and durability of concrete are other important areas.

In recent decades, different high performance concrete recipes were developed for satisfying the increasing demands. The use of self-compacting and self-consolidating concrete reduces expenditure for repairs and increases the durability of structures. The use of recycled concrete as aggregates and ecological cement are helpful to the sustainability and greenness of concrete production.

Engineered Cementitious Composite (ECC) or Strain Hardening Cementitious Composite (SHCC) typically means a type of high performance fibre reinforced concrete with high strain capacity. Here, ECC is one type of SHCC. Compared with normal concrete, the advantages of this type material are outstanding. For normal concrete, the load capacity of structural concrete members is governed by interaction of steel reinforcement and concrete. On the one hand, the desired mechanical performance of the composite is only achieved when concrete cracks and a slip between concrete and reinforcement takes place. One the other hand, cracks due to the low tensile strength of concrete is the main disadvantage of structural concrete. Cracks create pathways for aggressive substances and reduce durability of structural concrete. Furthermore, under severe cyclic loading (e.g. due to earthquakes), large number of cracks could cause spalling of concrete cover of structural members (columns and shear walls), which could lead to buckling of axial steel reinforcement and loss of anchorage. In extreme situations, this can cause collapse of the entire structure. ECC's strain capacity could reach over 3 %. Higher ductility could reduce the spalling of this material when under cyclic loading. Fibres bridging ECC's cracks always result in small cracks, which reduce the pathways for aggressive substances and protect the steel reinforcement. Durability of structural members can be improve with the use of ECC.

However, some type of discontinuous fibres alter the crack spacing significantly which could lead to increased localised strains, which might negatively influence the ductility of continuously reinforced concrete. There are no design codes for structural fibre reinforced concrete, which considers the effect of fibres on the failure process. Not enough research has been carried out to investigate the interplay of continuous (traditional steel bars) and discontinuous (short fibres) reinforcement in concrete and its affect on the load bearing capacity and ductility of reinforced concrete.

Adding different discontinuous fibres to cementitious matrix can strongly affect ECC's mechanical behaviour. The bond interaction between fibre concrete and continuous steel reinforcement which can, if not designed correctly, have a negative effect on the capacity and ductility of steel reinforced ECC.

1.2 Aim and Objectives

The aim of this research is to model the failure process of ECC and to understand how normal reinforcement interacts with ECC.

Objectives of this research are to

- develop a 1D macroscopic model for ECC in tension based on micro-mechanics of the interaction of fibre and matrix.
- develop a 3D constitutive model suitable for FE computation for ECC.
- understand the interaction of steel reinforcement and ECC and its effect on ductility.

1.3 Contribution to the field

It is expected that this research contributes more to the understanding of SHCC and steel reinforced SHCC. Phenomenological models usually neglect the forming process of multiple cracks. A valid stress-strain relation based on micro-scale fibre properties is required. CDPM2F is a 3D FE constitutive model for SHCC, which is able to help us understand structural behaviour of SHCC. It also helps to

understand better the dominant factors which affect ductility and load capacity of steel reinforced ECC. This research provides guidance for R-ECC design.

1.4 Outline

This research is based on a plastic-damage approach to the modelling of the structural response of ECC and its interaction between ECC and steel reinforcement. This thesis is divided into six chapters, and the contents of each chapter are presented below:

Chapter 1, which is the present chapter, provides an introduction to the research, which shows the background of the research. It indicates that it is required to develop a valid micro-mechanical based model and that research on the interaction between steel and ECC should be carried out. Main aims and objectives of the study and the methodology in order to achieve the study's goals are summarised. Furthermore, the work's overall contribution to knowledge in the field is stated.

In Chapter 2, literature of relevant research is reviewed to explore key parameters that affect the overall structural response of strain hardening cementitious composites. Experimental studies of ECC structural behaviour (tension, compression, shearing) are presented. Theoretical and experimental research of fibres bridging at the micro scale are also reviewed.

In Chapter 3, a theoretical model of CDPM2F is described. It contains a reformulated fibre stress-cracking opening law and different relation of linking cracking strain and crack opening, which I used for both strain hardening and strain softening stages. Calibration of model based on fibre distribution variation is also discussed in this chapter.

Chapter 4 shows the single element response for different material parameters. Comparisons between experimental studies and modelling results for direct tension, compression and shearing are presented.

Validation of CDPM2F in modelling structural component for steel reinforced ECC under tension is shown in Chapter 5. Modelling results of steel reinforced concrete, steel reinforced ECC and steel reinforced low strength ECC are compared with experimental studies to reveal the different failure mechanism.

Chapter 6 gives conclusions, limitations, and recommendations for future work.

Chapter 2

Literature review

2.1 Mechanical behaviour of ECC

The mechanical behaviour of ECC is outstanding. ECC exhibits high ductility as its strain can reach over 3 %. Potentially, ECC could be an ideal constructional material because of its high ductility. In this section, the constituents of ECC, tensile, compressive and shear behaviour of ECC is presented via literature.

2.1.1 Constituents of ECC

ECC consists of a cementitious matrix mixed with short and thin fibres. Fibres are usually randomly distributed within ECC. This section shows what typical fibre materials and matrix materials are used in making ECC.

2.1.1.1 Fibre material and geometry

Various types of fibres are used in making ECC. Typical fibres of making ECC are Polyvinyl Alcohol (PVA) fibres, because of their good dispersibility, high tensile strength and good bond slip property. Tensile strength of PVA-ECC can reach up the range of 3 to 8 MPa and the tensile strain capacity can reach up to 5 %. The chemical bond between virgin fibres and matrix is considerably strong, due to hydrophilic property of PVA fibre (Yu et al., 2018). Other types of fibres such as Polyethylene (PE) fibres, Polypropylene (PP) fibres, steel fibres (SF) and glass fibres (GF) are also used in ECC. Stiffness of steel fibres and glass fibres are high compared with other fibres. They are usually used in hybrid with PE or PVA fibres. PE fibres with high strength and high Young's modulus have been recently used in producing high strength ECC. This is because for low chemical fibres/matrix bond strength and high slip hardening capacity, PE fibres with high strength may not be fractured during debonding stage. The ultimate tensile strength is also relatively high because of high slip hardening capacity. This leads to a high tensile strength of ECC, which can reach over 10 MPa (Ding et al., 2022).

Many researchers found that the slip hardening effect is also governed by the geometry of fibres. Long and thin fibres are required. However, if the length of fibres is too long, fibres might fracture before fibre pullout from the matrix occurs because of the high debonding force required. If the length of fibres is too short, there is not enough slip hardening capacity to generate high bridging capacity. For typical PVA-ECC, The length of PVA fibres used is 12 mm. The diameter of fibres is 39 μm (Li et al., 2023).

2.1.1.2 Matrix material

The matrix of ECC is cementitious with fine aggregate. Many admixtures are added to improve the performance of the matrix. For example, fly ash (class F) can improve the toughness and ductility of the matrix (Liu et al., 2018; Wang et al., 2020; Halvaei et al., 2013). Silica flume and metakolin can improve mechanical and durability properties (Liu et al., 2018; Madhavi et al., 2016). Ground granulated blast furnace slag can decrease permeability and increase durability and long-term strength. Superplastiser can improve ductility and tensile strength. Besides mineral admixtures, fine aggregates are used in making ECC. Another research shows crushed dolomitic limestone sands with a maximum size of 1.19 mm are used in making ECC. However, drying shrinkage is observed (Mustafa et al., 2009).

2.1.2 Tensile behaviour of ECC

ECC exhibits tensile hardening properties, which are due to the slip hardening effect when fibres are pulled out. Consequently, the fibre and matrix bond relation is very important. Other material parameters such as fibre length, fibre diameters, volume fraction of fibres, matrix strength, flaw size and distribution are also able to affect tensile behaviour of ECC. In this section, these factors are discussed based on literature.

2.1.2.1 Fibre/matrix bond

Bond slip property is the key factor of strain hardening behaviour. Slip hardening usually means that for one fibre being pulled out of the matrix, the pullout

force increases with slip. Fibres and matrix mentioned in sections 2.1.1.1 and section 2.1.1.2 usually exhibit slip hardening. On the other hand, steel fibres embedded in a cementitious matrix usually exhibit a slip softening response.

Researchers in Naaman and Shah (1976) have experimentally studied the pull out load and slip displacement relation of steel fibre/concrete matrix. The experimental set up is shown in Figure 2.1.

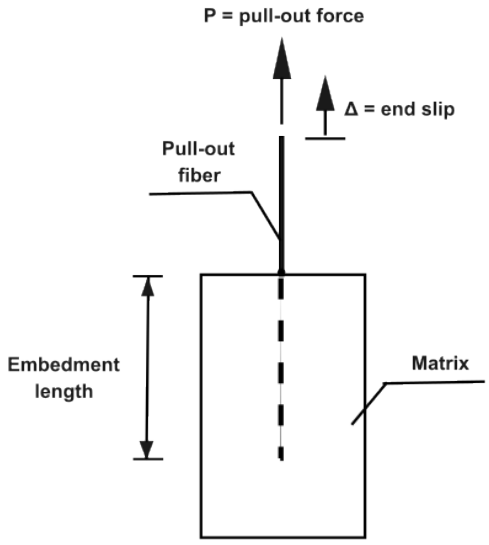

Figure 2.1: Typical single-steel fibre concentric pull-out test specimen.

A slip softening response is observed. In Maage (1978), it was found that the pullout force of single fibres is unaffected by the number of fibres. Naaman et al. (1989) found that additives can affect the bond strength of steel fibre/cementitious matrix. Latex can increase the steel fibre/cementitious matrix bond strength. Steel fibres with hook end can increase the pullout load during the pullout phase. However, steel fibres with hook ends still does not have slip hardening properties. The pullout force-slip displacement relation of steel fibres is shown in Figure 2.2.

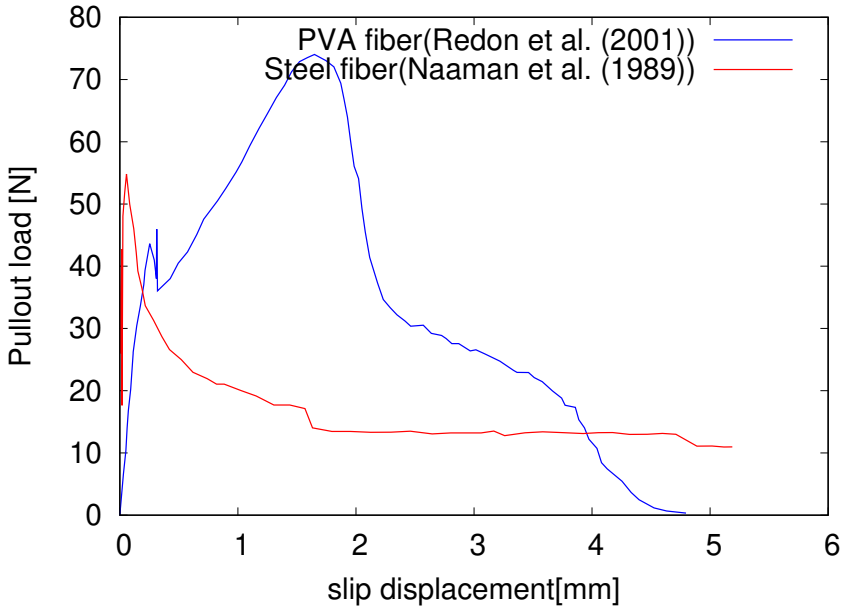

Figure 2.2: Comparison of pullout force-slip distance relation for single steel fibre and PVA fibre (Redon et al., 2001; Naaman et al., 1989).

Researchers in Marshall and Cox (1987) have found that PE fibres mixed with brittle cement based matrix have a pseudo strain hardening behaviour. Lin and Li (1997) proposed that the pseudo strain hardening behaviour of ECC is caused by the slip hardening property of spectra PE fibres/matrix bond. Redon et al. (2001) experimentally studied the pull out behaviour of a single PVA fibre from the cementitious matrix. The setup of experiment is shown in Figure 2.3.

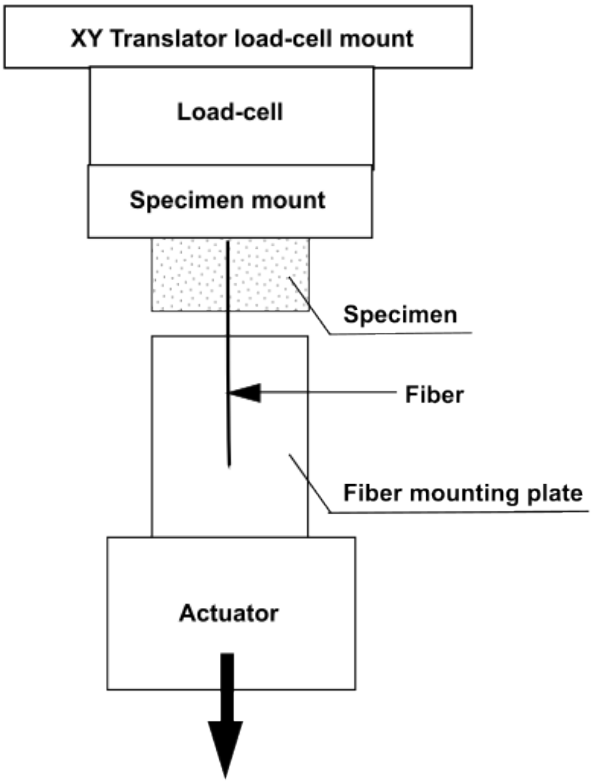

Figure 2.3: Scheme of the single PVA fibre pull-out test setup.

They found the reason of slip hardening property is that PVA fibres are peeled off by the cementitious matrix in the pull out phase. At the end of fibre embedment, fibres due to abrasion damage induce 'jam' effect. Pullout force increases due to this effect. The pullout force-slip displacement curve of steel fibres and PVA fibres is shown Figure 2.2. It shows slip hardening property of PVA fibre/cementitious matrix bond. Compared with steel fibres, PVA fibres have the potential to effectively increase ductility and tensile strength of the composite.

2.1.2.2 Geometry of fibre

Increasing bond stress of fibre/matrix interface causes strain hardening as mentioned in section 2.1.2.1. Geometry of fibres could affect the quantity of bond area between matrix and fibres, which also consequently influence the strain hardening capacity. Yu et al. (2018) shows that geometry of fibres affects peak stress and strain capacity of ECC. This effect is shown in Figure 2.4.

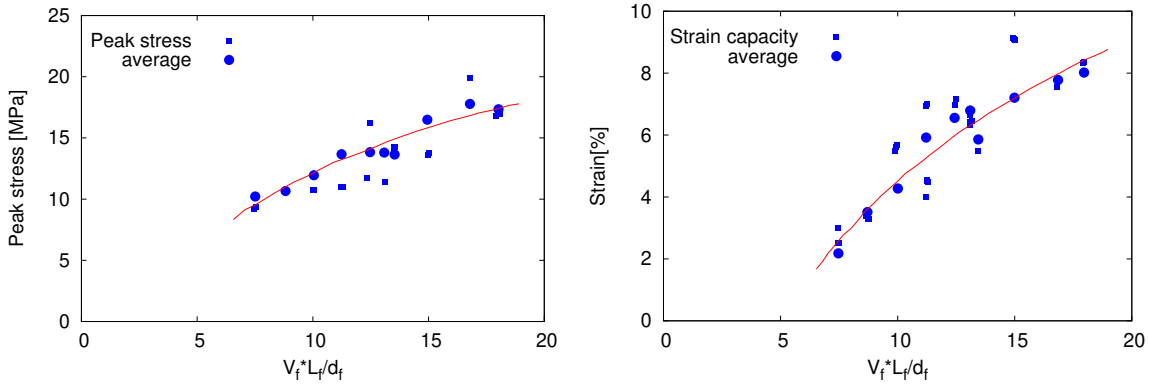

(a) (b)

Figure 2.4: Influence of fibre reinforced index on a) peak stress b) strain capacity (Yu et al., 2018).

V_f is the volume fraction of fibres, L_f is the length of fibres and d_f is the diameter of fibres. It shows that both tensile stress capacity and tensile strain capacity have positive correlation with fibre reinforced index ($\frac{V_\mathrm{f} L_\mathrm{f}}{d_\mathrm{f}}$). It indicates long and thin fibres are preferred to acquire higher ductility and higher tensile strength of ECC. Similar experiments carried out by Li et al. (2019) confirm this trend. Decreasing water/binder ratio enhances frictional strength of fibre/matrix bond.

2.1.2.3 Fibre dispersion

Fibre dispersion is another factor that affects tensile strain capacity and ultimate tensile strength of ECC material. Unlike material parameters mentioned before, fibre dispersion is usually related to the manufacturing process.

Li and Li (2013a) have experimentally studied the influence of fibres dispersion on strain capacity. A factor α is used to describe fibre dispersion. Definition of α is shown in equations 2.1 and 2.2:

$$\Phi(x) = \sqrt{\frac{\sum_{i=1}^{n}(x_i - \bar{x})^2}{n}}/\bar{x} \tag{2.1}$$

$$\alpha = \exp\left[-\Phi(x)\right] \tag{2.2}$$

Here, $\Phi(x)$ is coefficient of variation, x_i is the number of fibres in unit area. The variable $\bar{x}$ is the average number of fibres in unit area. Furthermore, n is the number of unit areas at a cross sectional cut of an ECC specimen. The experimental result of correlation between fibre dispersion and tensile capacity is shown in Figure 2.5. When α is approaching 1, the coefficient of variation is approaching 0. This limit implies that fibres can be considered uniformly distributed. Figure 2.5 shows that with α approaching 1, the strain capacity is also approaching its maximum.

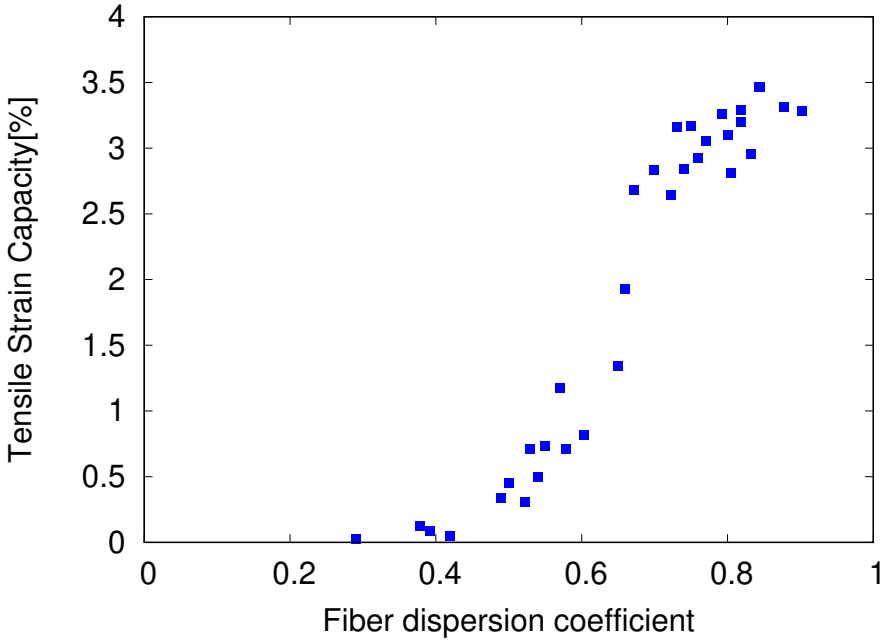

Figure 2.5: Correlation between fibre dispersion and tensile capacity (Li and Li, 2013a).

Zhou et al. (2012a) suggested holding back some amount of water to increase the plastic viscosity to the desired level when fibre was added. After fibres have been uniformly distributed, the rest of the water added. The mix sequence can enhance the uniformity of fibres distribution. The result of correlation between tensile capacity and fibre dispersion coefficient is shown in Figure 2.6. Same correlation between fibre dispersion and tensile capacity is observed.

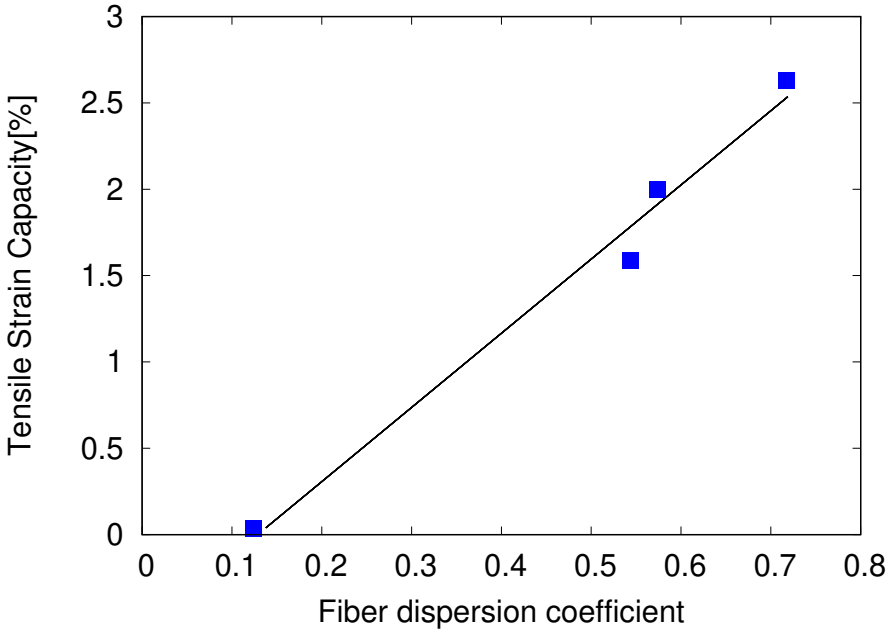

Figure 2.6: Correlation between fibre dispersion and tensile capacity (Zhou et al., 2012a).

2.1.2.4 Matrix flaw sizes distribution

Strain capacity and strength of ECC is also influenced by flaws added in cementitious matrix. It is shown that if artificial flaws are added, high strain capacity can be easily reached (Li and Wang, 2006).

Flaws in the ECC matrix can help with multiple crack process by decreasing tip toughness when a new crack forms. Strength of matrix is also related to flaw size at a crack plane as shown in Figure 2.7. It shows that cracking strength is decreasing with flaw size increasing. Critical value C_{mc} is the value of the flaw size when cracking strength of matrix is equal to fibre bridging strength. If flaw size at the new crack plane is larger than C_{mc}, a new crack could form as the fibre bridging stress is able to surpass the tensile strength of the matrix. When the flaw

size at a new crack plane is smaller then C_{mc}, a new crack may not be formed as the tensile strength of the matrix cannot be reached (Wang, 2005).

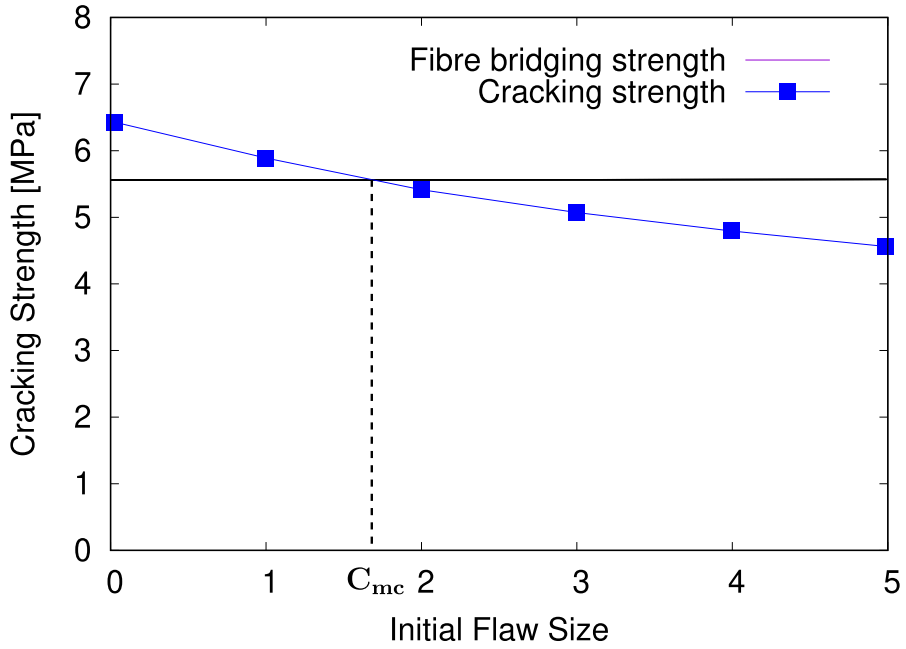

Figure 2.7: Matrix cracking strength and flaw size relation (Wang, 2005).

Therefore, strain capacity is also related to flaw sizes distribution. If enough large flaws exist in the matrix, new cracks can easily form until the saturated crack number is reached. In this way, a ECC specimen could reach its maximum tensile capacity. One way of achieving this is mixing artificial particles into the matrix. Normally, low strength particles with certain sizes are used in matrix as artificial particles. Evidence shows 7 % volume fraction artificial flaws with particle size of 3.5 μm to 0.2 mm mixed in matrix can increase the strain capacity from 0.4 % to 2.5 % (Li and Wang, 2006).

2.1.3 Compressive behaviour of ECC

Concrete is a type of constructional material with high compressive strength but low tensile strength. ECC material has a similar compressive property as concrete. Figure 2.8 shows compressive stress-strain curves of ECC with different compressive strength. The normal ECC compressive strength for structural applications ranges from 30 MPa to 70 MPa. For ultra high strength ECC, the compressive strength could reach over 150 MPa (Ding et al., 2022).

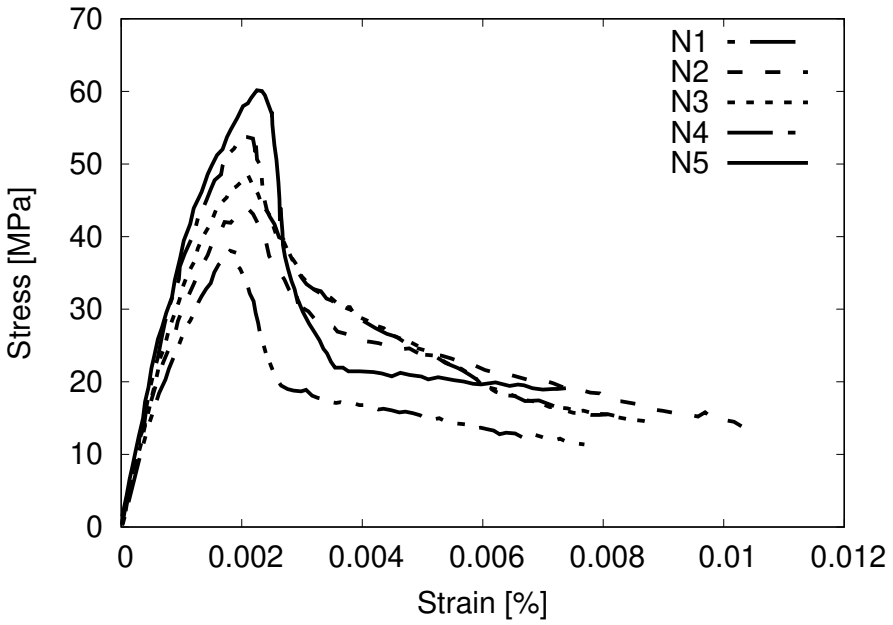

Figure 2.8: Compressive stress-strain curves of ECC with different compressive strength (J.Jia et al., 2015).

Typical compressive stress-strain curves is shown in Figure 2.8. N1 to N5 in Figure 2.8 represent compressive stress-strain curves of different compressive strength. Fibre bridging at vertical cracks lead to more ductile response compared to normal concrete. Like most cementitious materials, compressive strength of ECC is age dependent (shown in Figure 2.9). Type I cement is used in the experiment. Before

the age of 14 days, compressive strength increases rapidly. The age dependence of compressive strength of ECC is directly related to the rate of hydration of ECC's cementitious ingredients (Wang and Li, 2011).

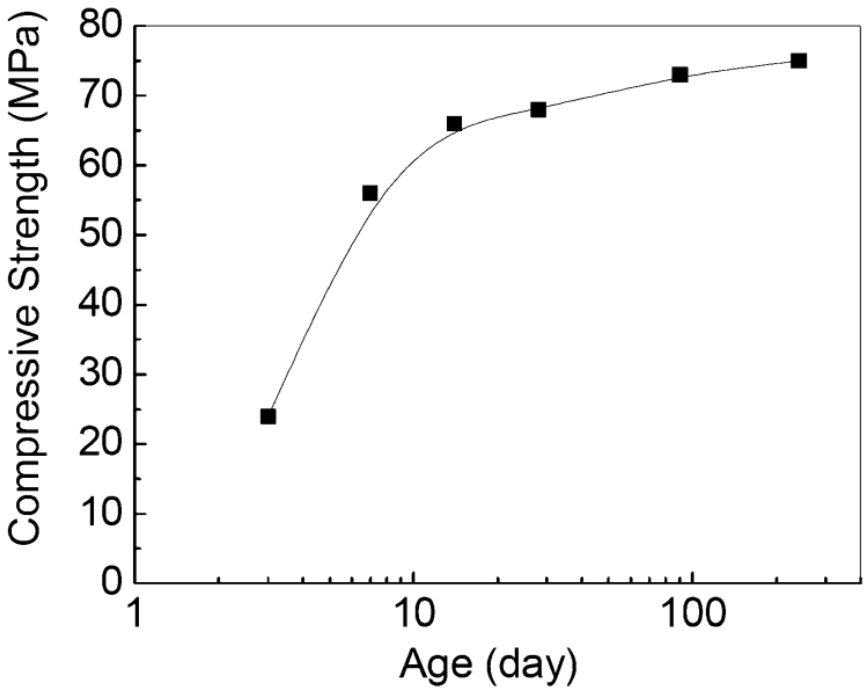

Figure 2.9: Age dependence of ECC's compressive strength (Wang and Li, 2011).

2.1.4 Shearing behaviour of ECC

Due to the ductile tensile response of ECC, the shear behaviour of ECC shows better performance than normal FRC material. Figure 2.10 gives the shear stress and strain curves for PE-ECC and FRC tested with Ohno shear beam.

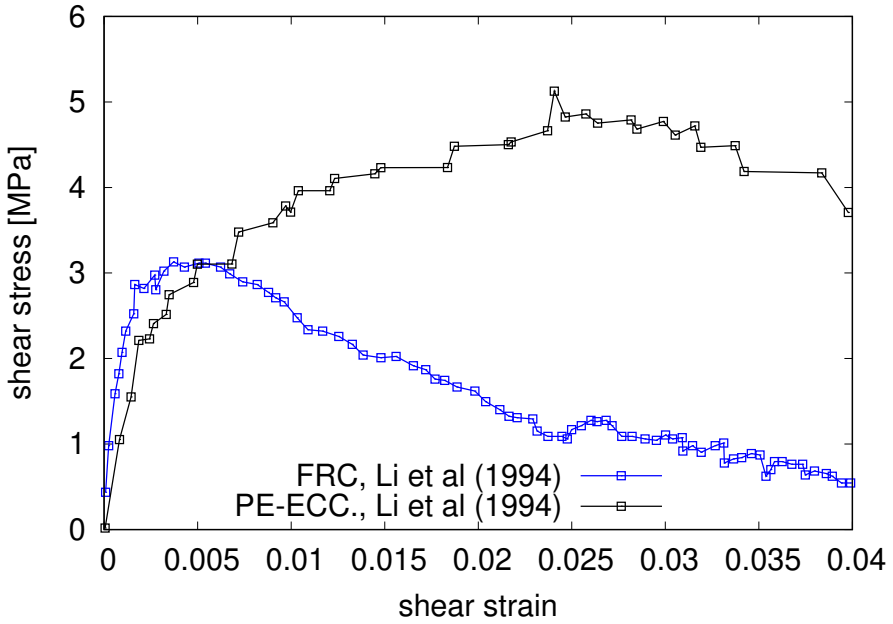

Figure 2.10: Shear performance of different cement based material tested with Ohno Shear Beam (Li et al., 2003).

For PE-ECC, both shear stress capacity and strain capacity reached is higher than FRC, which shows a more ductile response. Multiple cracks are observed at the middle part of the PE-ECC specimen (Li et al., 2003).

2.1.5 Structural tests of Reinforced ECC

Compared with normal concrete, ECC has higher tensile strength and better ductility. However, how the reinforcement interacts with ECC is the key point, which determines if ECC is a better construction material than concrete for steel reinfored structures. In the present description of the thesis, I use the abbreviation R for steel reinforcement, ECC for the ECC matrix materials and C for concrete matrix material. As an example, the abbreviation R-C stands for concrete matrix reinforced with steel. This notation will later also be used for the presentation of

the structural analyses. R-ECC (Reinforced Engineered Cementitous Composites) usually means ECC reinforced with normal steel reinforcement bars. R-ECC can potentially be applied for different structural members such as beams, columns and slabs.

Experimental comparison of load-strain curves of R-ECC and R-C tensile response is shown in Figure 2.11. It shows loading capacity of R-ECC is higher than R-C for tensile behaviour. However the strain capacity of R-ECC is lower than R-C (Moreno et al., 2014). Similar response was also observed by Liu et al. (2023) and Kang et al. (2017).

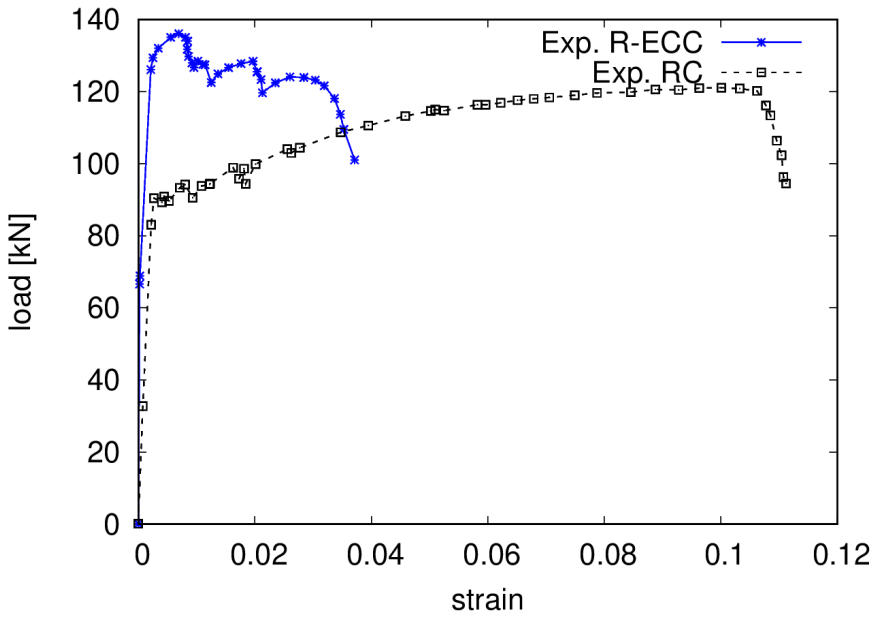

Figure 2.11: Tensile test for R/ECC and R/C (Moreno et al., 2014).

Moreno et al. (2014); Kang et al. (2017); Liu et al. (2023) investigated cracks distribution for R-ECC when reinforcement bar reaches fracture. Only one dominant crack is observed at onset of fracture of steel reinforcement in Moreno et al. (2014); Kang et al. (2017), but multiple dominant cracks were observed in Liu

et al. (2023). For the experiments in Moreno et al. (2014); Kang et al. (2017), the load capacity of R-ECC is higher than for R-C specimens.

2.2 1D theoretical models for ECC

The mechanical behaviour of ECC was discussed by means of different experimental studies within the literature in section 2.1. In this part, models for bridging capacity related to crack opening and multiple crack criteria based on micromechanical behaviour of ECC are introduced. Furthermore, the overall tensile stress-strain law obtained with numerical and phenomenological approaches in the literature are discussed.

2.2.1 Multiple cracks criteria

Naaman (1995) claimed that if the maximum post-cracking stress σ_0 is bigger than the cracking strength of matrix σ_{fc}, the material exhibits multiple cracking behaviour. Tetsushi and Li (2006) proposed energy criteria for flat crack propagation. It gives

$$\sigma_0\delta_0 - \int_0^{\delta_{ss}} \sigma(\delta)d\delta = J_b' \geq J_{tip} \tag{2.3}$$

It suggest that the maximum complementary energy J_{b}' must exceed the matrix toughness J_{tip} for flat crack propagation to prevail over that of the Griffith crack propagation mode, after a crack initiates from a flaw site. Both criteria provide design guidelines for fibre and matrix. Experimental data indicates that if $\sigma_0/\sigma_{\mathrm{fc}} \geq 1.3$ and $J_{\mathrm{b}}'/J_{\mathrm{tip}} \geq 2.7$, robust strain hardening of the ECC can be obtained (Kanda and Li, 2006b).

2.2.2 Fibre stress and crack opening relation

As mentioned before, the condition that the fibre stress at the crack surface surpasses the cracking strength and that the maximum complimentary energy exceeds the matrix toughness are two criteria for multiple cracks to be generated and strain hardening of ECC to be obtained.

Fibre stress capacity is the key factor for ECC tensile behaviour. In last decades, many researchers dedicated effort on developing fibre stress predictable model based on material properties of matrix, fibres and fibres/matrix interfaces. In this section, fibre stress-crack opening relation developed for predicting fibre stress, which is commonly used, is introduced.

Naaman et al. (1991) developed an analytical model for predicting shear stress of bond based on matrix/fibres interface properties, which link fibre bridging stress to material properties. LI (1992) derived a crack bridging model based on constant bond stress. This model is capable to predict fibre bridging stress-crack opening relation for both steel fibres and synthetic fibres reinforced cementitious composites within one model. Lin and Li (1997) implemented a linear slip hardening model for the increasing bond stress to fibre bridging model, which make it capable to predict tensile hardening response of ECC. Chemical bond is also further considered by Lin et al. (1999). Yang et al. (2008) modified the fibre bridging model for two way pullout. One way pullout refer fibres being pulled out at only one side of the crack surface, whereas two way is for both sides. The comparison of fibre stress-crack opening curves for two models in Lin et al. (1999) and Yang et al. (2008) is shown in Figure 2.12.

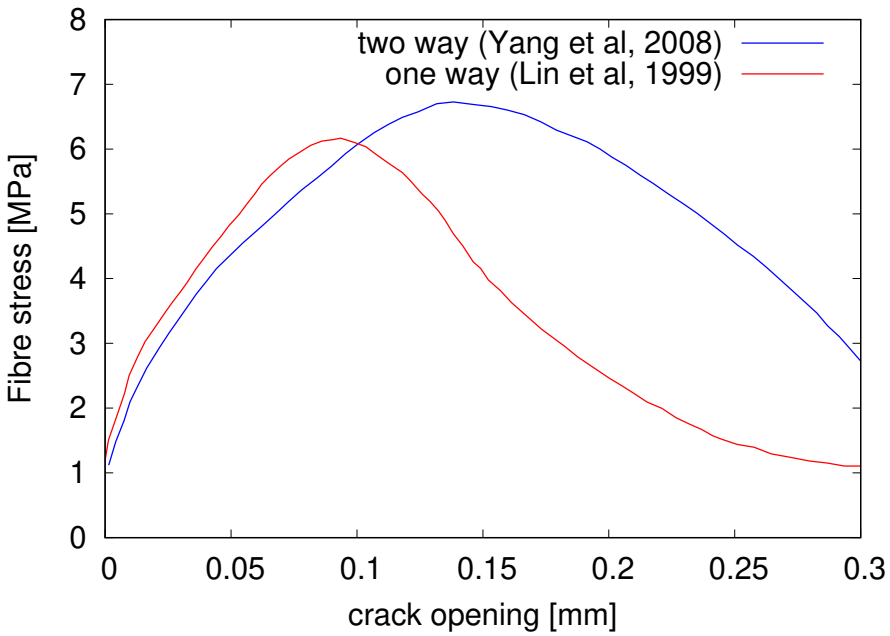

Figure 2.12: Theoretical bridging stress versus crack opening relation of PVA-ECC calculated by various models (Yang et al., 2008).

Huang et al. (2015) reformulated the fibre bridging law for hydrophilic fibres, which gives similar prediction as those obtained with the model proposed in Yang et al. (2008).

2.2.3 Tensile stress and strain law for ECC

ECC has pseudo strain-hardening properties as described in the former sections. Two typical stress and strain laws are commonly used within literature. Firstly, phenomenological stress and strain laws which can generally describe strain hardening properties but usually neglect the multiple crack forming process. Another is the numerical approaches based on micro-mechanical behaviour of each crack forming and unloading.

2.2.3.1 Phenomenological tensile stress and strain law

Phenomenological models are simplified models for the ECC tensile response. Strain hardening and softening responses are usually considered linear, which neglects the process of generating multiple cracks. The general stress and strain law is shown in Figure 2.13.

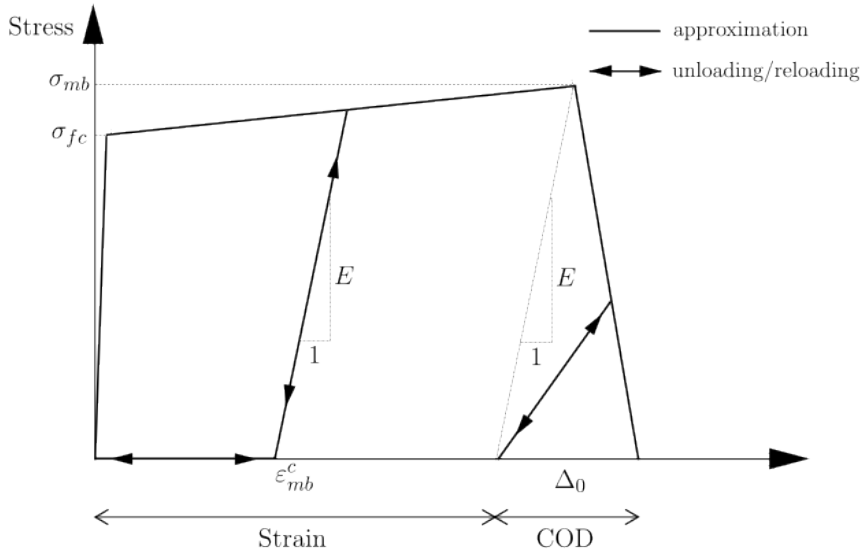

Figure 2.13: Approximation of a uniaxial tensile stress and strain relation of an ECC material (Kabele, 2000).

Many researchers have used stress and strain laws of varying complexity to analyse the structural response of components made of ECC. Kabele (2000) proposed an analytical model for ECC's structural behaviour, which includes a simplified tensile stress and strain law and shear bridging resistance based on a representative volume element. This model is able to predict the shear behaviour of ECC. COD/Δ_0 in Figure 2.13 refers to the strain induced with localised crack opening. Zhang et al. (2016) used a tensile phenomenological stress and strain law to evaluate shear failure behaviour of ECC. Ding et al. (2023) used a simplified stress and

strain law to model the seismic performance of ECC shell-RC columns. Bian et al. (2023) modelled the flexural performance of novel ECC-RC composite sandwich panels based on simplified stress and strain law. D.Liu et al. (2023) modelled the flexural behaviour of reinforced concrete (RC) beams strengthened with ECC with simplified stress and strain law considered. For the analysis of structural components made of ECC, simplified stress and strain laws are used frequently due to their ease to implement them into FE codes. However, the multiple cracking process and micro mechanical behaviour of fibres are usually neglected.

2.2.3.2 Numerical approaches

A multi-scale model of tensile response of ECC was proposed by Kabele (Kabele, 2007). Bridging stress prediction of matrix and fibres at the micro-scale were used to predict unloading and reloading of multiple cracks forming at the meso-scale. In recent research, cracks are idealised as springs to describe unloading and reloading phenomenon in Pan et al. (2023). A simplified fibre stress and crack opening relation is used and the debonding relation is considered to be linear for easy implementation. Variation of fibres is controlled with random volume fraction within governing range. The advantage of these methods lies in their ability to simulate the entire process of multiple crack formations.

2.3 3D computational models for ECC

In this section, computational mechanical approaches of modelling ECC in literature are introduced, which are continuum modelling approaches and discrete modelling approaches.

2.3.1 Continuum modelling approaches

The finite element method is usually used which is considered to be a continuum approaches of modelling ECC. FE models of ECC are already widely applied to simulate structural behaviour of R/ECC and ECC. Simplified tensile stress and strain laws in tension are usually implemented in FE codes to simulate 3D structural response. Examples of 3D applications are presented in Zheng and Zhang (2021), in which the bending behaviour of steel-ECC composite slab is considered. Kabir et al. (2022) modelled ECC encased steel composites beams. Yan et al. (2023) simulated concrete-filled steel tubes strengthened with CFRP grid-reinforced ECC. Kabir et al. (2022) simulated the CFST columns strengthened by CFRP grid-reinforced ECC under eccentric compression.

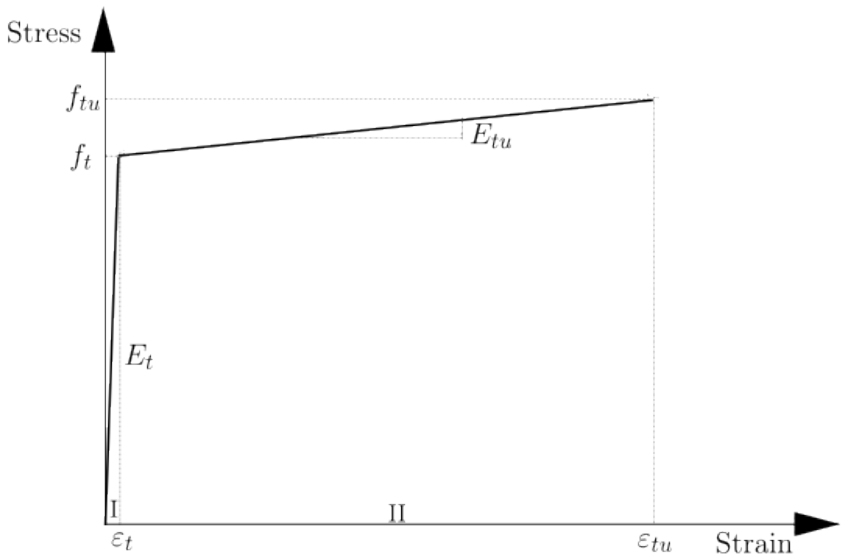

Figure 2.14: Bilinear constitutive model (Zhan et al., 2024).

Simplified tensile stress and strain laws have the benefit of easy implementation. Generally, they describe strain hardening behaviour of ECC well. However, the

explicit influence of micro-mechanical behaviour of fibres/matrix interface is usually neglected. Therefore, the input parameters of these models are usually not directly related to fibre properties.

2.3.2 Discrete modelling approaches

Rigid-body-spring models (RBSM) are often utilised in the modelling of the SHCC tensile response. Here, the matrix is modelled with rigid bodies. The bridging of fibres is modelled with springs. Usually every element has 6 degrees of freedom. At each boundary plane of element, 6 springs are placed. One spring is in normal direction to the boundary plane, two springs are in tangential direction to the boundary plane, and three springs are in the rotational directions. Mechanical properties of matrix (tensile strength, Young's modulus and fracture energy) are adopted at normal and tangential springs. Fibres are placed at boundary between rigid bodies. The springs are considered to have zero length. Slip-stress relation of fibre pulling out are adopted at these springs to calculate the fibre stress. For the randomly placed fibres, snubbing effects are also adapted for different orientations of fibres (Kunieda et al., 2010a,b; Ogura et al., 2013; Kang and J.E.Bolander, 2016).

Dispersion is controlled by varying the number of fibers at each boundary between rigid bodies. A sine function is adopted for describing the variance of number of fibres along the specimen length (Kang and J.E.Bolander, 2016). The weak section, which cracks first, usually corresponds to boundaries of rigid bodies with small number of fibres. The influence of fibre dispersion on RBSM is shown in Figure 2.15. P here represents the total pull out force, P_c represents the pull out force when the matrix reach cracking. Variable ϕ here refers the variation of fibers

distribution.

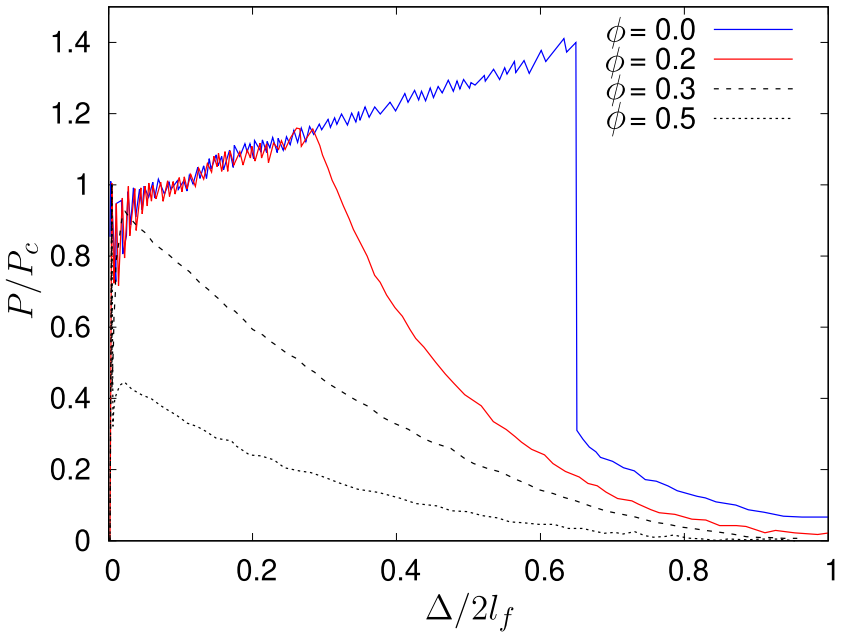

Figure 2.15: Influences of fibre dispersion on tensile behaviour of SHCC modelled by RBSM (Kang and J.E.Bolander, 2016).

2.3.3 Overview of CDPM2

CDPM2F is an extension of CDPM2, which is a 3D damage-plasticity approach of modelling the failure of concrete (Grassl et al., 2013). The way how CDPM2 was extended to obtain CDPM2F s introduced in 3.3.2. CDPM2 is a 3D damage-plasticity approach of modelling the failure of concrete (Grassl et al., 2013). An overview of CDPM2 is introduced in this section. The damage plasticity constitutive model is based on the following stress–strain relationship:

$$\boldsymbol{\sigma} = (1 - \omega_{\mathrm{t}})\,\bar{\boldsymbol{\sigma}}_{\mathrm{t}} + (1 - \omega_{\mathrm{c}})\,\bar{\boldsymbol{\sigma}}_{\mathrm{c}} \tag{2.4}$$

Here, ω_{t} and ω_{c} are the tensile and compressive damage variables, respectively. Furthermore, $\bar{\boldsymbol{\sigma}}_{\mathrm{t}}$ and $\bar{\boldsymbol{\sigma}}_{\mathrm{c}}$ are the positive and negative parts of the effective stress $\bar{\boldsymbol{\sigma}}$, respectively. The two parts of the effective stress are determined from the principal components of the effective stress $\bar{\boldsymbol{\sigma}} = \mathbf{D}_{\mathrm{e}}\,(\boldsymbol{\varepsilon} - \boldsymbol{\varepsilon}_{\mathrm{p}})$. Here, $\mathbf{D}_{\mathrm{e}}$ is the elastic stiffness, $\boldsymbol{\varepsilon}$ is the strain and $\boldsymbol{\varepsilon}_{\mathrm{p}}$ is the plastic strain. The plasticity model is based on the effective stress, which is independent of damage. The model is described by the yield function, the flow rule, the evolution law for the hardening variable and the loading–unloading conditions. The form of the yield function is

$$f_p(\bar{\boldsymbol{\sigma}}, \kappa_p) = F(\bar{\boldsymbol{\sigma}}, q_{h1}, q_{h2}) \tag{2.5}$$

The yield function

$$f_p(\bar{\sigma}_V, \bar{\rho}, \bar{\theta}; \kappa_p) = \{[1-q_{h1}(\kappa_p)](\frac{\bar{\rho}}{\sqrt{6}f_c}+\frac{\bar{\sigma}_V}{f_c})^2+\sqrt{\frac{3}{2}}\frac{\bar{\rho}}{f_c}\}^2+q_{h1}^2(\kappa_p)(\frac{m_0\bar{\rho}}{\sqrt{6}f_c}+\frac{m_g(\bar{\sigma}_V,\kappa_p)}{f_c}) \tag{2.6}$$

where $q_{h1}(\kappa_p)$ and $q_{h2}(\kappa_p)$ are dimensionless functions controlling the evolution of the size and shape of the yield surface. The flow rule is

$$\dot{\boldsymbol{\varepsilon}}_p = \dot{\lambda}\frac{\partial g_p}{\partial \bar{\boldsymbol{\sigma}}}(\bar{\boldsymbol{\sigma}}, \kappa_p) \tag{2.7}$$

where $\dot{\varepsilon_p}$ is the rate of the plastic strain, $\dot{\lambda}$ is the rate of the plastic multiplier and g_p is the plastic potential. The rate of the hardening variable κ_p is related to the rate of the plastic strain by an evolution law. The loading–unloading conditions are

$$f_p \leq 0, \quad \dot{\lambda} \geq 0, \quad \dot{\lambda} f_p = 0 \tag{2.8}$$

The damage part of the model is described by the damage loading functions, loading unloading conditions and the evolution laws for damage variables for tension

and compression. For tensile damage, the main equations are

$$f_{dt} = \tilde{\varepsilon}_t(\bar{\boldsymbol{\sigma}}) - \kappa_{dt} \tag{2.9}$$

$$f_{dt} \leq 0, \quad \dot{\kappa}_{dt} \geq 0, \quad \dot{\kappa}_{dt} f_{dt} = 0 \tag{2.10}$$

$$\omega_t = g_{dt}(\kappa_{dt}, \kappa_{dt1}, \kappa_{dt2}) \tag{2.11}$$

For CDPM2F, $\omega_t(\kappa_{dt}, \kappa_{dt1}, \kappa_{dt2})$ is modified based on the derivation in 3.3.2. For compression, main equations are

$$f_{dc} = \alpha_c \tilde{\varepsilon}_c(\bar{\boldsymbol{\sigma}}) - \kappa_{dc} \tag{2.12}$$

$$f_{dc} \leq 0, \quad \dot{\kappa}_{dc} \geq 0, \quad \dot{\kappa}_{dc} f_{dc} = 0 \tag{2.13}$$

$$\omega_c = g_{dc}(\kappa_{dc}, \kappa_{dc}, \kappa_{dc2}) \tag{2.14}$$

Here, f_{dt} and f_{dc} are the loading functions, $\tilde{\varepsilon}_c(\bar{\boldsymbol{\sigma}})$ and $\tilde{\varepsilon}_t(\bar{\boldsymbol{\sigma}})$ equivalent strains and κ_{dt}, κ_{dt1}, κ_{dt2}, κ_{dc}, κ_{dc} and κ_{dc2} are damage history variables. Furthermore, α_c is a variable that distinguishes between tensile and compressive loading.

Chapter 3

A damage plastic approach of modeling ECC

In the previous chapter, factors affecting tensile behaviour of strain hardening cementitious composites were described via a literature review. Some parameters are at the micro level and other parameters are related to manufacturing. In this chapter, the new constitutive model CDPM2F is presented, which is an extension of CDPM2 (Grassl et al., 2013).

3.1 Fibre stress versus crack opening

In this section, the model for the fibre stress versus crack opening $\sigma_{\mathrm{f}}(\delta)$ is derived. The model is an adjustment of the approach presented in Lin and Li (1997) to make it suitable for the iterative solution process used in this study. First, the original approach in Lin and Li (1997) is summarised and then our modification

is introduced.

3.1.1 Original model by Lin and Li (1997)

I present here in compact form the equations reported in Lin and Li (1997), which are then used in the continuum based damage-plasticity approach CDPM2F.

In Lin and Li (1997), the pullout force P of a single fibre crossing a single crack is given as a function of the displacement δ at the end of the fibre, which is loaded as

$$P(\delta) = \begin{cases} \dfrac{\pi d_{\mathrm{f}}^2 \tau_0 (1+\eta)}{\omega} \sqrt{\left(1 + \dfrac{c\delta}{L_{\mathrm{f}}}\right)^2 - 1} & \text{if } 0 \le \delta \le \delta_0 \\ \dfrac{\pi d_{\mathrm{f}}^2 \tau_0 (1+\eta)}{\omega} \left[\sinh\left(\omega \dfrac{L}{d_{\mathrm{f}}}\right) - \sinh\left(\dfrac{\omega(\delta - \delta_0)}{d_{\mathrm{f}}}\right)\right] & \text{if } \delta_0 \le \delta \le L \\ \quad + \pi \tau_0 \beta (1+\eta)(\delta - \delta_0)(L - (\delta - \delta_0)) & \\ 0 & \text{if } L \le \delta \end{cases} \tag{3.1}$$

where $L = L_{\mathrm{f}}/2 - z/\cos(\phi)$ is the embedment length. For the one-sided pull-out process considered here, the displacement of the loaded-end of the fibre is the same as the crack opening. Here, z is the distance from the centre of the fibre to the crack surface and ϕ is the fibre orientation. Furthermore, τ_0 is the bond strength at the onset of slip, β is the hardening parameter, d_{f} is the diameter of the fibre and $c = \beta L_{\mathrm{f}}/(2d_{\mathrm{f}})$. At the displacement threshold

$$\delta_0 = \frac{L_{\mathrm{f}}}{c}\left(\cosh\left(\frac{\omega L}{d_{\mathrm{f}}}\right) - 1\right) \tag{3.2}$$

the debonding process is completed.

In (3.1),

$$\eta = \frac{V_{\mathrm{f}} E_{\mathrm{f}}}{V_{\mathrm{m}} E_{\mathrm{m}}} \tag{3.3}$$

and

$$\omega = \sqrt{4\,(1+\eta)\,\beta\tau_0 / E_{\mathrm{f}}} \tag{3.4}$$

where E_{f} and E_{m} are Young's moduli and V_{f} and $V_{\mathrm{m}} = 1 - V_{\mathrm{f}}$ are volume fractions of fibre and concrete matrix, respectively. For my modified model described in section 3.1.2, a spatial variation of the fibre distribution is considered, which is explained in the calibration part of section 3.2. In Lin and Li (1997), it is assumed that one-sided pullout occurs. Therefore, the pullout displacement is equal to the crack opening. The pullout force versus crack opening is shown in Figure 3.1a for $z = 0$ and $\phi = 0$, where the displacement (crack opening) is normalised by dividing it with $L_{\mathrm{f}}/2$ and the force is normalised by dividing it with the force at δ_0. The expression in (3.1) was derived in Lin and Li (1997) based on the assumption that the fibre is rigid. Therefore, for plotting Figure 3.1a, the stiffness ratio $E_{\mathrm{f}}/E_{\mathrm{m}}$ was set to 200 so that the force approaches zero at a displacement of $L_{\mathrm{f}}/2$. As

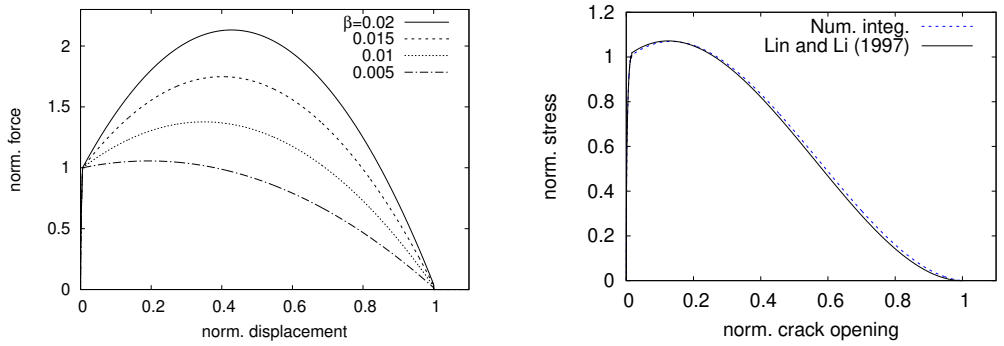

(a) (b)

Figure 3.1: Original fibre model according to Lin and Li (1997): a) normalised pullout force versus normalised crack opening. b) average fibre stress versus crack opening computed from (3.6) and numerical integration of (3.5).

seen in Figure 3.1a, the response is strongly influenced by the parameter β, which controls the hardening response at the fibre scale (Lin and Li, 1997). The greater β is, the greater is the crack opening at which the maximum bridging stress is reached. This parameter enters the expression of c, which will play an important part in the development of our model in section 3.2.

The bridging stress σ_f acting on a crack surface as function of the crack opening δ was proposed in Lin and Li (1997) as

$$\sigma_\mathrm{f} = \frac{4V_\mathrm{f}}{\pi d_\mathrm{f}^2} \int_{\phi=0}^{\pi/2} \int_{z=0}^{(L_\mathrm{f}/2)\cos\phi} P\left(\delta\right) g\left(\phi\right) p\left(\phi\right) p(z) \mathrm{d}z \mathrm{d}\phi \tag{3.5}$$

Here, L_f is the fibre length and $P\left(\delta\right)$ is the pullout force of one fibre across one crack. Furthermore, $p\left(\phi\right) = \sin\phi$ is the probability density function of inclination angle ϕ, $g\left(\phi\right) = \exp\left(f\phi\right)$ which includes the snubbing factor f, and $p(z) = 2/L_\mathrm{f}$ is the probability density function of the shortest distance from the centre of fibre to the crack plane.

Integrating (3.5) numerically is computationally demanding, if it has to be carried out many times within finite element simulations. Lin and Li (1997) derived an approximate closed-form solution of (3.5) as

$$\tilde{\sigma}_f = \frac{\sigma_f}{\sigma_0} = \begin{cases} \dfrac{2}{k}\left[1 - \dfrac{1}{k}\cosh^{-1}\left(1 + \lambda\dfrac{\tilde{\delta}}{\tilde{\delta}^*}\right)\right]\sqrt{\left(1 + \lambda\dfrac{\tilde{\delta}}{\tilde{\delta}^*}\right)^2 - 1} + \dfrac{2\lambda\tilde{\delta}}{k^2\tilde{\delta}^*} & \text{if } 0 \le \tilde{\delta} \le \tilde{\delta}^* \\ \left(1 + c\tilde{\delta}\right)\left(1 - \tilde{\delta}\right)^2 & \text{if } \tilde{\delta}^* \le \tilde{\delta} \le 1 \\ 0 & \text{if } 1 \le \tilde{\delta} \end{cases} \tag{3.6}$$

where $\tilde{\delta} = 2\delta/L_\mathrm{f}$ is the normalised crack opening and $k = \omega L_\mathrm{f}/\left(2d_\mathrm{f}\right)$. Furthermore,

the reference stress at the end of debonding without hardening is

$$\sigma_0 = \frac{1}{2} g \tau_0 V_\mathrm{f} (1+\eta) L_\mathrm{f} / d_\mathrm{f} \tag{3.7}$$

The normalised crack opening at the end of the debonding stage is

$$\tilde{\delta}^* = \frac{2\lambda}{c} \tag{3.8}$$

where

$$\lambda = \cosh(k) - 1 \tag{3.9}$$

Furthermore,

$$g = \frac{2}{4+f^2} \left(1 + \exp(\pi f/2)\right) \tag{3.10}$$

A comparison of the numerical integration of (3.5) and the approximate solution in (3.6) is shown in Figure 3.1b. It can be seen that (3.6) is overall in good agreement with the numerical integration. However, there is a jump in the curve predicted by (3.6), which can produce numerical difficulties if (3.6) is used as part of an iterative approach within a constitutive model for finite element analysis. This problem is addressed in the next section.

3.1.2 Reformulate fibre stress-crack opening law

The approximate solution of the fibre bridging stress in (3.6) exhibits a jump at $\tilde{\delta} = \tilde{\delta}^*$ as shown in Figure 3.2a and b, which results in numerical problems when the bridging stress in (3.6) is used within the damage-plasticity model in (3.43) to determine the damage variable iteratively. The jump is present because of simplifications in the integration of (3.5) for the pullout part of the fibres. For

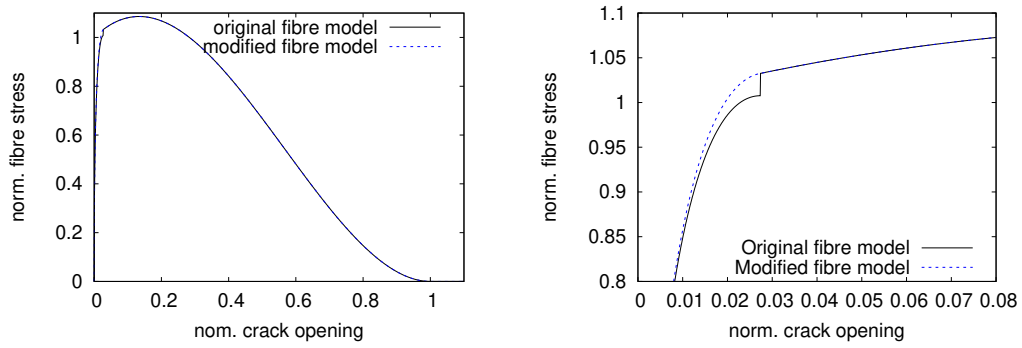

(a) (b)

Figure 3.2: Fibre stress versus crack opening for approximate relation with jump at $\tilde{\delta} = \tilde{\delta}^*$ and proposed modification without jump: a) full curve, b) zoom to area around $\tilde{\delta} = \tilde{\delta}^*$.

$0 \leq \tilde{\delta} \leq \tilde{\delta}^*$, the bridging stress in (3.5) is composed of

$$\tilde{\sigma}_{\mathrm{f}} = \tilde{\sigma}_{\mathrm{f}}^{\mathrm{debonding}} + \tilde{\sigma}_{\mathrm{f}}^{\mathrm{pullout}} \tag{3.11}$$

Here $\tilde{\sigma}_{\mathrm{f}}^{\mathrm{debonding}}$ and $\tilde{\sigma}_{\mathrm{f}}^{\mathrm{pullout}}$ are fibre stresses due to debonding and pullout, respectively, which are present before all fibres are debonded. The pullout part is represented in (3.6) by the term

$$\tilde{\sigma}_{\mathrm{f}}^{\mathrm{pullout}} = 2\lambda\tilde{\delta}/(k^2\tilde{\delta}^*) \tag{3.12}$$

Furthermore, $\tilde{\sigma}^{\mathrm{debonding}} = 0$ at $\tilde{\delta} = \tilde{\delta}^*$ since $\tilde{\delta}^*$ is the crack opening at which all fibres are fully debonded. Therefore, I propose to resolve this jump by adding a linear function to the pullout part so that the new pullout part of the bridging stress for $\tilde{\delta} \leq \tilde{\delta}^*$ as

$$\tilde{\sigma}_{\mathrm{f}}^{\mathrm{pullout}} = 2\lambda\tilde{\delta}/(k^2\tilde{\delta}^*) + a\tilde{\delta}/\tilde{\delta}^* \tag{3.13}$$

Here, the parameter a is determined by enforcing zero jump of the bridging stress expressions for $\tilde{\delta} \leq \tilde{\delta}^*$ and $\tilde{\delta} \geq \tilde{\delta}^*$ at $\tilde{\delta} = \tilde{\delta}^*$, which results in

$$2\lambda/k^2 + a = \left(1 + c\tilde{\delta}^*\right)\left(1 - \tilde{\delta}^*\right)^2 \tag{3.14}$$

Solving (3.14) for a gives

$$a = \left(1 + c\tilde{\delta}^*\right)\left(1 - \tilde{\delta}^*\right)^2 - 2\lambda/k^2 \tag{3.15}$$

so that the new expression for the pullout part of the bridging stress is

$$\tilde{\sigma}^{\text{pullout}} = 2\lambda\tilde{\delta}/(k^2\tilde{\delta}^*) + \left[\left(1 + c\tilde{\delta}^*\right)\left(1 - \tilde{\delta}^*\right)^2 - 2\lambda/k^2\right]\tilde{\delta}/\tilde{\delta}^* \tag{3.16}$$

This is a function of fibre and matrix parameters only. Consequently, the bridging stress formulation that I use for this work is

$$\tilde{\sigma}_f = \frac{\sigma_f}{\sigma_0} = \begin{cases} \dfrac{2}{k}\left[1 - \dfrac{1}{k}\cosh^{-1}\left(1 + \lambda\dfrac{\tilde{\delta}}{\tilde{\delta}^*}\right)\right]\sqrt{\left(1 + \lambda\dfrac{\tilde{\delta}}{\tilde{\delta}^*}\right)^2 - 1} + & \\ \dfrac{2\lambda\tilde{\delta}}{k^2\tilde{\delta}^*} + \left[\left(1 + c\tilde{\delta}^*\right)\left(1 - \tilde{\delta}^*\right)^2 - 2\lambda/k^2\right]\tilde{\delta}/\tilde{\delta}^* & \text{if } 0 \leq \tilde{\delta} \leq \tilde{\delta}^* \\ \left(1 + c\tilde{\delta}\right)\left(1 - \tilde{\delta}\right)^2 & \text{if } \tilde{\delta}^* \leq \tilde{\delta} \leq 1 \\ 0 & \text{if } 1 \leq \tilde{\delta} \end{cases} \tag{3.17}$$

which provides a reasonable agreement with the solution obtained from the numerical integration.

3.2 Linking between cracking strain and crack opening

The aim of the present work is to incorporate a micro-mechanics based fibre model into a macroscopic constitutive model, which is based on stress strain relations and in which the inelastic processes are represented by a cracking strain as a function of a damage variable. Therefore, it is required a link of the crack opening δ to the cracking strain $\varepsilon_{\mathrm{cr}}$ used in (3.43).

As mentioned before, ECC materials subjected to tension exhibit distributed cracking, because of the slip hardening pullout response of individual fibres. For displacements greater than the displacement at which the bridging stress reaches its maximum, softening occurs which is accompanied by the formation of a single localised crack. For converting crack opening to cracking strain, we are required to know the crack opening at which the softening process starts. With this information, I use then the crack band approach for the localised part of the cracking response, i.e. I scale the cracking strain with respect to the element length to obtain mesh independent results (Bažant and Oh, 1983). I assume that the matrix is very brittle in comparison to the fibre response. This means that at the onset of softening the stress in the concrete is already zero. Thus, the condition for softening is given by the fibre response only.

Independently of c, the debonding phase exhibits always hardening so that the earliest that softening can occur is when $\tilde{\delta} = \tilde{\delta}^*$. Therefore, we can focus our attention on the part of the fibre stress function in which $\tilde{\delta} \geq \tilde{\delta}^*$. For softening to occur, the condition $\mathrm{d}\tilde{\sigma}_f/\mathrm{d}\tilde{\delta} = 0$ has to be met. Differentiating $\tilde{\sigma}_{\mathrm{f}}$ in (3.17) with

respect to $\tilde{\delta}$ for $\tilde{\delta} \geq \tilde{\delta}^*$ and setting it to zero results in

$$\frac{\mathrm{d}\tilde{\sigma}_f}{\mathrm{d}\tilde{\delta}} = \left(\tilde{\delta} - 1\right)\left(3c\tilde{\delta} - c + 2\right) = 0 \tag{3.18}$$

Let us first study the case that softening occurs at the end of debonding. Setting $\tilde{\delta} = \tilde{\delta}^*$ into (3.18) and using the expression for $\tilde{\delta}^*$ in (3.8), we obtain a condition for the onset of softening at $\tilde{\delta} = \tilde{\delta}^*$, which is $c = 6\lambda + 2$. Therefore, for $c \leq 6\lambda + 2$ softening occurs at the end of debonding, i.e. $\tilde{\delta}_{\mathrm{cu}} = \tilde{\delta}^* = 2\lambda/c$. On the other hand, for $c > 6\lambda+2$, softening will occur when the condition $\mathrm{d}\bar{\sigma}_f/\mathrm{d}\tilde{\delta} = 0$ is met for $\tilde{\delta} > \tilde{\delta}^*$. The present study is limited to fibre arrangements which exhibit strain hardening beyond $\tilde{\delta} > \tilde{\delta}^*$, i.e. $c > 6\lambda + 2$. For this case, the displacement at the onset of softening $\tilde{\delta} = \tilde{\delta}_{\mathrm{cu}}$ is obtained by solving (3.18), which gives $\tilde{\delta}_{\mathrm{cu}} = (c-2)\,/\,(3c)$. The other solution to (3.18) is that $\tilde{\delta} = 1$, which is the case of complete pullout and is not of interest here.

Therefore, the critical displacement at which softening occurs is

$$\tilde{\delta}_{\mathrm{cu}} = \begin{cases} 2\lambda/c & \text{if } c \leq 6\lambda + 2 \\ (c-2)\,/\,(3c) & \text{if } c > 6\lambda + 2 \end{cases} \tag{3.19}$$

The corresponding critical stress $\tilde{\sigma}_{\mathrm{cu}}$ is obtained by setting (3.19) into (3.17) which results after mathematical manipulations in

$$\tilde{\sigma}_{\mathrm{cu}} = \begin{cases} (1+2\lambda)\,(2\lambda/c - 1)^2 & \text{if } c \leq 6\lambda + 2 \\ \dfrac{4\,(c+1)^3}{27c^2} & \text{if } c > 6\lambda + 2 \end{cases} \tag{3.20}$$

The information about $\tilde{\delta}_{\mathrm{cu}}$ and $\tilde{\sigma}_{\mathrm{cu}}$ can now be used to develop a link between the cracking strain $\varepsilon_{\mathrm{cr}}$ and the crack opening δ.

Three different links between cracking strain and the crack opening are proposed, which are called Constant, Linear and Sigmoid. These links are compared with experimental results reported in (Paul and Zijl, 2013). At the end, the Sigmoid relation is adapted in CDPM2F due to its ease of use and good agreement with experimental results.

3.2.1 Constant relation

The assumption of constant relation is that saturated crack spacing is reached directly at the onset of crack formation, i.e.

$$\bar{s}(\varepsilon_{cr}) = s_m \tag{3.21}$$

$\bar{s}$ is the average crack spacing which is related to cracking strain. The number of cracks does not change during the hardening process. In this case, $\bar{s}$ is also constant within hardening stage. With the calibration of fibre dispersion described in section 3.3.3, the relation between crack opening and cracking strain is

$$\delta(\varepsilon_{cr}) = \frac{\varepsilon_{cr} s_m}{\gamma_{cu}} \qquad if \quad 0 < \varepsilon_{cr} \leq \varepsilon_{cu} \tag{3.22}$$

The validation of constant relation compared to experiment research (Paul and Zijl, 2013) is shown in Figure 3.3 and Figure 3.4. This model shows poor correlation to experimental data, which indicates that a δ-ε_{cr} relation based on the formation of multiple cracks is required.

3.2.2 Linear Relation

Based on the observation of experimental research by Paul and Zijl (2013) shown in Figure 3.3, a linear relation between number of cracks per unit length and strain is investigated. Number of cracks within unit length is considered equal to $\frac{1}{h_e}$ at onset of crack forming, and equal to $\frac{1}{S_m}$ once the maximum stress capacity is reached. Two equations can be written for a single element:

$$\begin{cases} \frac{N(\varepsilon_{cr}=0)}{h_e} = \frac{1}{h_e} \\ \frac{N(\varepsilon_{cr}=\frac{\gamma_{cu}\delta_{cu}}{S_m})}{h_e} = \frac{1}{S_m} \end{cases} \tag{3.23}$$

Where h_e is the element length. The linear relation is based on experimental study shown in Figure 3.3. The number of cracks per unit length versus cracking strain relation can be derived as:

$$\frac{N(\varepsilon_{cr})}{h_e} = \frac{(h_e - S_m)\varepsilon_{cr} + \gamma_{cu}\delta_{cu}}{\gamma_{cu}\delta_{cu}h_e} \tag{3.24}$$

Next, we know for one element that we can link crack opening to cracking strain as

$$N(\varepsilon_{cr})\delta(\varepsilon_{cr}) = h_e\varepsilon_{cr} \tag{3.25}$$

Therefore, the formula linking cracking strain and crack opening based on the linear relation is

$$\delta(\varepsilon_{cr}) = \frac{\varepsilon_{cr}h_e}{(\frac{(h_e-S_m)\varepsilon_{cr}}{\gamma_{cu}\delta_{cu}} + 1)\gamma_{cu}} \quad \text{if } 0 < \varepsilon_{cr} \leq \varepsilon_{cu} \tag{3.26}$$

The predictions of the number of cracks per unit length and the average crack width obtained by the linear model agrees well with the experimental research in

Figure 3.3 and Figure 3.4. The average crack width-cracking strain evolution agrees with the experimental phenomenon. However, the average crack width increases rapidly with the strain increasing at begining, which leads to a high stiffness. It is unrealistic if the stiffness induced by fibre bridging is higher than the stiffness of the matrix.

3.2.3 Sigmoid Relation

In the third approach, which is adopted in this study, it is proposed for hardening to link the crack opening to the cracking strain for $\varepsilon_{\mathrm{cr}} < \varepsilon_{\mathrm{cu}}$ as

$$\delta(\varepsilon_{\mathrm{cr}}) = \delta_{\mathrm{cu}} \frac{1 - \exp\left(-\dfrac{\varepsilon_{\mathrm{cr}}}{\xi}\right)}{1 - \exp\left(-\dfrac{\varepsilon_{\mathrm{cu}}}{\xi}\right)} \tag{3.27}$$

where $\varepsilon_{\mathrm{cu}} = \gamma_{\mathrm{cu}}\delta_{\mathrm{cu}}/s_{\mathrm{m}}$ is the cracking strain at the peak of the bridging stress and s_{m} is the saturated crack spacing. Here, ξ is a parameter, which controls the slope of the relationship between the maximum displacement and the cracking strain at maximum bridging stress. Furthermore, γ_{cu} is a parameter, which originates from the variation of fibres and relates the average crack opening $\bar{\delta}_{\mathrm{cu}}$ to the maximum crack opening δ_{cu} at maximum bridging stress as $\bar{\delta}_{\mathrm{cu}} = \gamma_{\mathrm{cu}}\delta_{\mathrm{cu}}$. For $\varepsilon_{\mathrm{cr}} = \varepsilon_{\mathrm{cu}}$, (3.27) results in $\delta(\varepsilon_{\mathrm{cr}}) = \delta_{\mathrm{cu}}$. The link between γ_{cu} and the variation of fibres is explained in Section 3.3.3. Sigmoid relation gives a better agreement compared with other two relations, which is shown in figure 3.3 and figure 3.4. Therefore, Sigmoid relation is adapted in CDPM2F.

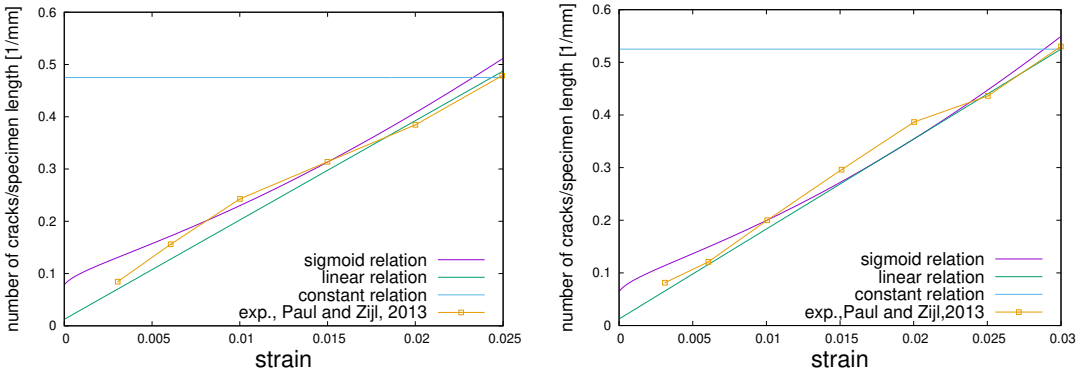

(a) (b)

Figure 3.3: Comparison with experiments for number of cracks per unit length and cracking strain models. (a) coarse sand cement-based strain hardening composite; (b) fine sand cement-based strain hardening composite.

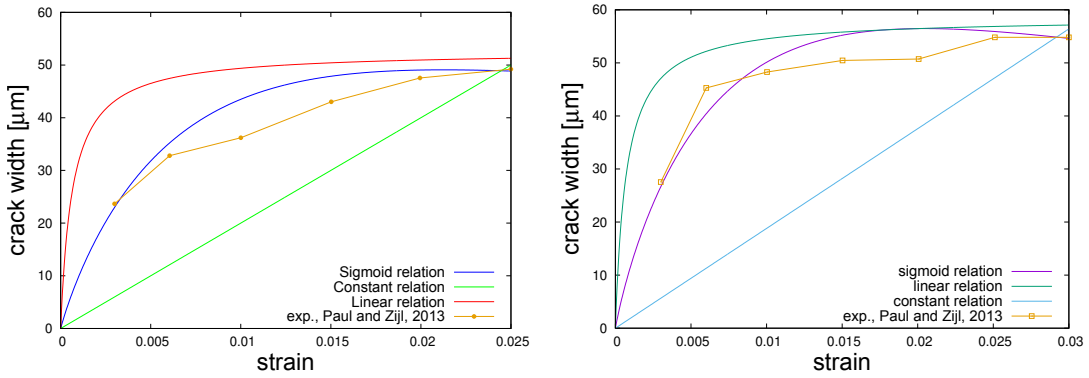

(a) (b)

Figure 3.4: Comparison with experiments for crack width and cracking strain. (a) coarse sand cement-based strain hardening composite; (b) fine sand cement-based strain hardening composite.

3.2.4 Strain softening stage

For the derivation of the link between cracking strain and crack opening during softening, I distinguish again between two crack openings. The first one is the average crack opening δ^{un} of the closing cracks due to unloading and the second

one is the crack opening δ of the widening crack in which the displacements are localised. The bridging stress of the two types of cracks must be the same to satisfy equilibrium. Therefore, the closing crack opening is determined as

$$\delta^{\mathrm{un}} = \frac{\delta_{\mathrm{cu}}^{\mathrm{un}}}{\sigma_{\mathrm{cu}}}\sigma_{\mathrm{f}} = \frac{\delta_{\mathrm{cu}}^{\mathrm{un}}}{\sigma_{\mathrm{cu}}}\sigma_0 \left(1 + \frac{\beta\delta}{d_{\mathrm{f}}}\right)\left(1 - 2\delta/L_{\mathrm{f}}\right)^2 \tag{3.28}$$

where σ_{f} is the bridging stress determined from the crack opening δ of the crack in which the displacements localise according to (3.17). The cracking strain is then the sum of the crack openings divided by the element length h_{e}, which results in

$$\varepsilon_{\mathrm{cr}} = \left(\delta + \left(h_{\mathrm{e}}/s_{\mathrm{m}} - 1\right)\delta_{\mathrm{un}}\right)/h_{\mathrm{e}} \tag{3.29}$$

Setting δ^{un} in (3.28) into (3.29) results in

$$\varepsilon_{\mathrm{cr}} = \frac{1}{h_{\mathrm{e}}}\left(\delta + \left(h_{\mathrm{e}}/s_{\mathrm{m}} - 1\right)\frac{\delta_{\mathrm{cu}}^{\mathrm{un}}}{\sigma_{\mathrm{cu}}}\sigma_0 \left(1 + \frac{\beta\delta}{d_{\mathrm{f}}}\right)\left(1 - 2\delta/L_{\mathrm{f}}\right)^2\right) \tag{3.30}$$

From this function, δ is determined iteratively. To avoid local snapback, i.e. snapback at the constitutive level, $\varepsilon_{\mathrm{cr}}$ must increase with increasing δ, which provides an upper limit for the element size h_{e}, shown in Figure 3.5. This upper limit is determined by setting the second derivative of (3.30) with respect to δ equal to zero and solve forthe critical displacement at which the slope of the softening curve is the steepest. This displacement is then set into the first derivative of (3.30) with respect to δ, which has to be greater than zero. This provides then an inequality for h_{e}, which needs to be satisifed to avoid local snapback. The first derivative of (3.30) with respect to δ is

$$\frac{\mathrm{d}\varepsilon_{\mathrm{cr}}}{\mathrm{d}\delta} = \frac{1}{h_{\mathrm{e}}}\left\{1 + \frac{9c\left(c-2\right)\left(2\delta/L_{\mathrm{f}} - 1\right)\left(\gamma_{\mathrm{cu}}h_{\mathrm{e}}/s_{\mathrm{m}} - 1\right)\left[c\left(2\delta/L_{\mathrm{f}} - 1\right) + 2\left(2c\delta/L_{\mathrm{f}} + 1\right)\right]}{4\left(c+1\right)^3}\right\} \tag{3.31}$$

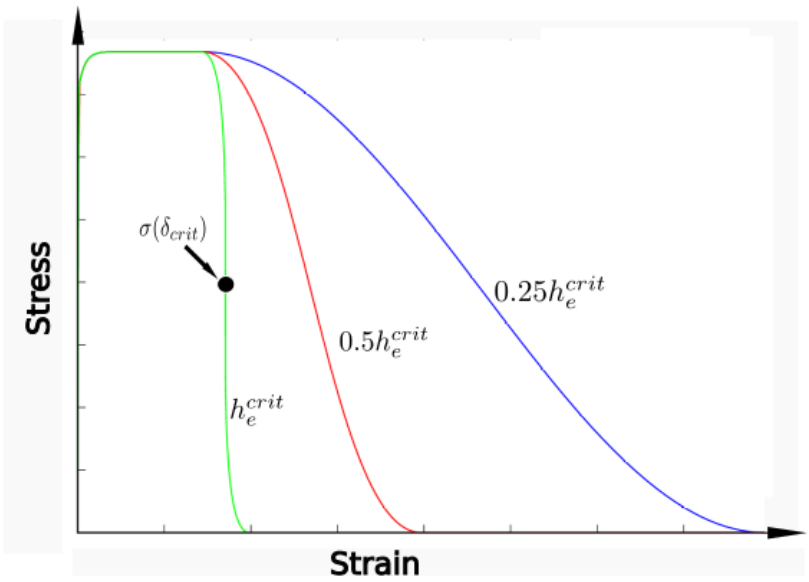

Figure 3.5: Schematic of tensile stress versus strain of single element for different mesh size.

and the second derivative is

$$\frac{\mathrm{d}^2\varepsilon_{\mathrm{cr}}}{\mathrm{d}\delta^2} = \frac{9c\left(\gamma_{\mathrm{cu}}h_{\mathrm{e}} - s_{\mathrm{m}}\right)(c-2)\left(L_{\mathrm{f}} - 2L_{\mathrm{f}}c + 6c\delta\right)}{L_{\mathrm{f}}^2 h_{\mathrm{e}} s_{\mathrm{m}}\left(c+1\right)^3} \tag{3.32}$$

These derivatives are rather complicated, but the critical displacement at the steepest softening and the limit on the element length are of compact form. By setting (3.32) equal to zero and solving for δ, the critical displacement at which the softening is the steepest is determined as $\delta = \delta_{\mathrm{crit}} = L_{\mathrm{f}}(2c-1)/(6c)$. Inserting $\delta = \delta_{\mathrm{crit}}$ into (3.31), setting (3.31) equal to zero and solving it for the element length h_{e} gives

$$h_{\mathrm{e}} = h_{\mathrm{e}}^{\mathrm{crit}} = (7c-2)s_{\mathrm{m}}/(\gamma_{\mathrm{cu}}(3c-6)) \tag{3.33}$$

Since this derivation is for $h_{\mathrm{e}} > s_{\mathrm{m}}/\gamma_{\mathrm{cu}}$, the expression in (3.30) is valid for elements in the range $s_{\mathrm{m}}/\gamma_{\mathrm{cu}} < h_{\mathrm{e}} < (7c-2)s_{\mathrm{m}}/(\gamma_{\mathrm{cu}}(3c-6))$.

Let us now consider the case that $h_\mathrm{e} < s_\mathrm{m}/\gamma_\mathrm{cu}$. This case arises if a fine mesh is used in the numerical analysis. This means that there is no displacement in the element which will unload and the displacement at peak in the element is less than the crack opening. A reduction factor γ_0, which links the crack opening to the displacement at peak, is determined as

$$\gamma_\mathrm{r0} = \frac{\gamma_\mathrm{cu}}{s_\mathrm{m}} h_\mathrm{e} \tag{3.34}$$

Thus, the reduction factor results in $\gamma_\mathrm{r0} = \gamma h_\mathrm{e}/s_\mathrm{m}$ at peak. Since for the crack band model, the displacements are localised in one row/band of elements, the reduction factor needs to increase so that at the end $\gamma_\mathrm{r} = 1$ and the cracking strain is defined at zero fibre stress as $\varepsilon_\mathrm{cr} = L_\mathrm{f}/2/h_\mathrm{e}$. I choose here a linear transition of the reduction factor so that $\gamma_\mathrm{r} = \gamma_\mathrm{r0} + (1-\gamma_\mathrm{r0})(\delta - \delta_\mathrm{cu})/(L_\mathrm{f}/2 - \delta_\mathrm{cu})$. The cracking strain results in

$$\varepsilon_\mathrm{cr} = \frac{\gamma_\mathrm{r}\delta}{h_\mathrm{e}} = \frac{\gamma_\mathrm{r0}\delta}{h_\mathrm{e}} + \frac{(1-\gamma_\mathrm{r0})(\delta^2 - \delta_\mathrm{cu}\delta)}{h_\mathrm{e}\,(L_\mathrm{f}/2 - \delta_\mathrm{cu})} \tag{3.35}$$

For $\delta = \delta_\mathrm{cu}$, we obtain $\varepsilon_\mathrm{cr} = \gamma_\mathrm{r0}\delta_\mathrm{cu}/h_\mathrm{e}$. For $\delta = L_\mathrm{f}/2$, we have $\varepsilon_\mathrm{cr} = L_\mathrm{f}/(2h_\mathrm{e})$. From this equation, the crack opening is determined as

$$\delta = \frac{L_\mathrm{f}\gamma_\mathrm{r0} - 2\delta_\mathrm{cu} - \sqrt{L_\mathrm{f}^2\gamma_\mathrm{r0}^2 - 4\delta_\mathrm{cu}\,(L_\mathrm{f}\gamma_\mathrm{r0} - \delta_\mathrm{cu}) + 8(1-\gamma_\mathrm{r0})\varepsilon_\mathrm{cr}h_\mathrm{e}\,(L_\mathrm{f} - 2\delta_\mathrm{cu})}}{4(\gamma_\mathrm{r0} - 1)} \tag{3.36}$$

With this δ, the fibre stress can be calculated using (3.17). With the softening law derived, all parts of the bridging stress cracking strain law are complete. The fibre stress is now defined as a function of the cracking strain by using (3.27) and (3.30).

3.3 Concrete damage plasticity model CDPM2F for ECC

3.3.1 Bridging stress cracking strain law

To summarise, I developed a link of the crack opening δ to the cracking strain $\varepsilon_{\mathrm{cr}}$ for the fibre part which is split into a hardening and softening part. For hardening, we have (3.27). For softening, we need to consider multiple cases. For $s_{\mathrm{m}}/\gamma_{\mathrm{cu}} < h_{\mathrm{e}}$, I determine the crack opening iteratively from (3.30). For $s_{\mathrm{m}}/\gamma_{\mathrm{cu}} > h_{\mathrm{e}}$, the explicit expression in (3.36) is used. The softening part of the model provided by (3.30) and (3.36) is only valid for $h_{\mathrm{e}} < (7c-2)s_{\mathrm{m}}/(\gamma_{\mathrm{cu}}(3c-6))$. Furthermore, the entire derivation is for strain hardening fibre arrangements with $c > 2 + 6\lambda$. $\tilde{\delta}_{\mathrm{hard}}(\varepsilon_{cr})$ is from 3.27 based on Sigmoid relation proposed and $\tilde{\delta}_{\mathrm{soft}}(\varepsilon_{cr})$ is from 3.36. Then the briging stress cracking strain law is:

$$\sigma_{\mathrm{f}}(\varepsilon_{\mathrm{cr}}) = \begin{cases} \dfrac{2\sigma_0}{k}\left[1 - \dfrac{1}{k}\cosh^{-1}\left(1 + \lambda\dfrac{\tilde{\delta}_{\mathrm{hard}}(\varepsilon_{\mathrm{cr}})}{\tilde{\delta}^*}\right)\right]\sqrt{\left(1 + \lambda\dfrac{\tilde{\delta}_{\mathrm{hard}}(\varepsilon_{\mathrm{cr}})}{\tilde{\delta}^*}\right)^2 - 1} + & \text{if } 0 < \varepsilon_{\mathrm{cr}} \le \varepsilon^*_{\mathrm{cr}} \\ \dfrac{2\lambda\tilde{\delta}_{\mathrm{hard}}(\varepsilon_{\mathrm{cr}})}{k^2\tilde{\delta}^*} + \left[\left(1 + c\tilde{\delta}^*\right)\left(1 - \tilde{\delta}^*\right)^2 - 2\lambda/k^2\right]\tilde{\delta}_{\mathrm{hard}}(\varepsilon_{\mathrm{cr}})/\tilde{\delta}^* & \\ \sigma_0\left(1 + c\tilde{\delta}_{\mathrm{hard}}(\varepsilon_{\mathrm{cr}})\right)\left(1 - \tilde{\delta}_{\mathrm{hard}}(\varepsilon_{\mathrm{cr}})\right)^2 & \text{if } \varepsilon^*_{\mathrm{cr}} < \varepsilon_{\mathrm{cr}} \le \varepsilon_{cu} \\ \sigma_0\left(1 + c\tilde{\delta}_{\mathrm{soft}}(\varepsilon_{\mathrm{cr}})\right)\left(1 - \tilde{\delta}_{\mathrm{soft}}(\varepsilon_{\mathrm{cr}})\right)^2 & \text{if } \varepsilon_{\mathrm{cu}} < \varepsilon_{\mathrm{cr}} \le \varepsilon_{\mathrm{ult}} \\ 0 & \text{if } \varepsilon_{\mathrm{cr}} \ge \varepsilon_{\mathrm{ult}} \end{cases} \tag{3.37}$$

where in equation 3.37:

$$\varepsilon_{\mathrm{ult}} = \frac{L_{\mathrm{f}}}{2h_{\mathrm{e}}} \tag{3.38}$$

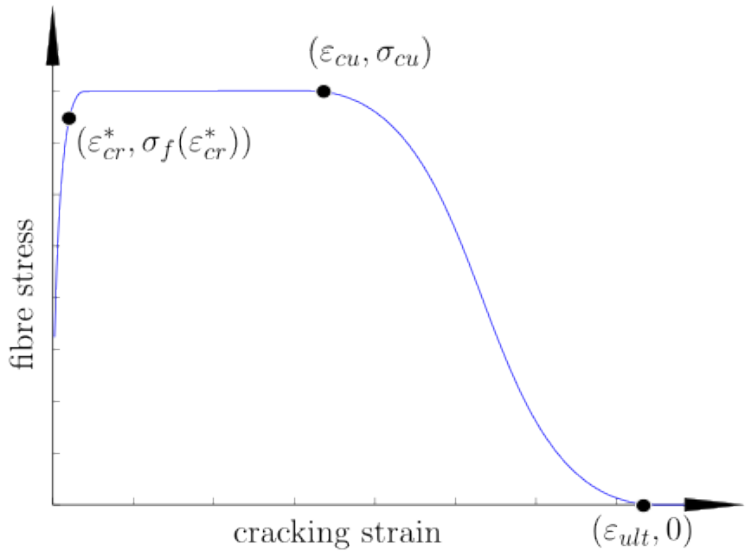

Figure 3.6: Schematic of fibre stress versus cracking strain relation

$\varepsilon^*_{\mathrm{cr}}$ satisfies the condition:

$$\tilde{\delta}^* = \tilde{\delta}_{\mathrm{hard}}(\varepsilon^*_{\mathrm{cr}}) \tag{3.39}$$

The general fibre stress versus cracking strain curve for different stage is shown in Figure 3.6.

3.3.2 Extension of CDPM2

The present section describes CDPM2F, which is an extension of the concrete damage-plasticity model CDPM2 to ECC proposed in this study. The original CDPM2 is a 3D concrete damage-plasticity model presented in Grassl et al. (2013), which has been shown to produce good results for a wide range of concrete fracture tests (Bažant et al., 2022; Bažant and Nguyen, 2023). These tests include tensile, shear and compressive fracture processes of unconfined and confined concrete. Here, CDPM2 is extended to CDPM2F by combining it with a fibre bridging

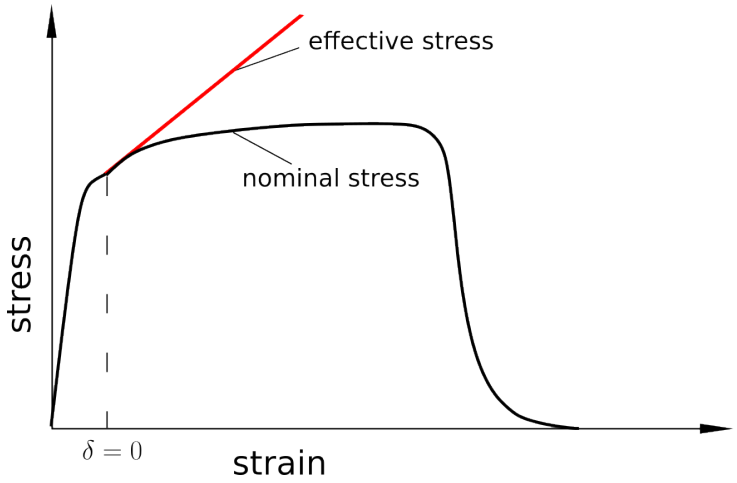

Figure 3.7: Stress-strain law incorporate with damage plastic approach

cracking strain law mentioned previously.

CDPM2 is based on the concept of combining scalar damage with tensorial plasticity. The nominal stress $\boldsymbol{\sigma}$ is

$$\boldsymbol{\sigma} = (1 - \omega_{\mathrm{t}})\, \bar{\boldsymbol{\sigma}}_{\mathrm{t}} + (1 - \omega_{\mathrm{c}})\, \bar{\boldsymbol{\sigma}}_{\mathrm{c}} \tag{3.40}$$

Here, ω_{t} and ω_{c} are the tensile and compressive damage variables, respectively. Furthermore, $\bar{\boldsymbol{\sigma}}_{\mathrm{t}}$ and $\bar{\boldsymbol{\sigma}}_{\mathrm{c}}$ are the positive and negative parts of the effective stress $\bar{\boldsymbol{\sigma}}$, respectively. The two parts of the effective stress are determined from the principal components of the effective stress $\bar{\boldsymbol{\sigma}} = \mathbf{D}_{\mathrm{e}}\,(\boldsymbol{\varepsilon} - \boldsymbol{\varepsilon}_{\mathrm{p}})$. Here, $\mathbf{D}_{\mathrm{e}}$ is the elastic stiffness, $\boldsymbol{\varepsilon}$ is the strain and $\boldsymbol{\varepsilon}_{\mathrm{p}}$ is the plastic strain. For a description of the equations of CDPM2, it is referred to Grassl et al. (2013), which contains all required details. Here I focus on the extension of CDPM2 to ECC, for which I only adjust the tensile damage part of the model which is derived based on a 1D tensile response of the material of the form,

$$\sigma = (1 - \omega_{\mathrm{t}})\bar{\sigma} = (1 - \omega_{\mathrm{t}})\, E\,(\varepsilon - \varepsilon_{\mathrm{p}}) = E\,(\varepsilon - \varepsilon_{\mathrm{cr}}) \tag{3.41}$$

because in 1D tension $\bar{\sigma}_{\mathrm{t}} = \bar{\sigma} = E\left(\varepsilon - \varepsilon_{\mathrm{p}}\right)$. In (3.41), the inelastic strain component $\varepsilon_{\mathrm{cr}}$ is defined as

$$\varepsilon_{\mathrm{cr}} = \varepsilon_{\mathrm{p}} + \omega_{\mathrm{t}}\left(\varepsilon - \varepsilon_{\mathrm{p}}\right) \tag{3.42}$$

where ε_{p} is the irreversible and $\omega_t\left(\varepsilon - \varepsilon_p\right)$ is the reversible inelastic strain part. The damage variable ω_{t} is in the range from 0 (undamaged) to 1 (fully damaged). The composition of the two parts of the inelastic strain are controlled by the hardening parameter H_{p} of the plasticity part of CDPM2 (Grassl et al., 2013), which determines the effective stress of the undamaged material. The damage variable ω_{t} is then used to reduce the effective stress to obtain the nominal stress. For $H_{\mathrm{p}} = 0$, the majority of the cracking strain is composed of the irreversible part, because the plasticity part does not exhibit any hardening and damage is only used to reduce the stress from the level of the tensile strength during the softening response. For $H_p \to 1$, the plastic strain approaches zero and the cracking strain is mainly reversible.

For ECC, the 1D stress-strain law in (3.41) is the sum of stresses transmitted in the matrix and by the fibres as

$$\sigma = E\left(\varepsilon - \varepsilon_{\mathrm{cr}}\right) = \sigma_{\mathrm{m}}(\delta) + \sigma_{\mathrm{f}}(\delta) \tag{3.43}$$

where σ_{m} is the matrix and σ_{f} is the fibre stress in direct tension and δ is the crack opening. How the stress-strain relation is incorporated in CDPM2 is shown in Figure 3.7. For the fibre stress, I propose a new model described in Section 3.1.2. For the concrete stress, I use an exponential stress crack opening curve of the form

$$\sigma_{\mathrm{m}}\left(\delta\right) = f_{\mathrm{t}} \exp\left(-\frac{\delta}{\delta_{\mathrm{f}}}\right) \tag{3.44}$$

Here, f_{t} is the tensile strength of the matrix and δ_{f} is the crack open threshold

which controls the softening slope. Since the damage-plasticity model is a function of the cracking strain $\varepsilon_{\mathrm{cr}}$ and the matrix and fibre models are functions of the crack opening δ, a link between crack opening and cracking strain is required which has been introduced in Section 3.2. With this link, both cracking strain in (3.42) and crack opening are functions of the damage variable ω_{t}, which is determined iteratively from (3.43).

3.3.3 Calibration with fibre dispersion

The calibration of CDPM2F, which is an extension of CDPM2 to strain hardening materials is split into two parts. First, the calibration of CDPM2 is addressed. Then, the calibration of the fibre model is discussed.

The input parameters for the matrix are those of the CDPM2 model. Many of the input parameters of CDPM2 have default values, which are used in this study and are described in Grassl et al. (2013). I assume in this study that these parameters apply also to the matrix of ECC. Five parameters of CDPM2 do not have default values and are required to be determined. These parameters are the Young's modulus E_{m}, the tensile strength f_{t}, the compressive strength f_{c} and the crack opening threshold in tension δ_{f}, which for the present exponential law in (3.44) is calculated from the fracture energy G_{F} as $\delta_{\mathrm{f}} = G_{\mathrm{F}}/f_{\mathrm{t}}$. Furthermore, Poisson's ratio ν of the matrix is required. In addition to these five parameters, there is the strain threshold ε_{f} which controls the softening response in compression. Furthermore, the hardening modulus was set for all analyses to $H_{\mathrm{p}} = 0.05$ to ensure that for the majority of the stress-strain response the effective stress is greater than the fibre stress.

For the fibre model, nine input parameters are required for the fibre stress-strain

relation. Some of these parameters can be directly obtained from the specifications of the fibre manufactures and the design of the material. These parameters are Young's modulus of fibres E_{f}, length of fibre L_{f}, diameter of fibre d_{f}. The next group of input parameters are related to the fibre stress versus crack opening law. These parameters are the volume fraction V_{f}, shear strength of interface τ_0, hardening parameter β, the snubbing factor f. Furthermore, there are the parameters ξ and γ_{cu}, which control the relation of crack opening and cracking strain. Here, V_{f} and γ_{cu} are two parameters which depend on the spatial variation of the distribution of fibres and are calculated indirectly using the uniform volume fraction V_{f0} and the fibre distribution coefficient α, which represents the degree of variation of the spatial fibre distribution (Li and Li, 2013b). The parameter α in (Li and Li, 2013b) is determined by the number of fibres crossing the cross-section at weakest crack and the average number of fibres of all cracks. I link the fibre dispersion coefficient to the variation of volume fraction of the weakest crack to average volume fraction. This is because in (Lin and Li, 1997) equation 7, V_{f} is used to represent area ratio of bridging fibres, which is also dependent on number of fibres crossing crack surface for certain diameter of fibres. I assume that we can link the fibre volume fraction V_{f} at a cracked section to the dispersion as

$$\alpha = \exp \frac{V_{\mathrm{f}} - V_{\mathrm{f0}}}{V_{\mathrm{f0}}} \tag{3.45}$$

so that

$$V_{\mathrm{f}} = (1 + \ln \alpha)\, V_{\mathrm{f0}} \tag{3.46}$$

There is a lower limit for α so that strain hardening is guaranteed. The condition for strain hardening is

$$\sigma_{\mathrm{cu}} = \sigma_0 \bar{\sigma}_{\mathrm{cu}} \geq f_{\mathrm{t}} \tag{3.47}$$

Using the expression for $\bar{\sigma}_{\mathrm{cu}}$ in (3.20) and σ_0 in (3.7) we obtain

$$\frac{1}{2} g \tau_0 V_{\mathrm{f}} \left(1+\eta\right) \frac{L_{\mathrm{f}}}{d_{\mathrm{f}}} \frac{4\left(c+1\right)^3}{27c^2} \geq f_{\mathrm{t}} \tag{3.48}$$

For the minimum volume $V_{\mathrm{f}} = V_{\mathrm{f,min}}$, a bridging stress equal to f_{t} is required. This results in the equation

$$\frac{1}{2} g \tau_0 V_{\mathrm{f,min}} \left(1+\eta\right) \frac{L_{\mathrm{f}}}{d_{\mathrm{f}}} \frac{4\left(c+1\right)^3}{27c^2} = f_{\mathrm{t}} \tag{3.49}$$

Here, η is a function of $V_{\mathrm{f,min}}$ according to (3.3). Also, the factor $L_{\mathrm{f}}/d_{\mathrm{f}}$ is linked to c. Using these two expressions, we obtain

$$\left(E_{\mathrm{f}} - E_{\mathrm{m}}\right) V_{\mathrm{f,min}}^2 + \left(E_{\mathrm{m}} + E_{\mathrm{m}} Z\right) V_{\mathrm{f,min}} - E_{\mathrm{m}} Z = 0 \tag{3.50}$$

where

$$Z = \frac{27 f_{\mathrm{t}} \beta}{4 g \tau_0} \frac{c}{\left(c+1\right)^3} \tag{3.51}$$

Now, from (3.50), we obtain

$$V_{\mathrm{f,min}} = \frac{-\left(E_{\mathrm{m}} + E_{\mathrm{m}} Z\right) + \sqrt{\left(E_{\mathrm{m}} + E_{\mathrm{m}} Z\right)^2 + 4\left(E_{\mathrm{f}} - E_{\mathrm{m}}\right) E_{\mathrm{m}} Z}}{2\left(E_{\mathrm{f}} - E_{\mathrm{m}}\right)} \tag{3.52}$$

I set now $V_{\mathrm{f,min}}$ into the expression for α in (3.45) which gives

$$\alpha_{\mathrm{min}} = \exp \frac{V_{\mathrm{f,min}} - V_{\mathrm{f0}}}{V_{\mathrm{f0}}} \tag{3.53}$$

Here, α_{min} is the lower limit of α, so that the region with a critically low fibre distribution still exhibits strain hardening.

Parameter γ_{cu} depends also on α. I assume that γ_{cu} is a linear function of α as

$$\gamma_{\mathrm{cu}} = \frac{(1-\alpha)\,\varepsilon_0 s_{\mathrm{m}}}{\delta_{\mathrm{cu}}\,(1-\alpha_{\mathrm{min}})} + \frac{\alpha - \alpha_{\mathrm{min}}}{1-\alpha_{\mathrm{min}}} \tag{3.54}$$

which is motivated by experimental results in Li and Li (2013b); Zhou et al. (2012b). Let us explore (3.54). For $\alpha = \alpha_{\mathrm{min}}$, we have $\gamma_{\mathrm{cu}} = \varepsilon_0 s_{\mathrm{m}}/\delta_{\mathrm{cu}}$. Thus, $\varepsilon_{\mathrm{cu}} = \gamma_{\mathrm{cu}}\delta_{\mathrm{cu}}/s_{\mathrm{m}} = \varepsilon_0$. For the other limit, let us consider the case of a fibre reinforced specimen at ultimate stress σ_{cu} for which all cracks exhibit the same crack opening and are equally spaced, which corresponds to $\alpha = 1$, i.e. fibres are uniformly distributed within the volume. For this idealised assumption, $\gamma_{\mathrm{cu}} = 1$ and, therefore, $\varepsilon_{\mathrm{cu}} = \delta_{\mathrm{cu}}/s_{\mathrm{m}}$. This concludes the calibration of the model.

CDPM2F is implemented in the open source finite element program OOFEM (Patzák, 2012). The implementation of the procedure for the computation of the effective stress and the compressive damage variable is the same as in CDPM2. For determining the tensile damage variable, three steps are carried out. First, the cracking strain is converted into crack opening. Then, the fibre and matrix stresses are computed as function of the crack opening. Finally, the damage variable is determined iteratively from the balance of nominal stress and sum of fibre and concrete stress.

Chapter 4

Material response of CDPM2F

In this chapter, the constitutive model is used to investigate plain ECC response subjected to tension, shear and compression.

4.1 Determination of material parameters

In this section, the way how material parameters are determined is presented. Parameters are related to fibre, matrix and fibre/matrix properties. For fibres, the parameters are Young's modulus of fibres E_{f}, volume fraction of fibres V_{f0}, length of fibres L_{f}, diameter of fibres d_{f} and snubbing factor f. For the matrix, the parameters are the Young's modulus of matrix E_{m}, tensile strength of matrix f_{t}, compressive strength of matrix f_{c}, Poisson's ratio ν, rack opening threshold δ_{f}. For the fibre/matrix interface, the parameters are the slip hardening coefficient β and the interface bond strength τ_0. Parameters mentioned above should be determined either from experiments or manufacturer. Another parameter is ξ,

which controls the slope of sigmoid relation. The default value for this parameter is $\xi = 10$, which is used for fitting experimental results. The parameter α, has a lower limit $\alpha_{\min}$, which is calculated automatically based on material properties. Normally α is around 0.9 for good mixed ECC, but around 0.7 for poor mixed ECC. The parameter s_{m} needs to be set by users. It represents the saturated crack spacing, which is affecting the manufacturing process. By using artificial flaws in the matrix. Fine saturated crack spacing can be reached. For good mixed ECC, 0.02 m crack spacing is normally used.

4.2 Tensile response for different material parameters

In this section, the tensile response of composite is related to matrix properties, fibre properties and interface properties. As mentioned in section 2.1.2.2, both tensile strength capacity and tensile strain capacity of ECC have positive correlation with fibre reinforced index ($\frac{V_{\mathrm{f0}} L_{\mathrm{f}}}{d_{\mathrm{f}}}$).

A test of a single linear tetrahedral element subject to tensile loading for different material/interface properties is carried out. The setup of single tetrahedral element test is shown in Figure 4.1. Node 1 is fully fixed; Node 2 fixed at Y and Z direction; Node 4 is fixed at X and Y direction; Node 3 is fixed at Z direction and the nodal force is applied at Y direction. Controlled variables to investigate are volume fraction of fibres V_{f0}, length of fibres L_{f}, diameter of fibres d_{f}, and slip hardening coefficient β. The default input of the controlled parameters are $V_{\mathrm{f0}} = 0.02$, $L_{\mathrm{f}} = 12$ mm, $d_{\mathrm{f}} = 0.04$ mm, $\beta = 0.02$. The model input parameters for the matrix are Young's modulus $E_{\mathrm{m}} = 20$ GPa, Poisson's ratio $\nu = 0.2$, tensile strength

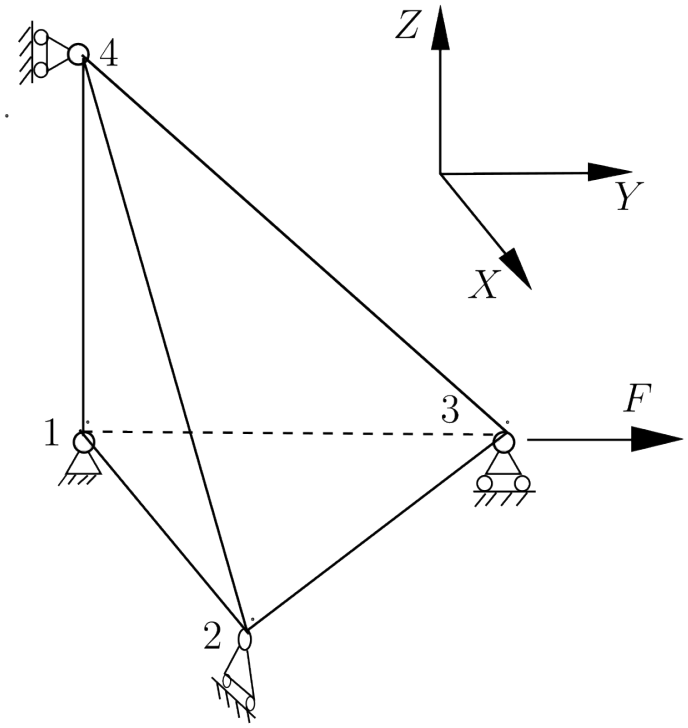

Figure 4.1: Setup of single tetrahedral element tensile test

$f_{\mathrm{t}} = 2.0$ MPa, compressive strength $f_{\mathrm{c}} = 20.$ MPa and crack opening threshold $\delta_{\mathrm{f}} = 0.02$ mm. The fibre properties are Young's modulus $E_{\mathrm{f}} = 22$ GPa, $f = 0.8$, $\tau_0 = 0.8$ MPa, $s_{\mathrm{m}} = 20$ mm, $\alpha = 0.8$, length $L_{\mathrm{f}} = 11/12$ mm, fibre diameter $d_{\mathrm{f}} = 0.014$ mm, $\beta = 0.015$,$V_{\mathrm{f0}} = 0.015$.

Figure 4.2 a to c shows the composite response for different L_{f} and V_{f0}, which shows the correct response as described in section 2.1.2.2. Each of L_{f}, V_{f0} and d_{f} is able to affect both tensile strength capacity and tensile strain capacity. Figure 4.3 shows peak stress and strain capacity for different $\frac{V_{\mathrm{f0}}L_{\mathrm{f}}}{d_{\mathrm{f}}}$ for Figure 4.2 a to c, which agree with the response as described in section 2.1.2.2.Long and thin fibres are preferred for manufacturing ECC with strong strain hardening property. Figure 4.2 d) shows composite tensile response for different slip hardening coefficient. The interface slip hardening property is another factor which can generate strong strain hardening.

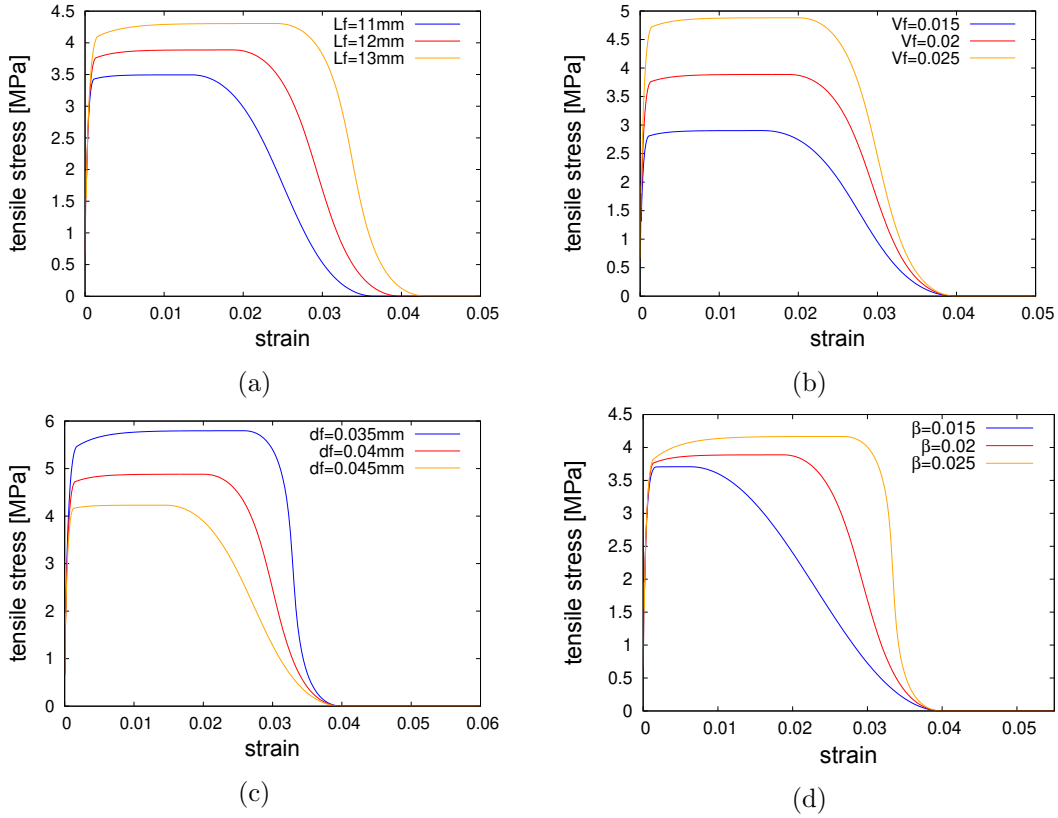

Figure 4.2: Material response for different material properties: a) length of fibres (L_{f}): 11 mm, 12 mm and 13 mm; b) volume fraction of fibres (V_{f0}): 0.015, 0.02, 0.025; c) diameter of fibres (d_{f}): 0.035 mm, 0.04 mm, 0.045 mm. d) slip hardening coefficient (β): 0.015, 0.02, 0.025

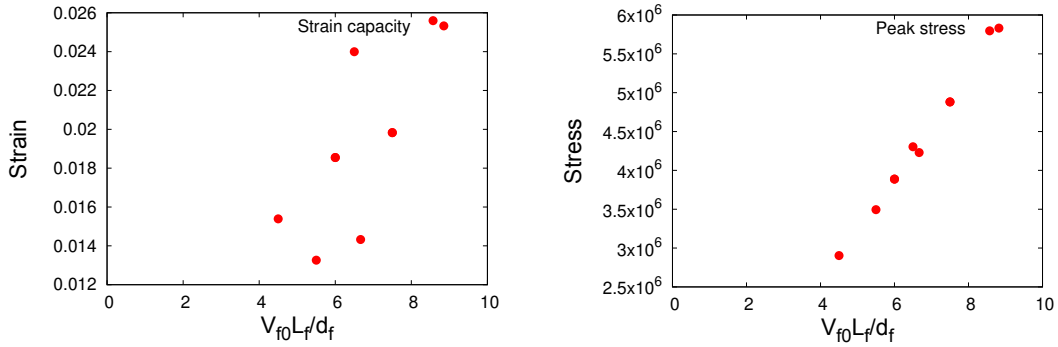

Figure 4.3: a) Strain capacity and b) peak stress predicted by model for different $\frac{V_{\mathrm{f0}} L_{\mathrm{f}}}{d_{\mathrm{f}}}$

4.3 Tension

The next example is a tensile test of an ECC specimen reported in Kanda and Li (2006a). This is the first example which is compared with experiments. The geometry with loading setup and the medium finite element mesh with an element size of 2 cm is shown in Figure 4.4a and b, respectively. The out-of-plane thickness is 12.7 mm. The three-dimensional finite element mesh consists of tetrahedral elements and was generated with the mesh generator T3D (Rypl, 1998). A prescribed displacement is applied at the right surface of specimen. Displacement in the horizontal direction is restrained at left side surface of specimen.

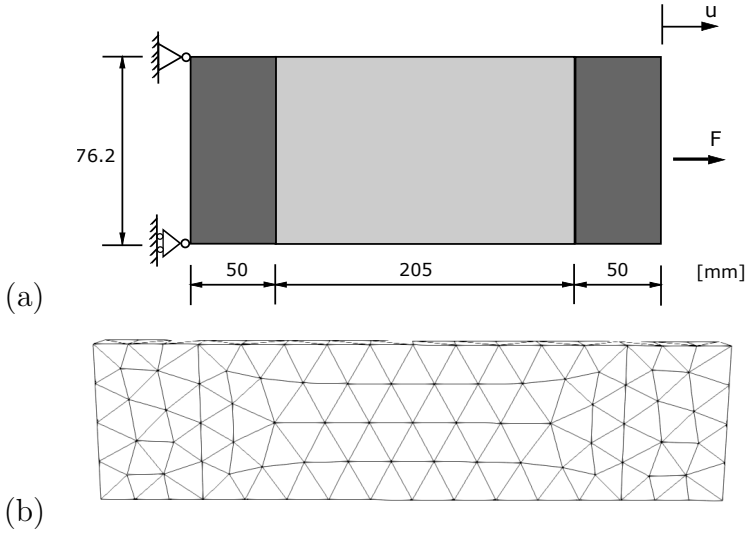

Figure 4.4: a) Tensile test setup used in the model based on the experiments reported in Kanda and Li (2006a); b) Medium three-dimensional tetrahedral finite element mesh with element size 2 cm. The out-of-plane thickness is 12.7 mm.

From the experiments in Kanda and Li (2006a), two sets were modelled which differ mainly in fibre properties. For set 1 with short and thin fibres, the model input parameters for the matrix are Young's modulus $E_{\mathrm{m}} = 15.9$ GPa, Poisson's

ratio $\nu = 0.2$, tensile strength $f_{\mathrm{t}} = 1.12$ MPa, compressive strength $f_{\mathrm{c}} = 15.5$ MPa and crack opening threshold $\delta_{\mathrm{f}} = 0.01$ mm. Here, E_{m} and f_{c} were chosen from Kanda and Li (2006a). Tensile strength f_{t} was chosen to be smaller than in the experiments to avoid initial softening in the constitutive response. The stress is composed of fibre stress and matrix stress. The matrix stress reaches its maximum at a much smaller strain than the fibre stress. Therefore, it could be that after the matrix stress reaches its maximum the decrease of the matrix stress (softening) is greater than the increase of the fibre stress (hardening). This would then lead to a decrease of the overall stress even if the final fibre bridging stress is greater than the sum of fibre and matrix stress when the matrix stress reaches its maximum. The parameters ν and δ_{f} were given typical values for mortar. The fibre properties are Young's modulus $E_{\mathrm{f}} = 60$ GPa, length $L_{\mathrm{f}} = 6$ mm, fibre diameter $d_{\mathrm{f}} = 0.014$ mm, $f = 0.5$, $\beta = 0.015$, $\tau_0 = 1.8$ MPa, $s_{\mathrm{m}} = 12$ mm, $\xi = 10$, $\alpha = 0.53$ and $V_{\mathrm{f0}} = 0.015$. The last two parameters result in $\gamma_{\mathrm{cu}} = 0.2$ and $V_{\mathrm{f}} = 0.0055$. These fibre properties result in $c = \beta L_{\mathrm{f}} / (2d_{\mathrm{f}}) = 3.2$. Here, E_{f}, L_{f}, d_{f} and V_{f0} are chosen from Kanda and Li (2006a). The other parameters were given reasonable values for ECC so that the response agreed with the experimental results.

For set 2 with long and thick fibres, the model input parameters for the matrix are Young's modulus $E_{\mathrm{m}} = 15.9$ GPa, Poisson's ratio $\nu = 0.2$, tensile strength $f_{\mathrm{t}} = 1.12$ MPa, compressive strength $f_{\mathrm{c}} = 15.5$ MPa and crack opening threshold $\delta_{\mathrm{f}} = 0.01$ mm. Again, E_{m}, f_{t} and f_{c} were chosen from Kanda and Li (2006a). The parameters ν and δ_{f} were given typical values for mortar. The fibre properties are Young's modulus $E_{\mathrm{f}} = 60$ GPa, length $L_{\mathrm{f}} = 12$ mm, fibre diameter $d_{\mathrm{f}} = 0.04$ mm, $f = 0.5$, $\beta = 0.015$, $\tau_0 = 1$ MPa, $s_{\mathrm{m}} = 4$ mm, $\xi = 10$, $\alpha = 0.59$ and $V_{\mathrm{f0}} = 0.02$. The last two parameters result in $\gamma_{\mathrm{cu}} = 0.23$ and $V_{\mathrm{f}} = 0.00094$. This gives $c = \beta L_{\mathrm{f}} / (2d_{\mathrm{f}}) = 2.3$. Again, E_{f}, L_{f}, d_{f} and V_{f0} are chosen from Kanda and Li (2006a). The other parameters were given reasonable values for ECC so that the response

agreed with the experimental results. The end areas of the specimen shown in dark grey in Figure 4.4 are modelled as aluminium with Young's modulus of 70 GPa and Poisson's ratio of $\nu = 0.2$. The comparison of FE model and experiments is shown in Figure 4.5 in the form of stress versus strain for the mesh with an element size of 2 cm. Here, stress is the force divided by the cross-sectional area and strain is the end displacement of the specimen divided by the length.

CDPM2F produces for the tensile response of ECC with the two fibre properties results which are in good agreement with the experiments. As expected from the expression of $\tilde{\sigma}_{\mathrm{cu}}$ in (3.20), the set with greater c produces the greater bridging stress.

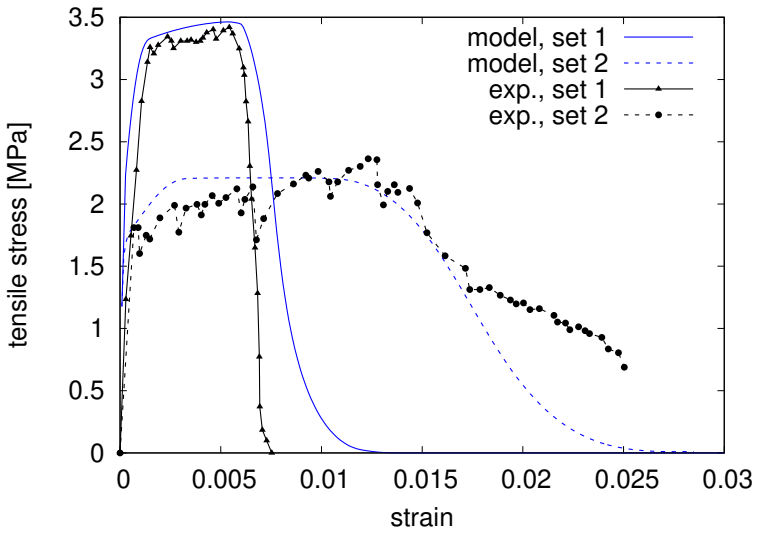

Figure 4.5: Comparison of set 1 and 2 of finite element model with element size 0.02m with experimental results reported in Kanda and Li (2006a).

Next, it is checked that the model does not exhibit pathological mesh-dependence. Coarse, medium and fine meshes with element sizes of 4, 2 and 1 cm, respectively, are used for the ECC with short fibres. The input is the same as for the comparison with the experiments. The results are shown in the form of tensile stress versus

strain in Figure 4.6.

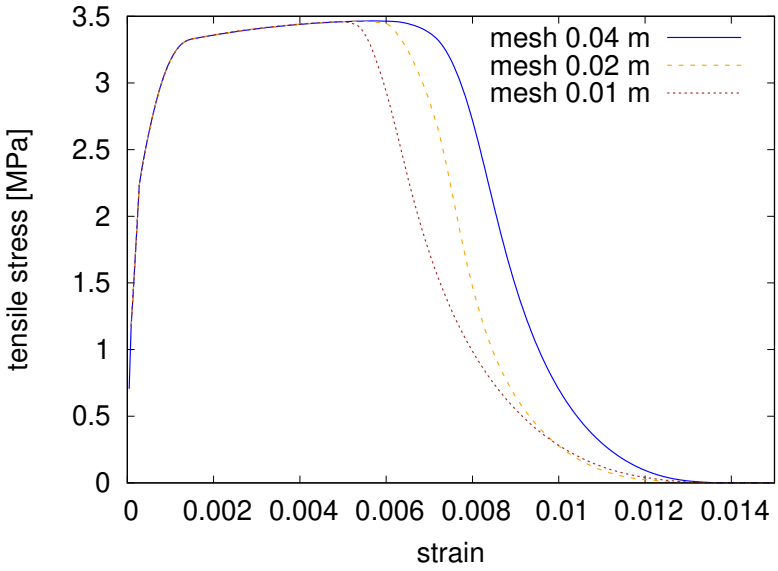

Figure 4.6: Convergence of set 2 model

The first part of the response up to the onset of softening is mesh independent. For the softening part a difference in the curves is present. However, for all three curves softening starts at the same strain and also reach zero stress at the same strain. The pre- and post-peak responses can be further understood by studying the strain profiles for the three meshes. For the hardening part, the strain contours are shown in Figure 4.7 at an average strain of 0.004 in Figure 4.6.

The strains are more or less uniform in the concrete specimen and independent of the mesh size. Slightly higher strains are visible close to the ends of the ECC specimen next to the aluminium plates due to the higher stiffness of the plates which constraints the ECC material in the lateral direction. The ECC material is strain hardening at this stage of the analysis.

In Figure 4.8, the maximum principal strain contours are shown at an average strain of 0.012 in Figure 4.6. At this softening stage of the analyses, strain is

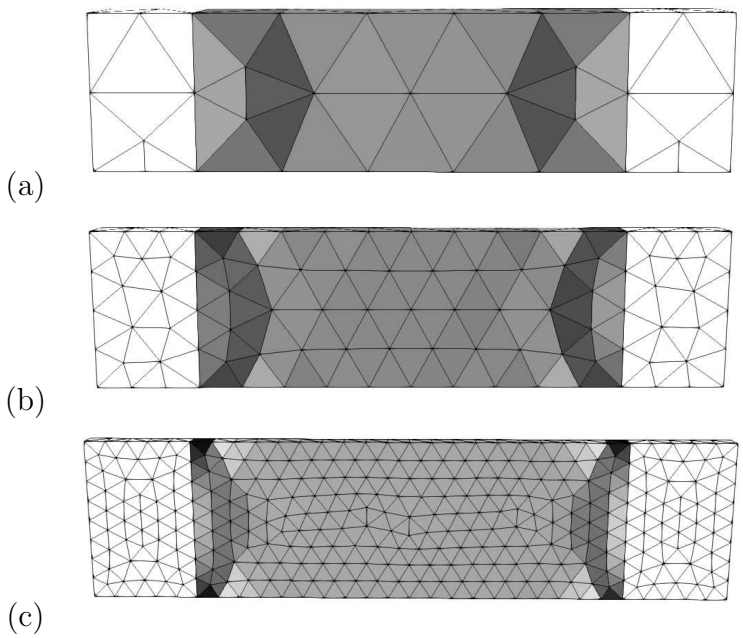

Figure 4.7: Contour plot of the maximum component of the principal strain at an average strain of 0.004 for mesh sizes a) 4 cm, b) 2 cm and c) 1 cm. The upper threshold for the maximum strain was chosen as 0.006.

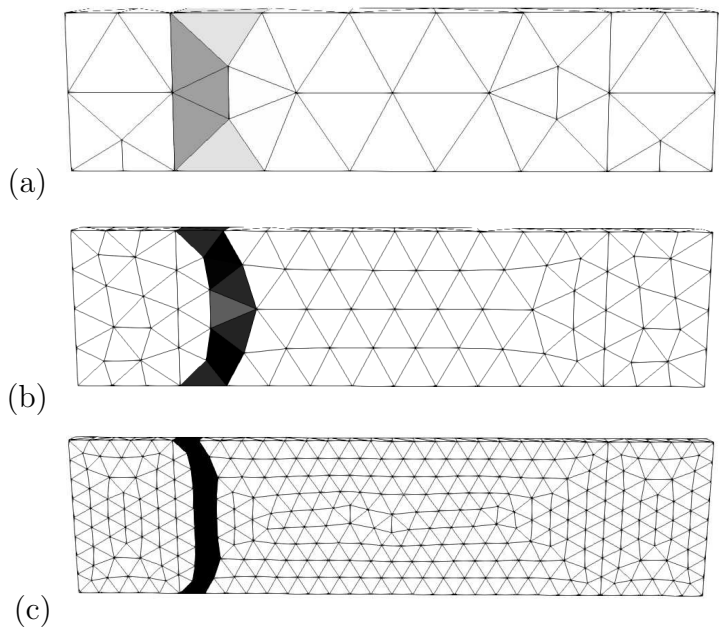

Figure 4.8: Contour plot of the maximum component of the principal strain at an average strain of 0.012 for mesh sizes a) 4 cm, b) 2 cm and c) 1 cm. The upper threshold for the maximum strain was chosen as 0.15.

localised in mesh dependent zones as assumed for the crack band approach. The difference between the curves for the meshes in the softening regime is explained by the link between crack opening and cracking strain defined in (3.36). With the input chosen for the present comparison to the experiments in Kanda and Li (2006a), we have $h_e < s_m/\gamma_{cu}$. Therefore, the reduction factor determined in (3.34) is used in the simulations, which varies linearly during softening.

In the tensile analyses, the hardening modulus was set to $H_p = 0.05$. This value was chosen because it allows for a good representation of the debonding stage of the tensile test as shown in Figure 4.9. Larger values of H_p result in less plasticity, which can be problematic in analyses in which compression plays a role.

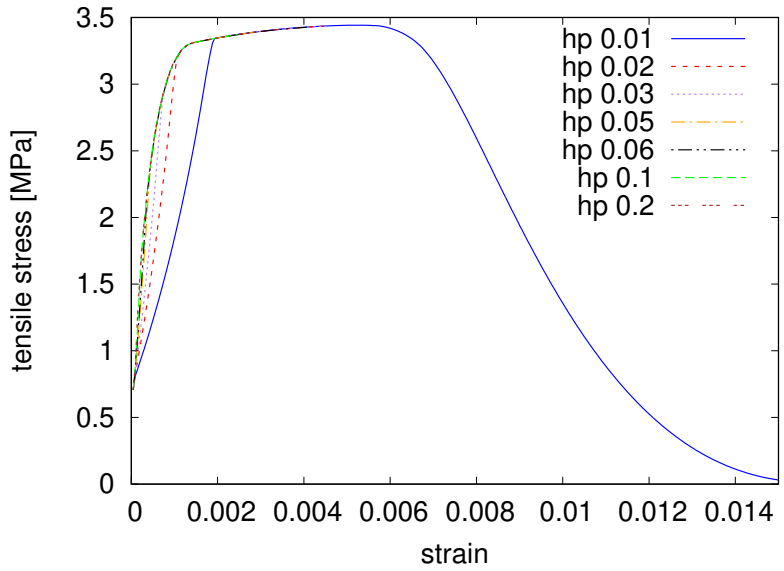

Figure 4.9: Stress strain response for set 1 with H_p values ranging from 0.01 to 0.2.

4.4 Shear

The second example is an ECC panel subjected to shear as reported in Li et al. (1994). The geometry and loading setup is shown in Figure 4.10a. The specimen

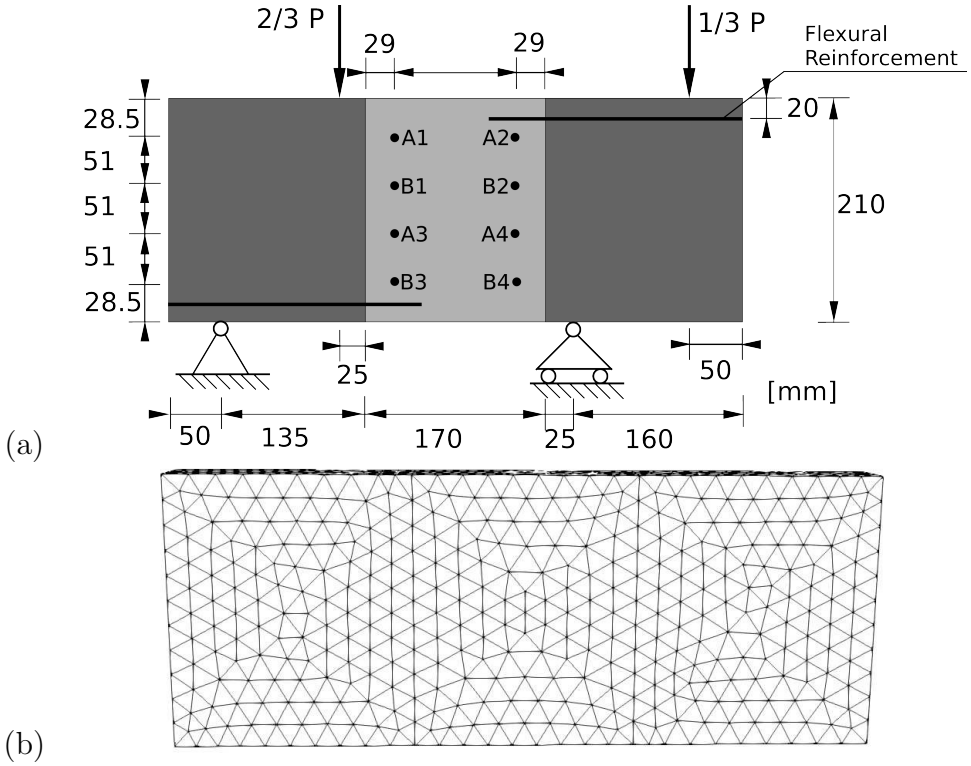

Figure 4.10: a) Geometry and setup of ECC panel subjected to shear based on (Li et al., 1994) and b) three-dimensional tetrahedral finite element mesh with element size of 2 cm.

consists of two regions modelled to be linear elastic (shown as dark grey) and a middle region modelled as ECC material. The out-of-plane thickness of the specimen is 50 mm. Boundary conditions are applied at edge of out-of-plane thickness. A coarse, medium and fine mesh with element sizes of $h_e = 4$, 2 and 1 cm were used. The three-dimensional tetrahedral meshes were generated with T3D

(Rypl, 1998). The mesh with an element size $h_e = 2$ cm is shown in Figure 4.10b.

Many of the material parameters were chosen using the information provided in Li et al. (1994). Some of the model parameters were calibrated to obtain a good agreement with the experimental results. For the ECC specimen, model input parameters for the matrix are Young's modulus $E_m = 20$ GPa, Poisson's ratio $\nu = 0.2$, tensile strength $f_t = 1.4$ MPa, compressive strength $f_c = 53$ MPa and crack opening threshold $\delta_f = 0.015$ mm. Furthermore, $\varepsilon_f = 0.000085$, which is close to the default value of 0.0001. Here, E_m and f_c were chosen from Li et al. (1994). The tensile strength was reduced (experimental value is 2.2 MPa) to avoid initial softening in the initial part of the stress-strain curve. The parameters ν and δ_f were given typical values for mortar. The fibre properties are Young's modulus $E_f = 48$ GPa, length $L_f = 12.7$ mm, fibre diameter $d_f = 0.04$ mm, $f = 0.8$, $\beta = 0.03$, $\tau_0 = 0.63$ MPa, $s_m = 18$ mm, $\xi = 10.$, $\alpha = 0.9$ and $V_{f0} = 0.02$. The last two parameters result in $\gamma_{cu} = 0.808$ and $V_f = 0.0179$. The parameters result in $c = \beta L_f / (2d_f) = 5.01$. Here, E_f, L_f, d_f and V_{f0} are chosen from Li et al. (1994). The other parameters were given reasonable values for ECC so that the constitutive response agreed with the experimental results of ECC in tension, which are part of the same experimental study (Li et al., 1994). For the linear elastic regions, the Young's modulus is $E_m = 90$ GPa and Poisson's ratio is $\nu = 0.2$. This higher Young's modulus is chosen to represent the larger out of plane thickness in the outer region. For the flexural reinforcement, Young's modulus $E_s = 210$ MPa and a yield strength $f_{rt} = 448$ MPa were chosen. The diameter of reinforcement bar is 20 mm. The embedment length of the reinforcement in the ECC material is 60 mm. With these input parameters, the tensile stress-strain response is in reasonable agreement with the experimental results in Li et al. (1994) as shown in Figure 4.11.

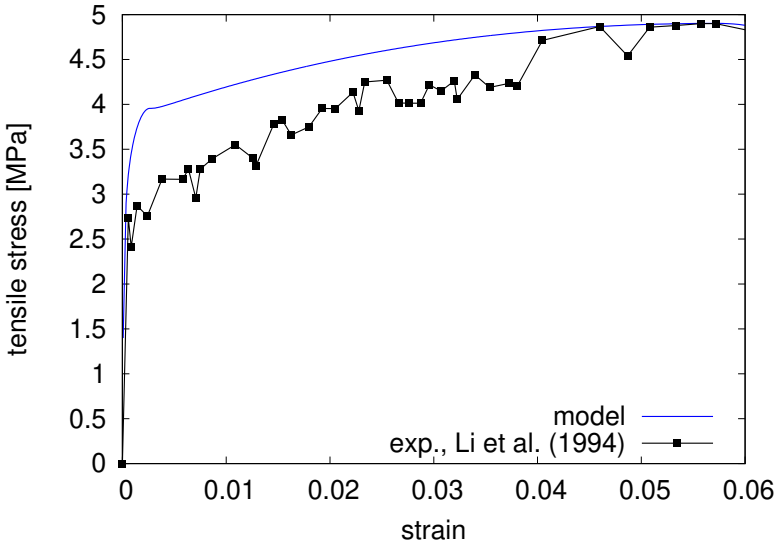

Figure 4.11: Model strain-stress curve under tension compared with experimental results reported in Li et al. (1994)

The main purpose of the shear test is to generate a constant shear force between loading points, so that the specimen is mainly subjected to shear. In the experiments in Li et al. (1994), the average shear strain is calculated by the measured displacements at two sets of four points in specimen as shown in Figure 4.10. With these two sets A and B, the horizontal strain ε_1, vertical strain ε_2 and diagonal strain ε_3 are calculated as described in Li et al. (1994). From these three strain components, the engineering shear strain is calculated as

$$\gamma_{\text{average}} = 2\varepsilon_3 - \varepsilon_1 - \varepsilon_2 \tag{4.1}$$

Here, the same approach is used for post-processing the FE results.

The comparison of shear stress and shear strain relation between model and experiment is shown in Figure 4.12. The model can generally predict the trend of the shear stress and shear strain curve in the experiments. The shear strain at peak

shear stress is almost same as in the experiment. However, the predicted peak shear stress is different, which might be due to the underlying CDPM2 model response and not due to the fibre extension. The first component of principal strainfor the three mesh sizes at a shear strain of 0.025 is shown in Figure 4.13. The strain is not localised at peak stress in the FE model. In Figure 4.13, the dark areas of the contour plot represents distributed cracks because even at high values of principal strain the material is still in the hardening stage. For the small element size of $h_{\mathrm{e}} = 1$ cm, a nonuniform strain distribution can be seen, which implies that distributed cracks form more likely at the top and bottom parts of the specimen at the peak value of shear stress. To illustrate the failure process, the evolution of the principal strain for the fine mesh is shown in Figure 4.14. The value of the first principal strain at the middle part of the specimen increases with further displacement as shown in Figures 4.14. The crack propagation process of the experiment is not described by Li et al. (1994). Still, this type of crack distribution is predicted for a similar short shear beam test for other models described in Kabele (2000) and Kanda et al. (1998).

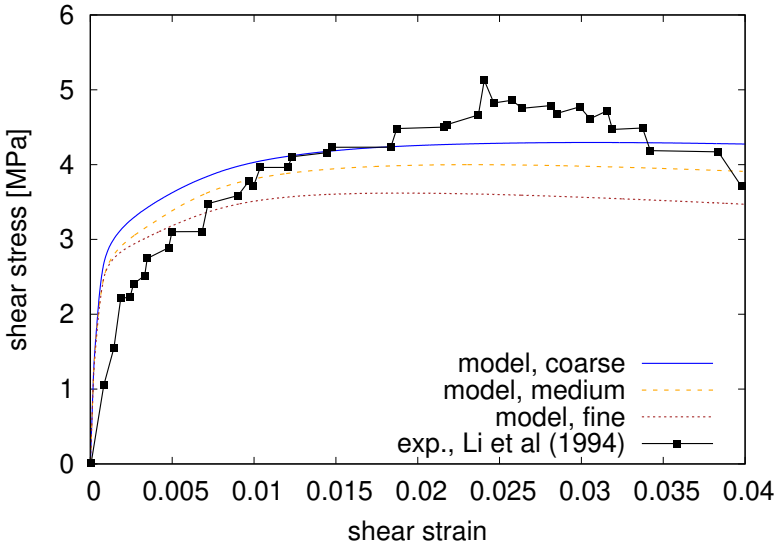

Figure 4.12: Model shear strain-shear stress curve of different mesh size compared with experiment. The experimental results are from Li et al. (1994)

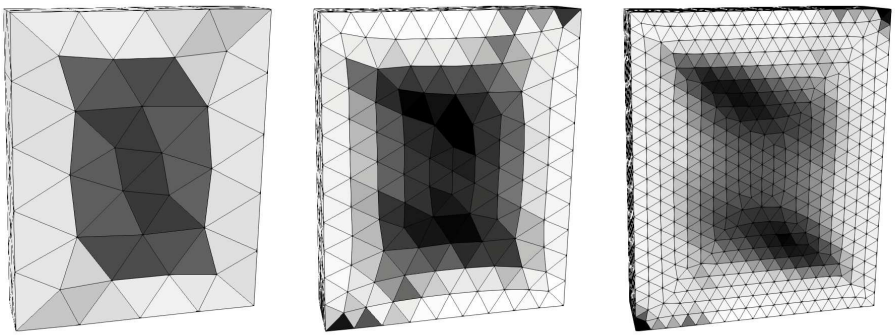

(a) (b) (c)

Figure 4.13: Contour plot of maximum component of principal strain at an average shear strain of 0.025: a) mesh size 4 cm, b) mesh size 2 m, c) mesh size 1 cm. Here, the colour black corresponds to a threshold of 0.02.

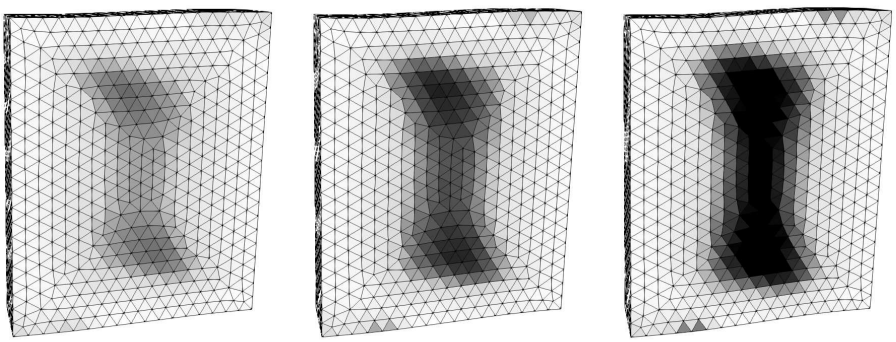

(a) (b) (c)

Figure 4.14: Contour plot of maximum component of principal strain at an average shear strain of : a) 0.05, b) 0.06, c) 0.07. Here, the colour black corresponds to a strain threshold of 0.06.

4.5 Compression

The last example is a compression test of an ECC cylinder tested in Zhou et al. (2014). The geometry and loading setup is shown in Figure 4.15a. The ECC specimen is loaded at the top and bottom by means of aluminium plates.

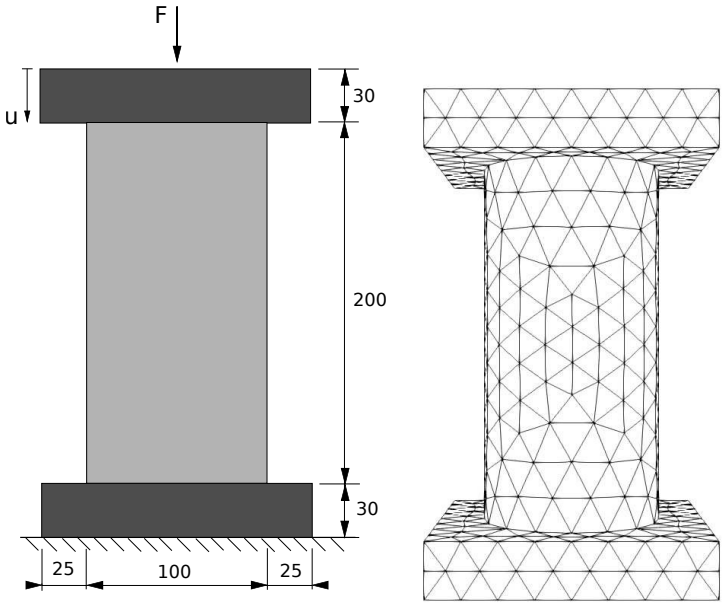

(a) (b)

Figure 4.15: a) Compression test geometry and loading setup based on experiments reported in Zhou et al. (2014) and b) FE mesh with element size 2 cm.

The three-dimensional finite element mesh shown in Figure 4.15 consists of tetrahedral constant strain elements which were generated with the mesh generator T3D (Rypl, 1998). Meshes of loading plates and specimen are conform. Therefore, there is no slip between specimen and loading plates. Three element mesh sizes were used with element size $h_{\mathrm{e}} = 4$, 2 and 1 cm to investigate the effect of mesh size on the results. This test differs from the tension and shear test, because the compressive response of CDPM2F is not affected by the bridging law that we introduced in the previous sections, so that for pure compression the response of CDPM2F is equal to the response of CDPM2. Therefore, we state here only the input parameters of the matrix. For the ECC cylinder, the input parameters are chosen as matrix Young's modulus $E_{\mathrm{m}} = 30$ GPa, Poisson's ratio $\nu = 0.2$, matrix tensile strength $f_{\mathrm{c}} = 2.2$ MPa, matrix compressive strength $f_{\mathrm{c}} = 39.28$ MPa

and matrix softening strain threshold for compression as $\varepsilon_f = 0.00001$. For the aluminium plates at the top and bottom of the specimen an elastic constitutive model is used with Young's modulus $E = 70$ GPa and Poisson's ratio $\nu = 0.2$. The stress-displacement curves of the finite element model with different element sizes are compared with the experimental results from in Figure 4.16.

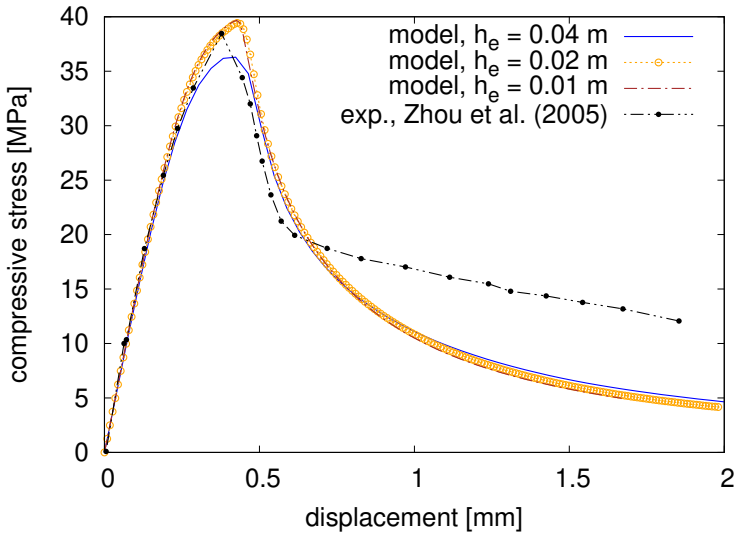

Figure 4.16: Stress-displacement curves for different mesh sizes of the structural model compared to experimental result. The experimental results are reported in Zhou et al. (2014).

Stress-displacement curves of models with different mesh sizes are agree well with experimental results. An almost mesh-independent response is observed. Contour plots of the vertical strain ε_{zz} for the three meshes are shown in Figure 4.17 for a vertical displacement of 0.6 mm (see Figure 4.16) for the three meshes. The model predicts distributed strains which are greatest in the middle of the specimen, because the edges are restrained by the loading platen.

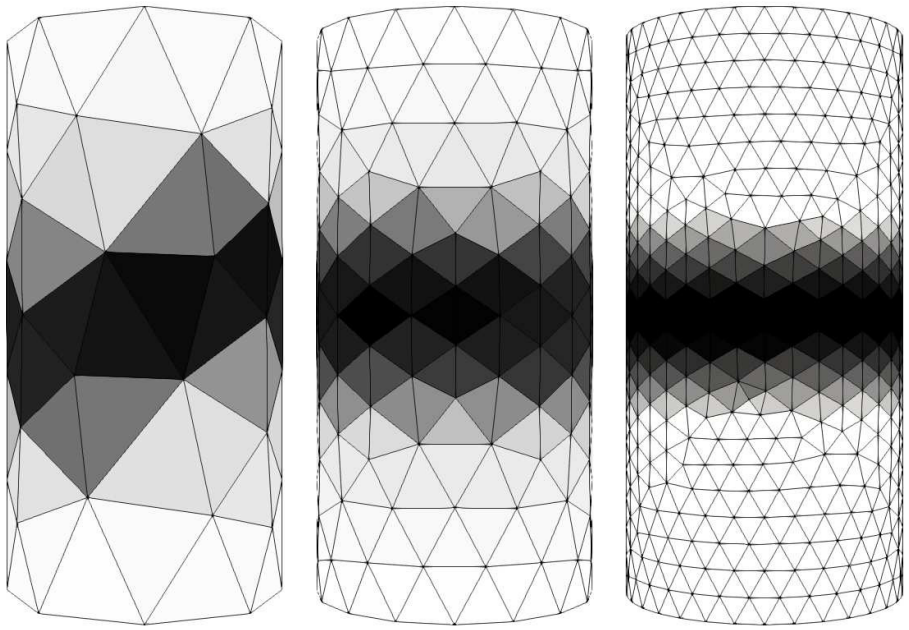

(a) (b) (c)

Figure 4.17: Influence of mesh size on zz component of strain tensor contour plot of compression tests at displacement 0.6 mm: a)mesh size 0.04 m, b)mesh size 0.02 m, c) mesh size 0.01 m.

Chapter 5

Structural component response modeled by CDPM2F

The numerical investigations carried out in this work are based on the experimental results reported in Moreno et al. (2014). Two of the matrix materials used in the experimental study are considered, which are concrete (C) and Engineered Cementitious Composite (ECC), which is a type of SHCC. In addition, a low strength version of the ECC model, called ECCLow, is used to illustrate the cracking process further. The material ECCLow is intended to reveal certain features which were demonstrated in Moreno et al. (2014) by a hybrid fibre reinforced model, which cannot be modelled by the constitutive model directly described in section 3.3.2. The finite element mesh is generated with the mesh generator T3D (Rypl, 1998). The finite element analyses are carried out with the open source finite element program OOFEM (Patzák, 2012).

5.1 Setup and input

R-C, R-ECC and R-ECCLow tensile tests are modelled to provide insight into the reinforcement matrix interaction. The numerical results are compared to the experimental data reported in Moreno et al. (2014); Moreno-Luna (2014), if applicable. Concrete is modelled with CDPM2 (Grassl et al., 2013). The ECC and ECCLow matrix materials are modelled with CDPM2F, which is described in section 3.3.2. For zero fibre volume, CDPM2F and CDPM2 are the same. The setup and geometry of the analysis is shown in Figure 5.1a. Concrete and ECC materials are modelled with 3D tetrahedral elements as shown in Figure 5.1b. The steel reinforcement bar is modelled with frame elements with fibre cross-sections. For each fibre of the cross-section a 1D elasto-plastic model with multi-linear hardening and softening is used. All these models are readily available in OOFEM (Patzák, 2012). Boundary conditions are applied at the ends of reinforcement. Pre-described displacement is applied. In trial analyses, I observed that it is important to use frame instead of truss elements, so that once the matrix cracks, the reinforcement bar can still resist bending. With truss elements, large lateral displacements of the reinforcement bar were present so that cracking of the matrix occurred only on side of the specimen. This excessive lateral displacement was avoided by using frame elements. In the experiments, the ends of the specimens were reinforced with steel cages so that cracking at the end of the specimens is prevented. In the analyses, effect of these cages is approximated by increasing the strength of the end parts of the reinforcement bars as shown in Figure 5.1a. I do not consider explicitly bond between steel and matrix. Instead, a merged approach is used in which the nodes of the reinforcement and matrix have the same degrees of freedom. For this, I initially generate the meshes of matrix and reinforcement bar seperately, i.e. the vertices of the lines representing the reinforcement bar are not at the same position

as the vertices of the tetrahedra for the matrix. I then place in the tetrahedral elements of the matrix hanging nodes at the location of the reinforcement vertices. These hanging nodes are then used as the nodes of the reinforcement elements. In Grassl et al. (2018) it was shown that this approach produces acceptable results for good bond conditions as long as the matrix is modelled in 3D. Damage in the matrix adjacent in the reinforcement bar will produce relative displacements between steel bar and matrix so that crack formation in reinforced concrete can be reproduced so that the overall load-displacement curve is not strongly affected by the mesh size (Grassl et al., 2018). It was shown that there is a slight mesh dependence in the crack patterns obtained. I discuss the topic of bond-slip in more detail in section 5.3. The results of the analyses are later shown in the form of load versus average strain of the reinforcement, which is calculated as the relative displacement between points B and A divided by the length of these two points (Figure 5.1a).

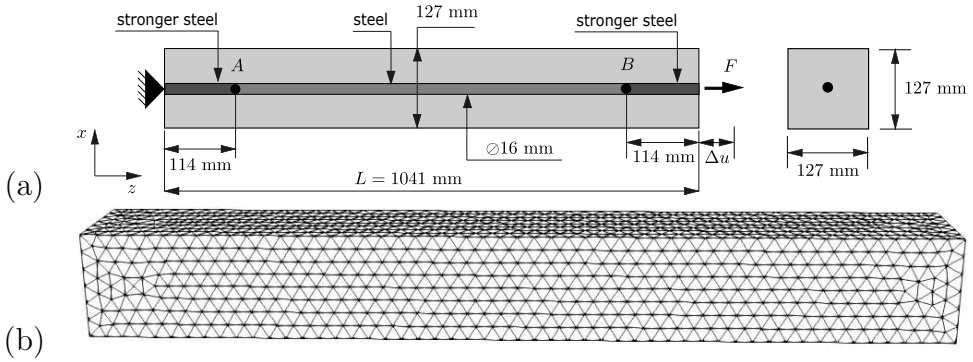

Figure 5.1: a) Geometry and setup of R-ECC specimen subjected to tension based on experiments in Moreno et al. (2014) and b) three-dimensional tetrahedral finite element mesh with an element size of 2 cm.

The total length of the specimen is 1041 mm. The edge length of the square cross-section is 127 mm. The diameter of reinforcement bar which is placed centrically in

the specimens is 16 mm. For concrete, the model input parameters for the matrix are Young's modulus $E_{\mathrm{m}} = 30$ GPa, Poisson's ratio $\nu = 0.2$, tensile strength $f_{\mathrm{t}} = 1.4$ MPa, compressive strength $f_{\mathrm{c}} = 44$ MPa and crack opening threshold $\delta_{\mathrm{f}} = 0.185$ mm for an exponential softening curve. The other parameters are given default values as introduced in Grassl et al. (2013). From these parameters, f_{t} and f_{c} are directly chosen from Moreno et al. (2014). The other parameters were given reasonable values for mortar.

For ECC, Young's modulus of the matrix is $E = 20$ GPa, the tensile strength of matrix is $f_{\mathrm{t}} = 2.9$ MPa, the compressive strength of matrix is $f_{\mathrm{c}} = 54$ MPa and $\delta_{\mathrm{f}} = 0.01$ mm for the exponential softening curve. Here, f_{t} and f_{c} are chosen from the experiments in Moreno et al. (2014). The hardening modulus of the plasticity model is chosen as $H_{\mathrm{p}} = 0.05$, which is a slightly larger than the default value of the hardening parameter for concrete recommended in Grassl et al. (2013), so that the debonding part of the fibre bridging stress response is reproduced correctly. The effect of H_{p} on the ECC response was discussed in Zhou et al. (2024). The fibre properties obtained from the experiments are $l_{\mathrm{f}} = 12.7$ mm, $d_{\mathrm{f}} = 40$ μm, $V_{\mathrm{f}} = 0.02$ and $E_{\mathrm{f}} = 43$ GPa. The other fibre model input parameters are $f = 0.9$, $\beta = 0.02$, $\tau_0 = 0.5$ MPa, $s_{\mathrm{m}} = 100$ mm, $\xi = 0.3$, $\alpha = 0.9$ and $V_{\mathrm{f0}} = 0.02$. Here, E_{f}, L_{f}, d_{f} and V_{f0} are chosen from Moreno et al. (2014). The other parameters were chosen so that the response agreed with the experimental results of ECC in tension shown Figure 5.2 in the form of stress versus average strain computed from the displacement of a specimen of 200 mm gauge length. The stress-strain curves agree well mainly because I adjusted the free parameters of CDPM2F to achieve this fit. For for the low strength ECC material ECCLow, $f_{\mathrm{t}} = 2.9$ MPa, $f_{\mathrm{c}} = 54$ MPa, $V_{\mathrm{f0}} = 0.011$ and $\alpha = 0.92$. All other parameters are the same as for the ECC material.

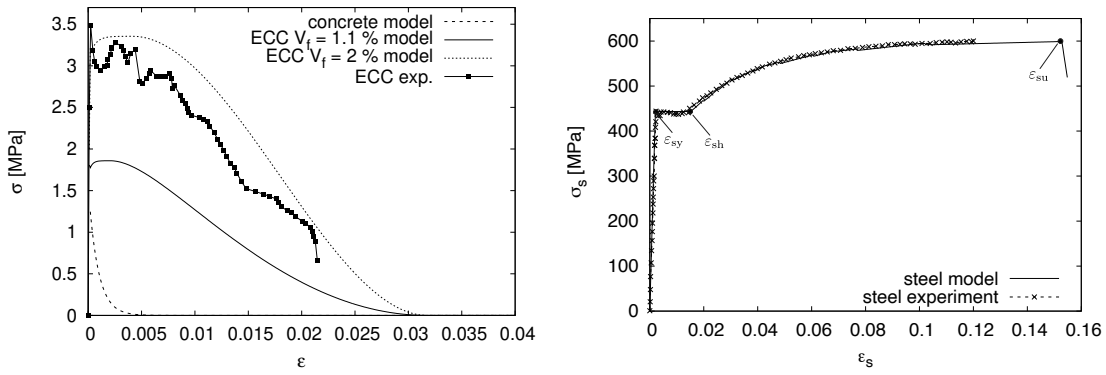

Figure 5.2: Material input: a) stress versus strain for R, ECC, ECCLow, and b) stress versus strain for the steel reinforcement bar. For ECC and steel, the results are compared with experimental results reported in Moreno et al. (2014).

For the reinforcement, the inelastic steel response is important for reproducing the experimental results of the composites. The hardening and softening response of the bare steel curve reported in Moreno et al. (2014) was used in the 1D elasto-plastic. The key parameters of this response are Young's modulus $E_{\mathrm{s}} = 210$ MPa, yield strength $f_{\mathrm{ys}} = 448$ MPa and strain $\varepsilon_{sy} = 0.00213$, strain at onset of hardening $\varepsilon_{sh} = 0.015$, ultimate strength $f_{\mathrm{us}} = 591$ MPa and strain $\varepsilon_{su} = 0.15$ as reported in Moreno et al. (2014). The response of the model compared to the experimental results available in Moreno et al. (2014) is shown in Figure 5.2b.

5.2 Analysis and results

The results of the analyses of R-C and R-ECC tests modelled with CDPM2F and CDPM2 are shown in this section. I use three main ways of presenting the results. Firstly, I compare the load versus average strain curves with the corresponding experimental results. In addition, to provide insight why these results are obtained,

I present the axial stress and strain distribution of the reinforcement and contour plots of the maximum principal strain component of the matrix. I choose the maximum principal strain as the variable for the contour plots, because this variable represents well localised strain profiles obtained in the model which represent cracks.

5.2.1 R-C modelled with CDPM2

For reinforced concrete, called here R-C, the load-strain curve is compared in Figure 5.3a with experimental results reported in Moreno et al. (2014).

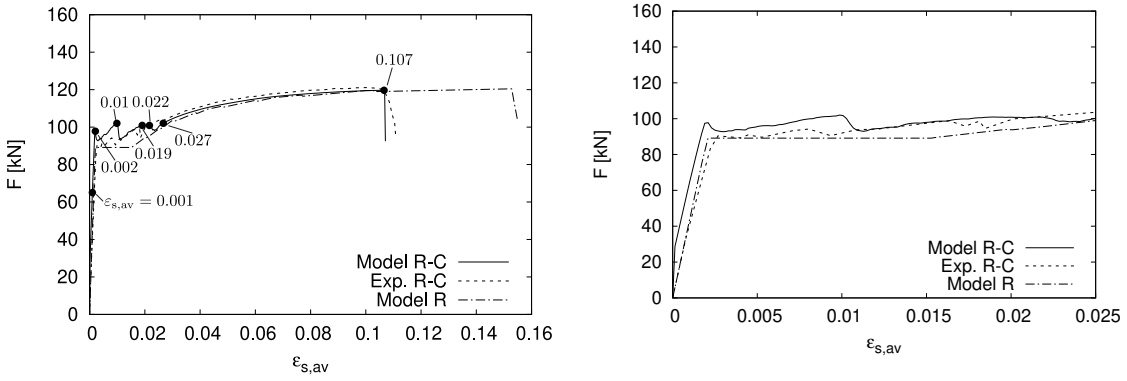

(a) (b)

Figure 5.3: R-C test: Load versus average strain from model compared to experiments in Moreno et al. (2014). Marked points in load-average strain curve.

Overall, the load-strain curve in Figure 5.3a is in good agreement with the experiments. The response is ductile and very similar to the bare steel response. The strain capacity in the model is 0.107, which agrees well to the experimental strain capacity of 0.102. This value is less than the strain capacity of the reinforcement of $\varepsilon_{su} = 0.015$, because of concrete carrying stresses between cracks. By studying

the initial part of the load-strain curve in Figure 5.3b, it can be seen that there is very little additional bridging stress provided by the concrete matrix, which is probably due to the brittle nature of concrete shown in Figure 5.2a. Both mechanisms, namely stresses carried between cracks and stresses carried across a crack, contribute usually to the tension stiffening effect observed in reinforced composites. For reinforced concrete, the the effect of stress carried across cracks is small. Therefore, tension stiffening for R-C is mainly due to stresses carried in the matrix between cracks.

The points marked in Figure 5.3a are stages in the loading process which are used to visualise the results further. Firstly, the axial steel strain and stress versus the z-coordinate along the reinforcement bar is shown in Figure 5.4a and b, respectively, for the stages marked in Figure 5.3a.

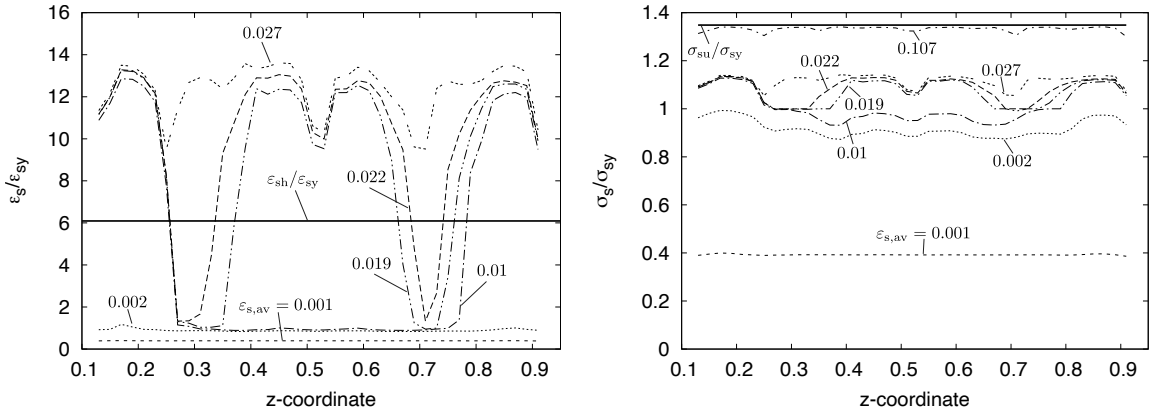

(a) (b)

Figure 5.4: R-C: Normalised axial steel a) strain versus z-coordinate and b) stress versus z-coordinate. The strain and stress are normalised by the yield strain and stress, respectively.

It can be seen that with increasing average strain, the strain and stress distribution in Figure 5.4 becomes nonuniform. Since the overall axial force in the specimen

is in equilibrium, the stress and strain in the steel must be greater in a region in which the matrix cracks than in a region in which the matrix is not cracked. Consequently, the peaks of the steel strain and stress in Figure 5.4 represent cracks in the concrete matrix. In total, there are seven cracks visible at the end of the analysis. The evolution of cracks in the matrix is visualised in the form of contour plots of the maximum principal strain shown in Figures 5.5 to 5.7. For the first two stages with average strains of 0.001 and 0.002, the average response is shown in Figure 5.5a and b, respectively. For these average strain levels, the yield strength of the reinforcement bar is not reached. At a strain of 0.001, two cracks form at both ends of the specimen adjacent to the strengthened regions as shown in Figure 5.5a. Just before the onset of yielding at an average strain of 0.002, all seven cracks visible in the final configuration are formed as it can be seen in Figure 5.5b. The openings of these cracks are still small at this stage of average strain. Still, cracking occurs at this average strain, because for a concrete tensile strength $f_{\mathrm{t}} = 1.4$ MPa and Young's modulus $E = 30$ GPa, the strain capacity in tension is $f_{\mathrm{t}}/E = 0.000047$, which is considerably smaller than the steel yield strain of $\varepsilon_{\mathrm{y}} = 0.016$.

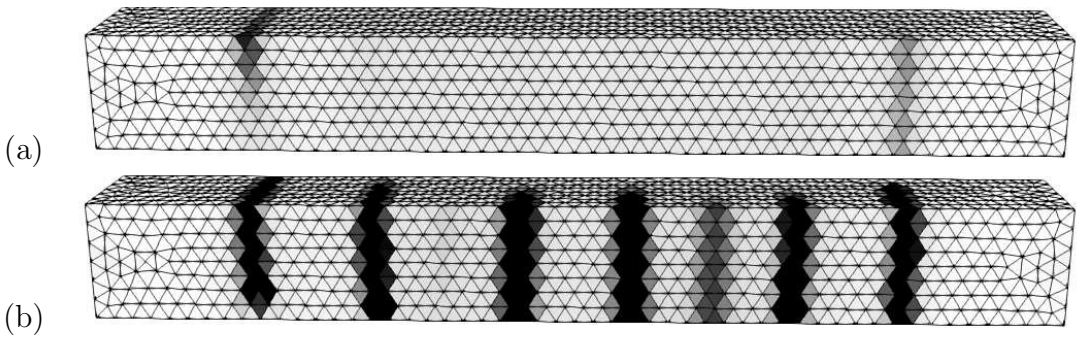

Figure 5.5: R-C test: Contour plot of maximum principle concrete strain at an average steel strain at a) 0.001 and b) 0.002. The upper threshold for the maximum strain was chosen as 0.004 and is shown in black.

For an average strain from 0.002 to 0.03 as marked in Figure 5.3, unloading and reloading of the force for monotonically increasing average strain can be observed. This occurs after the yield strength of the reinforcement bar has been reached. In Figures 5.6 and 5.7 contour plots of the maximum component of principal strain for an average strain of 0.01, 0.019, 0.02 and 0.027 are shown.

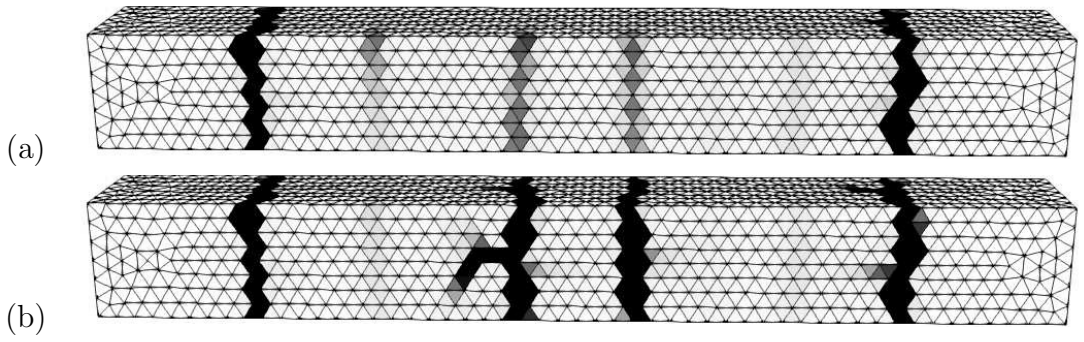

Figure 5.6: R-C test: Contour plot of the maximum principle concrete strain at an average steel strain of a) 0.01 and b) 0.019. The upper threshold for the maximum concrete strain was chosen as 0.015 and is shown in black.

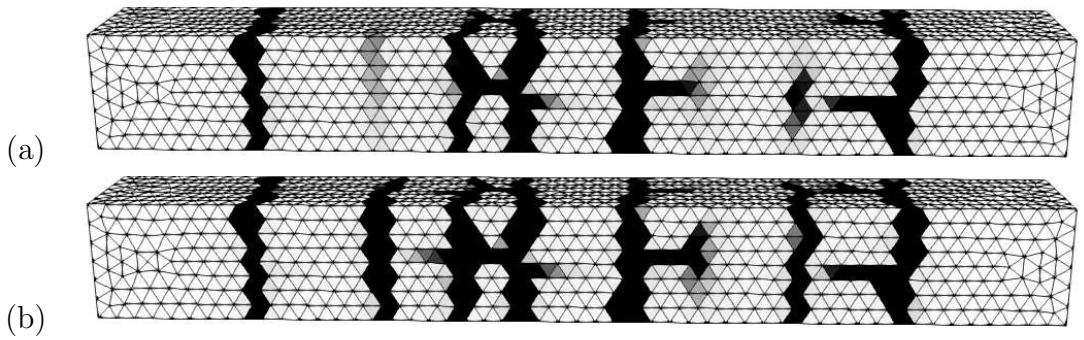

Figure 5.7: R-C test: Contour plot of maximum principle concrete strain at an average steel strain of the steel bar of a) 0.021 and b) 0.027. The upper threshold for the maximum concrete strain was chosen as 0.015 and is shown in black.

A larger threshold of 0.021 is selected for these contour plots to identify cracks with wider crack openings. It can be observed in Figure 5.4a and 5.4b that the non-uniformity of both strain and stress distributions are decreasing with increasing

crack-openings. As shown in Figure 5.4b, at an average strain of 0.03, the difference in axial steel stress in cracked and uncracked regions is much lower than at the onset of cracking at an average strain of 0.002. For the range of average strain of 0.030 to 0.105, the load-strain curve of R-C almost overlaps with the curve of the bare steel bar. The shape of curves of the steel stress along the reinforcement bar barely change in this range. The value of stress and strain almost uniformly increased along the reinforcement bar at this stage until most area of reinforcement bar reaches the ultimate stress of steel. Overall, from these results, the typical process of the formation of multiple cracks in reinforced concrete can be seen. Already before yielding, all cracks are initiated. For strains greater than the strain at the onset of yielding, the total load of the R-C composite is only slightly above the load of the bare reinforcement bar, which is due to the interplay of hardening reinforcement and the tension stiffening effect of the composites. The difference between the total load and the load of the bare steel reinforcement decreases as the cracks are opening. At the ultimate strain of the rebar, these two load levels are almost the same.

5.2.2 R-ECC modeled with CDPM2F

In the second part of the analyses, I modelled R-ECC with CDPM2F. For this ECC matrix, experimental results are available in Moreno et al. (2014). The load-strain curve is shown in Figure 5.8a.

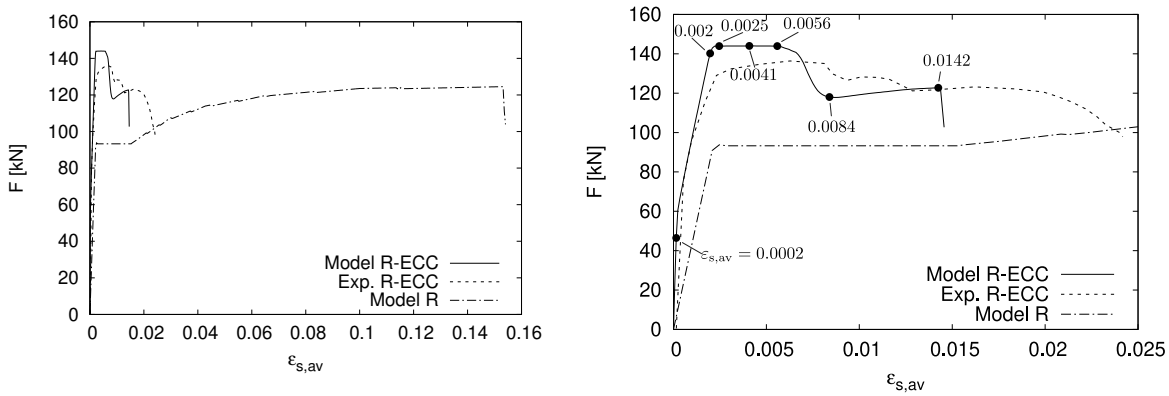

(a) (b)

Figure 5.8: R-ECC: a) Load versus average strain from model compared to experiments in Moreno et al. (2014), b) Marked points in load-average strain curve compared with bare reinforcement response.

For R-ECC, the load-strain curve agrees well with the experimental results in Moreno et al. (2014). The overall shape of load-strain curve is the same as in the experiments. The matrix response has a significant effect on the load strain response of R-ECC, due to the bridging stress provided by the fibres. The total load capacity at the onset of steel yielding is more than 50 % greater than the yield force of the steel. This is a significant difference to load-strain response for R-C. The effect of the bridging stress of the matrix material on the load strain curve has been described in Fischer and Li (2015), Liu et al. (2023) and Moreno et al. (2014).

In Figure 5.8b, the initial range of the average load strain curve obtained from the model is shown with points marked at which the response of composite is further investigated by plots of the steel stress and strain along the axis of the reinforcement bar, as well as contour plots of the maximum principal strain. The load-strain curve can be divided into three parts, namely hardening of ECC and

steel, softening of ECC and hardening of steel, and finally, softening of ECC and softening of steel. The three parts of the process are studied by normalised steel strain and stress versus z-coordinate plots in Figure 5.9a and b, respectively.

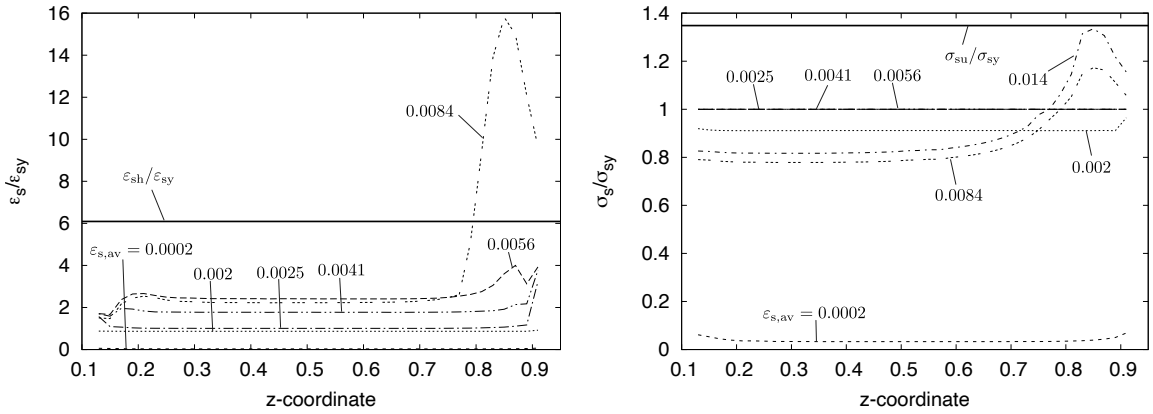

Figure 5.9: R-ECC: Normalised axial reinforcement a) strain versus z-coordinate and b) stress versus z-coordinate.

Furthermore, the contour plots of the maximum principal strain are shown in Figure 5.10 and 5.11.

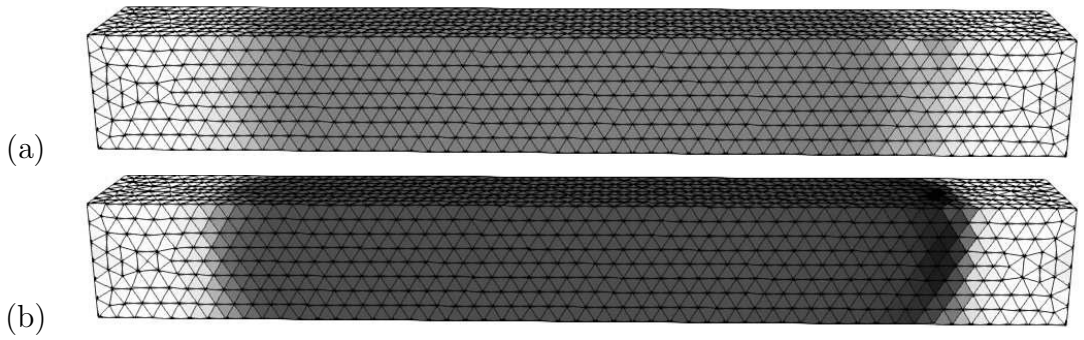

Figure 5.10: R-ECC: Contour plot of maximum principle ECC strain at an average steel strain of the reinforcement bar of a) 0.002 and b) 0.0025. The upper threshold for the maximum strain was chosen as 0.0024 and is shown in black.

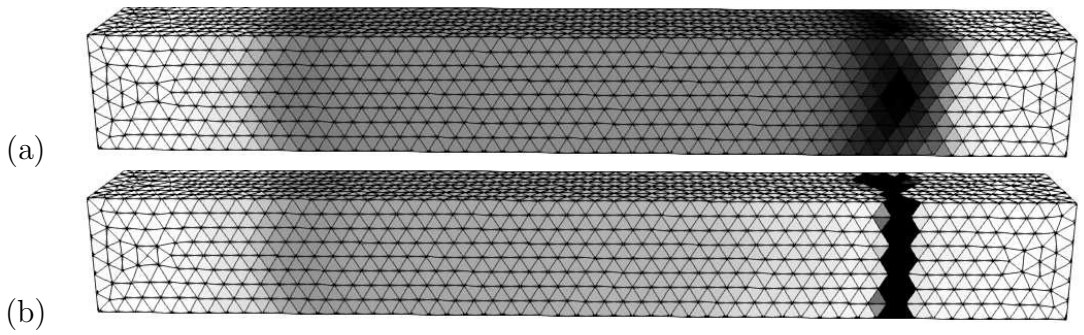

Figure 5.11: R-ECC: Contour plot of maximum principle ECC strain at an average steel strain of the reinforcement bar of a) 0.0041 and b) 0.0056. The upper threshold for the maximum strain was chosen as 0.0053 and is shown in black.

With the steel strain and stress distributions and the maximum principal strain contour plots, the failure process is illustrated. Initially, both the ECC matrix and the reinforcement bar behave elastically. At an average strain of 0.0002, the model results show that both reinforcement bar and ECC matrix are in the elastic range. The maximum principal stress in the matrix is 2.5 MPa, which is below the tensile strength of ECC matrix. The information about principal stresses is retrieved from the output of the analysis, but is not shown here, because it is difficult to present it clearly graphically, since the stress does not localised. From the stress distribution along the reinforcement bar shown in Figure 5.9a, it is seen that the axial stress along the reinforcement bar is smaller than the yield strength of reinforcement.

At an average strain of $\varepsilon_{\mathrm{s},av} = 0.002$, the reinforcement bar is still just in the elastic range, but the ECC matrix is in the cracking strain hardening stage (Figure 5.10a). The normalised axial stress along the reinforcement bar in Figure 5.9b is slightly smaller than 1, which indicates that the reinforcement bar is still elastic at this stage. In CDPM2F model, fine cracks in the distributed cracking stage are described with distributed cracking strain. Therefore, individual cracks are not

visible. This distributed cracking results in a lower slope of R-ECC load strain curve than the initial elastic response. At this stage, the maximum principal stress of model is 3.346 MPa, which is above the tensile strength of ECC of 2.9 MPa and below the stress capacity of $\sigma_{cu} = 3.354$ MPa.

At the average strain of $\varepsilon_{s,av} = 0.00246$, the reinforcement bar reaches the yield strength and ECC matrix is still at strain hardening stage. The principal stress of the ECC matrix is now 3.353 MPa, which is close to the stress capacity $\sigma_{cu} = 3.354$ MPa. The maximum normalised stress in the reinforcement bar show in Figure 5.9b is now equal to 1. This shows that the reinforcement bar has reached the yield strength of steel. The normalised strain distribution of reinforcement bar is non-uniformed as shown in Figure 5.9a, which is above yield strain of reinforcement bar and below the hardening strain of reinforcement. The stages with average strains of $\varepsilon_{s,av} = 0.0041$ and 0.0056 are chosen to elucidate the material response during strain softening of matrix. At an average strain of $\varepsilon_{s,av} = 0.0041$, the axial stress in the reinforcement bar is still equal to yield strength as shown in Figure 5.9b. The principal strain distribution of reinforcement bar shows higher value at end of rebar, where Figure 5.11a shows localised regions of maximum principal strain at the same position. At this strain, the maximum component of the principal stress of matrix in this area is slightly lower than σ_{cu}. These results indicate that, for the present configuration, the reinforcement bar does not reach the hardening stage until softening of the matrix occurs.

At an average strain of $\varepsilon_{s,av} = 0.0056$ in the R-ECC model, strain localisation becomes evident. As depicted in Figure 5.11b, regions of localised strains can be observed, with the dark regions corresponding to high values of the maximum principal strain. Notably, the axial strain within the reinforcement in thesis localised area surpasses that of other reinforcement segments significantly. In particular,

the principal strain values within the z-coordinate range of 0.8 to 0.9 exceed the hardening strain threshold of the reinforcement. Conversely, the axial strain in the other regions remains lower than the axial reinforcement strain observed for $\varepsilon_{s,av} = 0.0043$. This is indicative of reinforcement unloading. Figure 5.9b exhibits a similar response, where the axial stress in the reinforcement bar exceeds the yield strength and enters the hardening phase within the same z-coordinate range of 0.8 to 0.9. Meanwhile, the stress in other parts remains below the yield strength, as shown in Figure 5.9b.

In the range of average strains varying from 0.0056 to 0.0142, a part of the steel reinforcement progresses into the hardening stage. This part is where ECC is softening, which results in an almost zero bridging stress. As depicted in Figure 5.9b, the axial stress within the reinforcement in the weak zone of the matrix surpasses the hardening stress threshold, whereas in other regions, the stress remains below the yield strength, which constitutes the typical tension stiffening effect of steel reinforced composites. In these regions, the highest maximum component of the principal stress of the matrix is 3.03 MPa, which does not reach the ultimate tensile stress $\sigma_{cu} = 3.354$ MPa, thereby preventing the formation of a second crack.

The load-strain responses of R-ECC is very different of R-C. Considering the matrix response in Figure 5.2, strain hardening of ECC results in higher tensile strain capacity and higher tensile stress capacity than of plain concrete. Here, tensile strain capacity is defined as the strain at which the the tensile stress capacity is reached. This strain capacity is the main reason for the difference in behaviour of R-ECC and R-C. For both R-ECC and R-C, when the first localised crack in the matrix is initiated, there is a slip between matrix and reinforcement bar adjacent to the crack. This slip results in additional tensile strain of the matrix adjacent to the crack. For concrete, this additional strain results in additional cracks, as was

demonstrated in detail for R-C case, because the strain capacity of plain concrete in tension, i.e. the strain at which the tensile strength is reached, is very small. However, for ECC the strain capacity is much larger. Therefore, this additional strain due to the slip between reinforcement and matrix does not result in additional cracking away from the first crack formed. It could be argued that if the slip between ECC and reinforcement bar is large enough, then multiple cracks should also appear in the R-ECC case. However, for R-ECC, the load-strain response is not only governed by the matrix property, but also by the nonlinear response of the reinforcement bar within the region of localised cracks. For the present setup, the maximum stress of the reinforcement bar is reached before sufficient strains are generated to produce ECC cracking. Once the steel has reached its ultimate stress, the overall failure of the composite occurs.

This apparent drawback of R-ECC can be mitigated by lowering the strain capacity of ECC, so that multiple cracks occur, or by increasing the ductility of the steel. Here, I demonstrate the effect by simulating the response of the composite with a matrix material with lower stress and strain capacity, which we call ECCLow. The matrix response in tension of this material is shown in Figure 5.2. The load-strain curve of R-ECCLow and bare steel is shown in Figure 5.12a. A detailed first part of the response is shown in Figure 5.12b with averaged strain stages marked at which more detailed results are shown.

In Figure 5.13, the axial stress and strain along the reinforcement bar are shown at marked points presented in Figure 5.12.

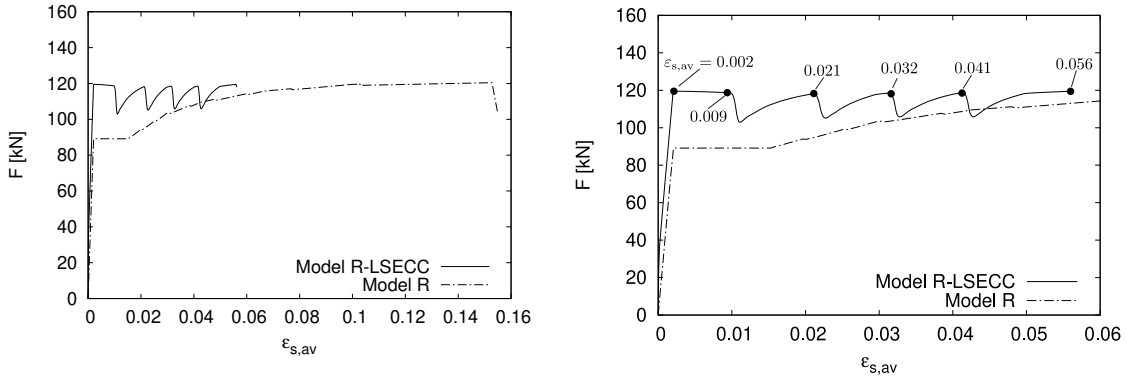

(a) (b)

Figure 5.12: R-ECCLow: a) Load versus average strain from model, b) Marked points in load-average strain curve compared with bare reinforcement response from model.

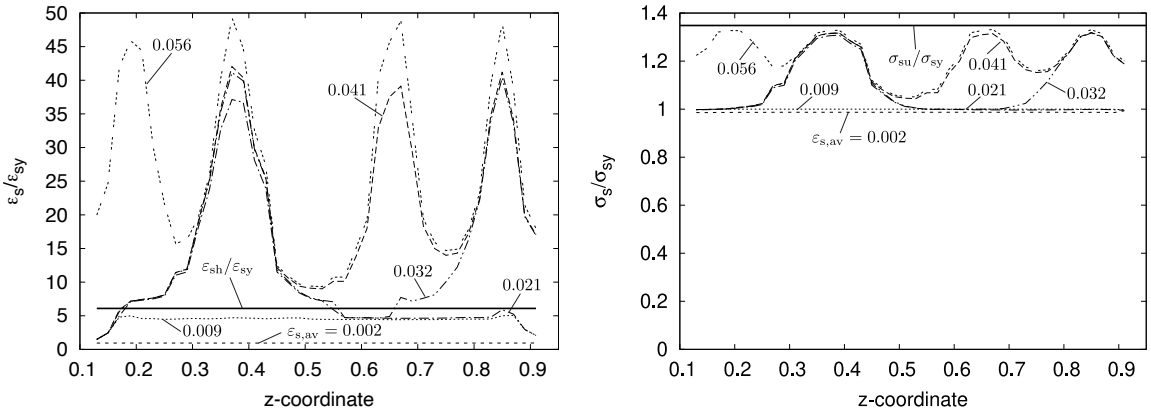

(a) (b)

Figure 5.13: R-ECCLow: Axial nomalised reinforcement a) strain versus z-coordinate and b) stress versus z-coordinate.

From the axial strain distribution in Figure 5.13a, the formation of multiple cracks is visible. Unlike for RC, the first dominant crack is formed after the yield strength of the reinforcement bar is reached. This is because ECCLow is much more ductile than C. At and average strain of 0.056, four dominant cracks are visible from the contour plot of the maximum principal strain in Figure 5.14.

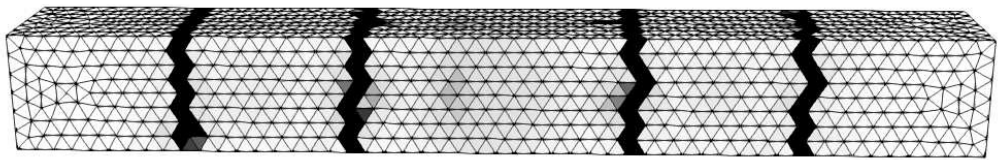

Figure 5.14: R-ECCLow: Contour plot of maximum principle ECCLow strain at an average steel strain of the reinforcement bar of 0.0561. The upper threshold for the maximum strain was chosen as 0.021.

The results demonstrate that both matrix and reinforcement reinforcement response has to be carefully selected to ensure a ductile response of the composite, so that the benefits of a ductile matrix material in the form of greater ductility and durability is maintained for reinforced composites. In Moreno et al. (2014), a response similar to our R-ECCLow results has been obtained experimentally with a hybrid fibre reinforced material, which has a much lower matrix strain capacity than the ECC material used here. Furthermore, in Liu et al. (2023) it was shown that for a certain combination of R and ECC, average strain capacities of the steel reinforced composite of more than 6 % can be obtained.

5.3 Investigation of bond-slip

The modelling in the previous section is based on a merged approach. This means that the nodes of the beam elements have the same DOFs as the nodes of the matrix elements. In a recent study, the ability of this approach to simulate the failure process of reinforced concrete mesh-independently was studied in Grassl et al. (2018) with the constitutive model CDPM2. It was found that there was a mild mesh dependence on the number of cracks generated. However, this apparent mesh dependence was much less severe than expected for an apparent perfect bond

approach. In Grassl et al. (2018), it was shown that inelastic processes occur in elements adjacent the reinforcement, so that a slip between reinforcement and matrix is facilitated. In Grassl et al. (2018), the study was limited to R-C. Here, I investigate the response between cracks for all three combinations used in the present study. The contour plot of the maximum principal strain for a cut at the level of the reinforcement is shown in Figure 5.15.

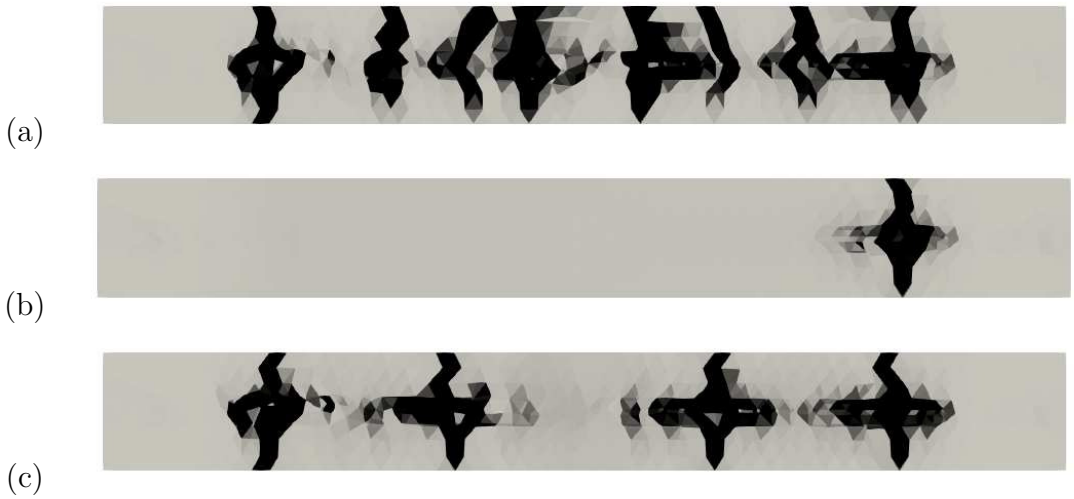

Figure 5.15: Contour plot for the maximum component of the principle strain of mesh size 2 cm for a) R-C, b) R-ECC and c) R-lsECC for a cut through the specimen at the level of reinforcement. The upper threshold (shown as black) for the maximum strain was chosen as 0.03.

We can see that in all three cases, there are a large maximum principal strains in the elements adjacent to the beam elements. This indicates that bond slip is facilitated so that the typical crack patterns known from reinforced concrete can be generated with a 3D modelling approach.

Chapter 6

Conclusion

This section summarises the main conclusions and recommendations for future work.

6.1 Conclusions

Based on the work presented in the previous chapters, I arrive at the following conclusions.

- The new model CDPM2F is capable of linking fibre properties to composite response.
- Dispersion of fibres is successfully incorporated by the parameter α, which represents the degree of variation of the spatial fibre distribution.
- CDPM2F is able to reproduce the three-dimensional structural behaviour of components made of ECC.

- CDPM2F produces results for ECC subjected to tension, compression and shear, which do not exhibit pathological mesh-dependence.
- CDPM2F is capable of revealing the interaction between the reinforcement bar and matrix. The R-ECC model results reveal the evolution of the material failure.
- CDPM2F is able to show different failure modes of steel combined with ECC for different ultimate strength of the ECC matrix.
- For R-C and R-ECC, the difference in ductility is related to uniformity of strain distribution along the steel reinforcement bar. The use of a strain hardening matrix such as ECC leads to a reduced overall ductility. This reduction of ductility is strongly dependent on the interplay between the ultimate matrix stress and ultimate steel stress.
- If the combination of matrix and reinforcement is designed carefully, unfavourable failure modes can be avoided. Therefore, it is important to have material models for the matrix which are a function of fibre properties. In this way, structural behaviour based on fibre properties can be determined.

Overall, this research links micro-mechanical response of fibre/matrix scale to macroscopic response of SHCC. Overall, this method is valid for modelling structural behaviour of SHCC. Furthermore, R-ECC tensile response is also well explained by this CDPM2F model.

6.2 Limitations and Recommendation for future work

The model has potential to be extended and improved. At present, one way pull-out fibre stress-crack opening law is adapted. In future, more accurate two-way pull-out model could also be adapted to improve the model. Effect of flaws distribution is not included in this model. As I proposed a sigmoid relation to reflect overall cracking strain to crack opening. A parameter ξ is used to control the slope. The relation of flaw distribution to ξ, could also be investigated in future.

Strain rate dependence is also another area could be further investigated. ECC tensile response for different strain rates is dependent on micro-mechanical properties of fibres/matrix. Phenomenological models cannot capture this effect. Potentially, this model can reflect strain rate dependence of overall response based on micro-mechanical properties. It could benefit the modelling of dynamic problems of ECC or R-ECC, where it has shown that ECC has a good performance in dynamic response.

Bibliography

Bažant, Z. P. and Nguyen, H. T. Proposal of m-index for rating fracture and damage models by their ability to represent a set of distinctive experiments. *Journal of Engineering Mechanics*, 149(8):04023047, 2023.

Bažant, Z. P.; Nguyen, H. T., and Dönmez, A. A. Critical comparison of phase-field, peridynamics and crack band model M7 in light of gap test and classical fracture tests. *Journal of Applied Mechanics*, pages 1–79, 2022.

Bažant, Z. P. and Oh, B.-H. Crack band theory for fracture of concrete. *Materials and Structures*, 16:155–177, 1983.

Bian, Y.; Xiong, F.; Liu, Y., and Ge, Q. Flexural performance of novel ECC-RC composite sandwich panels. *Engineering Structures*, 292:116547, 2023.

Ding, M.; Xu, W.; Wang, J.; Chen, Y., and Fang, R. Analytical study on seismic performance of ECC shell-RC column and its plastic hinge forming mechanism. *Structures*, 58:105489, 2023.

Ding, Y.; Yu, K., and Li, M. A review on high-strength engineered cementitious composites (HS-ECC): Design, mechanical property and structural application. *Structures*, 2022.

D.Liu, ; Qin, F.; J.Di, , and Z.Zhang, . Flexural behavior of reinforced concrete

(RC) beams strengthened with carbon fiber reinforced polymer (CFRP) and ECC. *Case Studies in Construction Materials*, 19:e02270, 2023.

Fischer, G. and Li, V. C. Influence of matrix ductility on tension-stiffening behavior of steel reinforced engineered cementitious composites (ECC). *ACI Structural Journal*, 99(1):104–111, 2015.

Grassl, P.; Xenos, D.; Nyström, U.; Rempling, R., and Gylltoft, K. CDPM2: A damage-plasticity approach to modelling the failure of concrete. *International Journal of Solids and Structures*, 50(24):3805–3816, 2013.

Grassl, P.; Johansson, M., and Leppänen, J. On the numerical modelling of bond for the failure analysis of reinforced concrete. *Engineering Fracture Mechanics*, 189:13–26, 2018.

Halvaei, M.; Jamshidi, M.; Latifi, M., and Behdouj, Z. The effect of nylon fibers on mechanical properties of engineered cementitious composites (ECCs). In *The fourth International Conference on Concrete & Development*, 2013.

Huang, T.; Zhang, Y. X.; C.Su, , and Lo, R. Effect of slip-hardening interface behavior on fiber rupture and crack bridging in fiber-reinforced cementitious composites. *Journal of Engineering Mechanics*, 141(10), 2015.

J.Jia, ; Zhou, ; Jin, L.; Pan, C., and Leung, K. Y. Mechanical behavior of fiber-reinforced engineered cementitious composites in uniaxial compression. *Journal of Materials in Civil Engineering*, 2015.

Kabele, P. *Assessment of structural performance of engineered cementitious composites by computer simulation*, volume 5.2001. Czech Technical University, 2000.

Kabele, P. Multiscale framework for modeling of fracture in high performance fiber reinforced cementitious composites. *Engineering Fracture Mechanics*, 74 (1-2):194–209, 2007.

Kabir, M.I; Lee, C. K., and Zhang, Y.X. Chapter 15 - finite element analysis of engineered cementitious composite (ECC) encased steel composite beams subjected to bending. In Zhang, Y.X. and Yu, Kequan, editors, *Advances in Engineered Cementitious Composites*, Woodhead Publishing Series in Civil and Structural Engineering, pages 471–500. Woodhead Publishing, 2022.

Kanda, T. and Li, V. C. Practical design criteria for saturated pseudo strain hardening behavior in ECC. *Journal of advanced concrete technology*, 4(1):59–72, 2006a.

Kanda, T. and Li, VC. Practical design criteria for saturated pseudo strain hardening behavior in ecc. *Journal of advanced concrete technology*, 4(1):59–72, 2006b.

Kanda, T.; Lin, Z., and Li, V. C. Application of pseudo strain-hardening cementitious composites to shear resistant structural elements. In *Proceedings of the 10th International Conference on Fracture Mechanics of Concrete and Concrete Structure (FraMCoS 3), Gifu, Japan*, pages 24–26, 1998.

Kang, J. and J.E.Bolander, . Multiscale modeling of strain-hardening cementitious composites. *Mechanics Research Communications*, 78:47–54, 2016.

Kang, S. B.; Tan, K. H.; Zhou, X. H., and Yang, B. Influence of reinforcement ratio on tension stiffening of reinforced engineered cementitious composites. *Engineering structures*, 141:251–262, 2017.

Kunieda, M.; Kozawa, K.; Ogura, H.; N.Ueda, , and Nakamura, H. Tensile fracture analysis of strain hardening cementitious composites by means of 3d meso-scale

analysis subjected to discretized short fibers. *Doboku Gakkai Ronbunshuu E*, 66 (2):193–206, 2010a.

Kunieda, M.; Kozawa, K.; Ueda, N., and Nakamura, H. Fracture analysis of strain hardening cementitious composites by means of discrete modeling of short fibers. *Fracture Mechanics of Concrete and Concrete Structures*, 2010b.

Li, J.; Qiu, J.; Weng, J., and Yang, E. Micromechanics of engineered cementitious composites (ECC): A critical review and new insights. *Construction and Building Materials*, 2023.

Li, L.; Cai, Z.; Yu, K.; Zhang, Y. X., and Ding, Y. Performance-based design of all-grade strain hardening cementitious composites with compressive strengths from 40 mpa to 120 mpa. *Cement and Concrete Composites*, 97:202–217, 2019.

Li, M. and Li, V. C. Rheology, fiber dispersion, and robust properties of engineered cementitious composites. *Materials & Structures*, 46(3):405–420, 2013a.

Li, Mo and Li, Victor C. Rheology, fiber dispersion, and robust properties of engineered cementitious composites. *Materials and structures*, 46:405–420, 2013b.

Li, V.; Mishra, D. K.; Naaman, A. E.; Wight, J. K.; LaFave, J. M.; Wu, H.-C., and Inada, Y. On the shear behavior of engineered cementitious composites. *Advanced Cement Based Materials*, 1994.

LI, V. C. Postcrack scaling relations for fiber reinforced cementitious composites. *Journal of materials in civil engineering*, 4(1):41–57, 1992.

Li, V. C. and Wang, S. Microstructure variability and macroscopic composite properties of high performance fiber reinforced cementitious composites. *Probabilistic Engineering Mechanics*, 21(3):201–206, 2006.

Li, V. C.; Mishra, D. K.; Naaman, A. E.; Wight, J. K., and Inada, Y. On the shear behavior of engineered cementitious composites. *Advanced Cement Based Materials*, 1(3):142–149, 2003.

Lin, Z. and Li, V. C. Crack bridging in fiber reinforced cementitious composites with slip-hardening interfaces. *Journal of the Mechanics and Physics of Solids*, 45(5):763–787, 1997.

Lin, Z.; Takayuki, K., and Li, V. C. On interface property characterization and performance of fiber-reinforced cementitious composites. *Concrete Science and Engineering*, 1:173–174, 1999.

Liu, K.; Liu, C.-X.; Liu, Y.; Wang, R.-Y., and Kang, S.-B. Experimental and analytical investigations on tension stiffening of reinforced engineered cementitious composites members. *Structures*, 48:976–988, 2023.

Liu, Y.; Zhou, X.; Lv, C.; Yang, Y., and Liu, T. Use of silica fume and ggbs to improve frost resistance of ecc with high-volume fly ash. *Advances in Civil Engineering*, 2018:1–11, 2018.

Maage, M. Fibre bond and friction in cement and concrete. In *Proc., RILEM Symp. Testing Test Methods Fiber Cement Composites*, pages 329–336, 1978.

Madhavi, K. B.; Venugopal, M.; Rajesh, V., and Suresh, K. Experimental study on bendable concrete. *International Journal of Engineering & Technical Research*, V5(10), 2016.

Marshall, D.B. and Cox, B.N. Tensile fracture of brittle matrix composites: Influence of fiber strength. *Acta Metallurgica*, 35(11):2607–2619, 1987.

Moreno, D. M.; Trono, W.; Jen, G.; Ostertag, C., and Billington, S. L. Tension

stiffening in reinforced high performance fiber reinforced cement-based composites. *Cement and Concrete Composites*, 50:36–46, 2014.

Moreno-Luna, D. M. *Tension stiffening in reinforced high performance fiber reinforced cement based composites*. PhD thesis, Stanford University, 2014.

Mustafa, S.; Mohamed, L.; MA, H. K.; Ravi, R., and Li, VC. Influence of aggregate type and size on ductility and mechanical properties of engineered cementitious composites. *ACI Materials Journal*, 106(3):308, 2009.

Naaman, A. E. High performance fiber reinforced cement composites 2 (HPFRCC2). *RILEM Proceedings 31, 1995, London*, 27(5):801–802, 1995.

Naaman, A. E.; Namur, G.; Najm, H., and Alwan, J. Bond mechanisms in fiber reinforced cement-based composites. *Report UMCE 89*, 9, 1989.

Naaman, A. E.; Namur, G. G.; Alwan, J. M., and Najm, H. S. Fiber pullout and bond slip. i: Analytical study. *Journal of Structural Engineering*, 117(9), 1991.

Naaman, A.E. and Shah, S.P. Pullout mechanism in steel fiber reinforced concrete. *Journal of the Structural Division*, 102(8):1537–1548, 1976.

Ogura, H.; Kunieda, M.; Ueda, N., and Nakamura, H. MESO-scale modeling for fiber reinforced concrete under mixed mode fracture. *International Conference on Fracture Mechanics of Concrete and Concrete Structures*, 2013.

Pan, Z. F.; Qiao, Z.; Si, D. D. S., and Shang, J. Q. Experimental investigation and numerical simulation on uniaxial tensile behavior of hybrid PVA–ECC. *Construction and Building Materials*, 398:132517, 2023.

Patzák, B. OOFEM – An object-oriented simulation tool for advanced modeling of materials and structure. *Acta Polytechnica*, 52:59–66, 2012.

Paul, S.C. and Zijl, G. P. A. G. V. Mechanically induced cracking behaviour in fine and coarse sand strain hardening cement based composites (SHCC) at different load levels. *Journal of Advanced Concrete Technology*, 11(11):301–311, 2013.

Redon, C.; Li, V. C.; Wu, C.; Hoshiro, H.; Saito, T., and Ogawa, A. Measuring and modifying interface properties of PVA fibers in ecc matrix. *Journal of materials in civil engineering*, 13(6):399–406, 2001.

Rypl, D. *Sequential and Parallel Generation of Unstructured 3D Meshes*. PhD thesis, Czech Technical University, Prague, Czech Republic, 1998.

Tetsushi, K. and Li, V. C. Practical design criteria for saturated pseudo strain hardening behavior in ECC. *ACT*, 4(1):59–72, 2006.

Wang, S. Micromechanics based matrix design for engineered cementitious composites. *Dissertation Abstracts International, Volume: 66-09, Section: B, page: 4974.;Chair: Victor C. Li.*, 2005.

Wang, S. and Li, V.C. Polyvinyl alcohol fiber reinforced engineered cementitious composites: Material design and performances. *Int'l Workshop on HPFRCC Structural Applications*, pages 65–73, 2011.

Wang, Y.; Liu, F.; Yu, J.; Dong, F., and Ye, J. Effect of polyethylene fiber content on physical and mechanical properties of engineered cementitious composites. *Construction and Building Materials*, 251:118917, 2020.

Yan, Y.; Lu, Y.; Zong, S., and Li, S. Numerical simulation and load-bearing capacity of concrete-filled steel tubes strengthened with CFRP grid-reinforced ECC under axial compression. *Structures*, 57:105320, 2023.

Yang, E.H.; Wang, S.; Y.Yang, , and Li, V. C. Fiber-bridging constitutive law of engineered cementitious composites. *ACT*, 6(1):181–193, 2008.

Yu, K.; Li, L.; Yu, J.; Wang, Y.; Ye, J., and Xu, Q.F. Direct tensile properties of engineered cementitious composites: A review. *Construction and Building Materials*, 165(MAR.20):346–362, 2018.

Zhan, X.F.; Chen, J.Y.; Wang, X., and Yan, H.L. Experimental and numerical study of road-bridge link slabs in fully jointless bridges using rubberized engineered cementitious composites (R-ECC). *Case Studies in Construction Materials*, 20:e02768, 2024.

Zhang, Y.; Ueda, N.; Nakamura, H., and Kunieda, M. Numerical approach for evaluating shear failure behavior of strain hardening cementitious composite member. *Engineering Fracture Mechanics*, 156:41–51, 2016.

Zheng, X. and Zhang, J. Finite element simulation for bending behavior of steel-ECC composite slab considering shrinkage, creep and cracking. *Construction and Building Materials*, 282:122643, 2021.

Zhou, C.; Marlot, A., and Grassl, P. Cdpm2f: A damage-plasticity approach for modelling the failure of strain hardening cementitious composites. *Engineering Fracture Mechanics*, 2024.

Zhou, J.; Qian, S.; Ye, G.; Copuroglu, O.; Breugel, K. V., and Li, V. C. Improved fiber distribution and mechanical properties of engineered cementitious composites by adjusting the mixing sequence. *Cement & Concrete Composites*, 34(3): 342–348, 2012a.

Zhou, J.; Qian, S.; Ye, G.; Copuroglu, O.; Van Breugel, K., and Li, V. C. Improved fiber distribution and mechanical properties of engineered cementitious composites by adjusting the mixing sequence. *Cement and Concrete Composites*, 34(3): 342–348, 2012b.

Zhou, J.; Pan, J., and Leung, C. K. Y. Mechanical behavior of fiber-reinforced engineered cementitious composites in uniaxial compression. *Journal of Materials in Civil Engineering*, 27(1):04014111, 2014.